Cavity Ring-Down Spectroscopy
And Its Application
To
Biomedical Diagnostics

Thesis submitted for the degree of

Doctor of Philosophy (Science)

in

Physics (Experimental)

by

Gourab Dutta Banik

Department of Physics

University of Calcutta

2017

Dedicated to my

Maternal Grandfather and Grandmother…

Abstract

In this thesis, we primarily focused on the development of a high-resolution cavity ring-down spectrometer (CRDS) coupled with a continuous-wave (*cw*) mode-hop-free (MHF) external-cavity quantum cascade laser (EC-QCL) operating at ~5.2 μm in the mid-IR molecular fingerprint region and subsequently we demonstrated its applications in trace gas sensing as well as in high-resolution molecular spectroscopy studies.

We have utilized the EC-QCL based *cw*-CRDS system for ultra-sensitive and trace detection of nitric oxide (N_2O) which is responsible for global warming as well as climate change. We probed the rotationally resolved R(8e) absorption line of (ν_1+ν_2) combination band of N_2O for direct quantitative and selective assessment of the concentration in the samples. The CRDS sensor demonstrates the advantages of monitoring atmospheric N_2O mixing ratios in the ppbv levels with high sensitivity and molecular specificity. A significant change in N_2O levels was observed in different sub-areas depending on the source of local pollution. We also observed a marked difference in N_2O levels between morning and afternoon sessions of the day in a particular sub-area.

In the next study, the *cw*-CRDS was utilized for simultaneous and molecule-specific real-time detection of several environmentally and biomedically important trace molecular species such as nitric oxide (NO), nitrous oxide (N_2O), carbonyl sulphide (OCS) and acetylene (C_2H_2) at ultra-low concentration by probing numerous rotationally resolved ro-vibronic transitions in the mid-IR spectral region within a relatively small spectral range of ~ 0.05 cm^{-1}. Using the current high-resolution spectrometer, the ultra-sensitive detection of NO and OCS in exhaled breath were performed. We also investigated the trace detection of N_2O and C_2H_2 in ambient air.

We have implemented our developed EC-QCL based CRDS system to study high resolution ro-vibrational spectroscopy of linear triatomic molecule like carbonyl sulphide (OCS). We observed the *l* type doubling in Δ vibrational state (*l*=2) in (14^20) ← (02^20) weak hot band transition of OCS and subsequently determined the *l*-type doubling constant, vibrational dipole moments, rotational constants and centrifugal distortion constants for the particular (14^20) vibrational state. The new data are useful for better understanding of linear polyatomic molecular properties.

In the next part of the thesis, we have extended our work in biomedical diagnostics and we demonstrated a new methodology, ^{13}C glucose breath test (^{13}C-GBT) for the accurate non-invasive diagnosis of small intestinal bacterial overgrowth (SIBO) in irritable bowel syndrome (IBS) patients by measuring $^{13}CO_2/^{12}CO_2$ stable isotope ratios in exhaled breath. This new methodology may be used as non-invasive test for screening of SIBO in routine clinical practices.

The present thesis work reveals the development and applications of an EC-QCL based CRDS spectrometer for trace gas sensing and high resolution molecular spectroscopy in mid-IR region of the EM radiation. This high finesse optical cavity based laser spectroscopy technique may open up a new direction of research in non-invasive biomedical diagnostics, environmental science and high resolution fundamental molecular spectroscopy.

List of Publications (included in Thesis Chapters)

1. **Gourab Dutta Banik**, Suman Som, Abhijit Maity and Manik Pradhan, *Cavity ring-down spectroscopy measurements of l-type doubling of hot bands in Δ vibrational states of OCS near 5.2 µm*, **2017** (under review).

2. **Gourab Dutta Banik**, Abhijit Maity, Suman Som, Mithun Pal, Santanu Mandal, Sanchi Maithani and Manik Pradhan, *Multi-component Chemical Sensing using EC-QCL based Cavity Ring-Down Spectroscopy*, **2017** (under revision).

3. **Gourab Dutta Banik**, Suman Som, Abhijit Maity, Mithun Pal, Sanchi Maithani, Santanu Mandal and Manik Pradhan, *An EC-QCL based N_2O sensor at 5.2 µm using cavity ring-down spectroscopy for environmental applications*, **Analytical Methods**, **2017**, 9 (15), 2315-2320.

4. **Gourab Dutta Banik**, Abhijit Maity, Suman Som, Chiranjit Ghosh, Sunil B Daschakraborty, Sujit Chaudhuri, Shibendu Ghosh, Manik Pradhan, *Diagnosis of small intestinal bacterial overgrowth in irritable bowel syndrome patients using high-precision stable $^{13}CO_2/^{12}CO_2$ isotope ratios in exhaled breath*, **Journal of Analytical Atomic Spectrometry**, **2014**, 29 (10), 2014 1918-1924.

List of Publications (Not included in Thesis Chapters)

1. **Gourab Dutta Banik**, Anulekha De, Suman Som, Subhra Jana, Sunil B Daschakraborty, Sujit Chaudhuri, Manik Pradhan, *Hydrogen sulphide in exhaled breath: a potential biomarker for small intestinal bacterial overgrowth in IBS*, **Journal of Breath Research**, **2016**, 10 (2), 026010.

2. Anulekha De†, **Gourab Dutta Banik**†, Abhijit Maity, Mithun Pal and Manik Pradhan, *Continuous wave external-cavity quantum cascade laser-based high-resolution cavity ring-down spectrometer for ultrasensitive trace gas detection*, **Optics Letters**, **2016**, 41 (9), 1949-1952 († equally contributed as first author).

3. Chiranjit Ghosh, **Gourab Dutta Banik**, Abhijit Maity, Suman Som, Arpita Chakraborty, Chitra Selvan, Shibendu Ghosh, Subhankar Chowdhury and Manik Pradhan, *Oxygen-18 isotope of breath CO2 linking to erythrocytes carbonic anhydrase activity: a biomarker for pre-diabetes and type 2 diabetes*, **Scientific Reports (Nature Publishing Group)**, **2015**, 8137.

4. Abhijit Maity, **Gourab Dutta Banik**, Chiranjit Ghosh, Suman Som, Sujit Chaudhuri, Sunil B Daschakraborty, Shibendu Ghosh, Barnali Ghosh, Arup K Raychaudhuri and Manik Pradhan, *Residual gas analyzer mass spectrometry for human breath analysis: a new tool for the non-invasive diagnosis of Helicobacter pylori infection*, **Journal of Breath Research**, **2014**, 8 (1), 016005.

Acknowledgement

It is the wonderful moment that the every graduate student aspires for! It is the moment that I have been dreaming for past several years! The journey, I started almost five years back is now come to an end with a new recognition of my research career and here, I am about to write the marvellous experiences of that long journey! The journey not only enriched me academically but non-academically also. Before joining to S.N. Bose centre, I spent almost three years at National Institute of Technology, Durgapur for my post graduate study and I could well remember the fantastic and exciting experiences which I would gather in those upcoming days. And none of these would be possible without those peoples whom I have come across during my PhD and before. I would like to begin by expressing my deepest gratitude to my supervisor Dr. Manik Pradhan for his unwavering support, consistent motivation and right direction throughout my PhD life. I have immensely benefited from his sound advice, good ideas, in depth experimental knowledge and continuous encouragement. His unconditional support from the happiest to the darkest moment of my life is what makes all the differences.

I would like to extend my sincere gratitude to our collaborator Dr. Sujit Chaudhri, AMRI Hospital, Salt Lake, Kolkata and Dr. Sunil B. Daschakraborty, Ruby General Hospital Kolkata for helping me in different ways during the bio-medical studies performed in the hospitals.

I would like to thank all of my lab mates Abhijit Maity, Chiranjit Ghosh, Suman Som, Mithun Pal, Sanchi Maithani, Santanu Mandal, Akash Das, Sasthi Charan Mandal, Iqbal Ahmed for providing the wonderful and friendly environment in the lab. Special thanks go to Abhijit for the useful discussions during the development of the experimental set-up and Suman with whom I have managed to work during the bio-medical studies in last five years. His assistance and hard work during the CRDS experiments helped me lot to perform those studies in short span of time. I again thank Suman for being a wonderful friend and colleague. I am thankful to Pabitra da (Dr. Pabitra Mondal) for many helpful discussions regarding the data acquisition part of the experiment and Mr. Amit Ghosh in the mechanical workshop for his expert assistance with metal cutting and lathing work.

I am grateful to my physics teacher Mr. Tarashankar Bhattacharya of Vidyasagar College, Kolkata for his excellent teaching, affection and always inspiring me to do the research in physics from my college days. Beside that I would like convey my sincere gratitude to Prof. P. Kumbhakar, Prof. A. K. Meikap, Dr. Mrinal Kanti Mandal, Dr. Sukadev Sahoo and Dr. Soumen Basu of NIT, Durgapur for their motivation in doing research during my post graduate studies.

I would like to thank my friends Sanjib, Atanu, Tushar, Sandip, Debu (Debabrata), Dipak, Alam, Moumita, Baishaki, Pampi and Azhar for making my college days wonderful with evergreen memories. My Special thank goes out to all of my friends at

NIT, specifically Raja Da (Dr. Mrimoy Goswami), Ayan Da (Dr. Ayan Mukherjee), Arnab Da (Dr. Arnab Maity), Subho Da (Dr. Subhojyoti Sinha), Himadri, and Avirup. I convey my heartiest gratitude to my fellow SNBNCBS mates for their wonderful company during my stay at SNBNCBS for almost five years, in particular Animesh da, Nirnay, Krishnendu, Shankar, Sushovan, Nabarun, Shamim, Sutapa, Semanti di, Susmita di, Bibhas da, Bipul da, Subhasish da, Sayani di for helping me in every possible way and made my life enjoyable with their presence.

I also wish to express my love and gratitude to my parents, brother, in-laws and all other family members. My deepest and sincere gratitude to my late grand-mother (Thakuma) and maternal grandfather (Dadu) for their affection love in my childhood days and for teaching me about the ethics of life. I want to convey my sincere gratitude to that person who always takes my care and supports me in each ups and downs in my life, is my maternal grandmother (Mum). Thank you Mum for being always with me! I would particularly like to thank my beloved wife Deboshri for her love, trust, sacrifice, inspiration and support throughout everything in all tough time of my PhD life. She is the only person with whom I can share all my personal and professional problems without thinking once. I am thankful to God for choosing her as my life partner. I would also like to thank my Mejomama (Mr. Sibaji Banik) for his support during my tough time and special thank goes to my mother in law (Mrs. Bandana Dutta Banik) for her effortless helps during the final year of my PhD.

Finally, I would like to acknowledge DST-INSPIRE Fellowship award for pursuing doctoral research funding and thankful to S. N. Bose National Centre for Basic Sciences for providing the excellent research facility.

Gourab Dutta Banik

Table of Contents

1 An introduction to infrared spectroscopy and common detection techniques of trace molecular species

Contents

1.1 Introduction

Spectroscopy is the branch of science which deals with interaction of electromagnetic (EM) radiation with matters (e.g. atoms, molecules *etc.*). The atoms or the molecules absorb energy (or to emit energy) from the EM radiation and subsequently transfer it into another excited state. Since the atoms or the molecules can only exist at well-defined discrete energy levels, only the radiation with certain energy can be absorbed which further indicates about the spacings between the quantized energy levels that are associated with various internal motions of the system. In atomic systems, electrons are in motion and the transition demonstrates the change in electronic configuration, whereas in molecular systems, the internal motions including the rotation, vibration and the orientations of the nuclear spins govern the transitions[1,2]. To analyse the observed spectra, the quantum mechanical models of distribution of discrete energy levels in a molecule are employed to get the information about the structure and properties of the molecule including the bond lengths, strengths of its bonds, the identity and relative positions of its constituent atoms, the energies and symmetries of its molecular orbitals[3]. The intensities of the observed spectral transition demonstrate the relative populations of individual molecular energy levels and the “selection rule” governs which levels may be coupled by allowed transitions, suggest the symmetry of the molecular electronic wave functions which enabled us to identify the particular molecular states. The observed energy level pattern provides the information about thermodynamic properties (enthalpy, entropy, heat capacity, etc.) of molecules, and equilibrium constants for chemical reactions whilst the spectrum of a given species indicates an absolutely unique molecular fingerprint, an essential tool for monitoring the trace species in bio-medical diagnostics[4-6] environmental monitoring application[7,8] and have wide range of implications in analytical chemistry[9-11] and astrophysics[12-14].

A numerous gaseous chemical substances exhibit strong fundamental vibrational absorption bands in the mid-infrared (mid-IR) spectral region and the absorption of EM radiation by these fundamental bands provide unique features for their detection. Thus the region is the most convenient for monitoring the trace molecular species in exhaled breath and atmospheric sample via direct quantitative absorption. In the mid-IR region these fundamental bands may have the absorption cross-section one or more orders of magnitude higher than the overtone or combination bands that occur in the near-IR region (NIR). In the past few decades, the low cost, cryogenic cooling free tunable diode lasers operating in the NIR spectral region were widely used for monitoring the trace species in gaseous sample. In the NIR region, the molecules generally have the smaller absorption cross-sections than in the ultraviolet (UV) or mid-IR regions but the detection methods have some advantages over other spectral regions. In presence of broad absorption band in the UV region, it is difficult to detect the specific molecules via strong electronic transitions. Moreover, the high cost of the mid-IR transmitting materials and the unavailability of high sensitive detectors restricted the use of mid-IR sources for monitoring the trace species in gaseous sample. But, with the technological advancement in the fabrication of semiconductor materials, the solid state mid-IR laser sources become very popular for their applications to direct quantitative measurements of trace species using the absorption spectroscopic techniques. An ideal mid-IR source would have some following properties[15]: (1) high optical power to overcome inherent electronic detection noise and ensure high laser signal-to-noise ratios, (2) narrow linewidth to obtain high selectivity and sensitivity, (3) single longitudinal mode operation with low amplified spontaneous emission output for high selectivity and elimination of intermode competition noise, (4) ease of tailoring the inherent laser operating wavelength (design of gain material and/or cavity structure) to access the desired absorption region, (5) low source noise and low amplitude modulation; (6) high beam quality, i.e., small beam divergence, small astigmatism, and stable, predictable beam output direction, for optimum coupling into and through a gas sampling cell, (7) low temperature and current tuning rates to minimize wavelength jitter induced by controller noise, (8) rapid wavelength tunability for fast response and high data acquisition rates, (9) minimal susceptibility to changing environmental conditions of temperature, pressure, humidity (10) no long term changes in laser wavelength and/or spatial output characteristics, and (11) compact and robust overall sensor package size. However, it is really challenging to achieve all these idealized properties in any real world mid-IR laser source but some of them attributes are more important for a given application to obtain the best possible measurement performance. However, the quantum cascade lasers currently play the pivotal role in mid-IR photonics and a relatively recent development in the field of semiconductor laser technology. In early days, the mid-IR semiconductor laser operation was based on inter-band transitions whereas in quantum cascade lasers utilize the property of intersubband transitions within a multiple quantum-well structure. This offers excellent designs flexibility because the staircase of intersubband transitions can be designed to obtain particular emission wavelengths. More recently, room-temperature controlled, widely tunable with mode-hop-free tuning features, continuous wave, single mode, high output power with extremely narrow line width mid-IR QCL sources have been developed and thus encourages the research on the development of novel optical sensors for monitoring the single or multiple trace chemical species in a gas sample with high sensitivity and molecular selectivity[16].

1.2 Infrared absorption spectroscopy

In the IR-spectral region of the EM radiation the molecules undergo vibrational transitions, resulting the vibrational absorption spectra consist of a large number of discrete closely spaced components (typically ≤ 10 cm^{-1}) which arise from rotational transitions that are associated with each vibrational excitation. Each line has a certain linewidth and shape that depends on temperature and surrounding environment of the molecules. The spectroscopic transitions between vibrational, rotational and rotational-vibrational ("ro-vibrational") states occur in the infrared "fingerprint" region are discussed briefly in this section.

1.2.1 Vibrational spectroscopy

Vibrational spectroscopy deals with transitions between the quantized vibrational energy levels associated with bond stretching or bending when exposed to EM radiation. When the constituent atoms of a molecule are displaced relative to one another, the dipole moment changes and the vibration is said to be infra-red active. It is noteworthy to mention here that not the permanent dipole moments rather the "changes in the dipole moment" plays the central role to excite the molecule in higher vibrational energy state when exposed to EM radiation. Thus every chemically heteronuclear diatomic molecule (such as HCl, NaBr or OH etc.) can be considered as vibrationally or "infrared" *active*, since the differences in atomic polarizabilities ensure that there is always some non-zero permanent dipole moment whose magnitude will oscillate when the bond stretches. By the same argument, the homonuclear diatomic molecules such as H_2, N_2 etc. can be considered as vibrationally or "infrared" *inactive*.

The situations become more complicated when the vibration of a polyatomic molecules are considered. A molecule containing N atoms will have 3N degrees of freedom as the positions of each atom are specified by the three co-ordinates (e.g. x, y and z coordinates) in Cartesian system and their motions are independent of the others. However, the fixed bond distances and the bond angles constrained their motion. If a molecule is free to move in 3D space, the translational movement is noted by its centre of gravity which requires three coordinate values. Also, the rotation of a non-linear molecule can be resolved into three perpendicular axes which require three more degrees of freedom. Thus the non-linear molecules have 3N-6 fundamental vibrations. Again, the linear molecules do not exhibit the rotation about the bond axis, so only two rotational degrees of freedom are allowed. Thus the linear molecules show 3N-5 vibrational fundamentals vibrations. Among these fundamental vibrations, there are N-1 vibrational motions related to bond stretching whereas 2N-5 and 2N-4 fundamental vibrations related to bending motions in non-linear and linear molecules, respectively. For an illustrative example, the vibration of a simple linear tri-atomic molecule CO_2 (O=C=O) is depicted in figure-1.1.

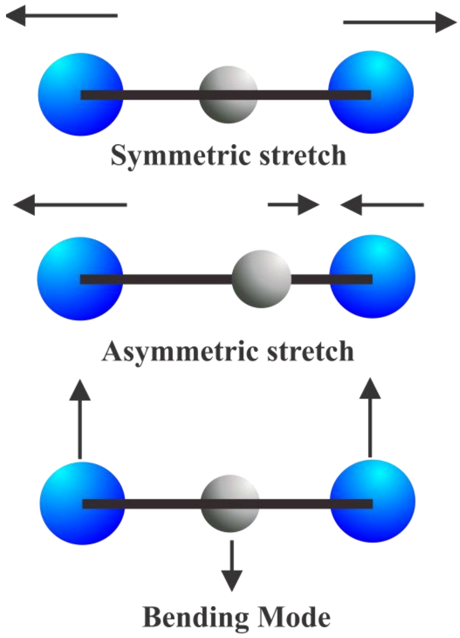

Figure 1.1 *Vibrational modes of CO_2 molecule.*

It is a symmetric linear species and has no permanent dipole moment, and hence it is microwave inactive. It has 3N-5=4 fundamental modes, among these N-1=2 stretching modes and 2N-4=2 bending modes of vibration. The "symmetric stretch" mode (ν_1) in which both C=O bonds stretch and compress in phase with each other, the "anti-symmetric stretch" mode (ν_3) in which one bond compresses while the other stretches, and vice versa, and the bending mode (ν_2). It is clear from the figure-1.1 that the symmetry of the molecule is maintained throughout the course of the symmetric stretching vibration, so the vibrational motion does not give rise to any temporary or "instantaneous" dipole moments. In contrast, for both the anti-symmetric stretch and bending modes, the molecular distortion that occurs during the vibrational cycle will give rise to a temporary dipole moment which oscillates in magnitude and direction as the motion proceeds. The bending mode of the CO_2 molecule is doubly degenerate whereas the anti-symmetric stretching mode is non-degenerate. The frequencies of the fundamental vibrational modes of CO_2 are shown in the Table-1.1.

Table 1.1 Summary of the Fundamental vibrational modes of CO_2

Assignment	Description	Band origin/cm^{-1}	IR active
ν_1	Symmetric stretching	1388	No
ν_2	Bending	667	Yes
ν_3	Asymmetric stretching	2349	Yes

.

The vibrational motion of a diatomic molecular system can be described using a simple harmonic oscillator (SHO) model in quantum mechanics. The Schrödinger equation can be applied to solve the energy eign value of a molecule in a particular vibrational state. If ψ (r) is the analogous wave function corresponds to a particular vibrational state of a molecule with eign energy value E_{vib}, then the vibrational Hamiltonian for that particular state can be given by,

$$\hat{H}_{vib}\,\psi(r) = -\frac{\hbar^2}{2\mu}\frac{d^2\psi(r)}{dr^2} + V(r)\psi(r) = E_{vib}\,\psi(r) \tag{1.1}$$

Considering the potential energy function V(r) $=\frac{1}{2}k(r-r_e)^2$ [(r-r_e), is the difference between the inter-nuclear and equilibrium separation of the bond] the energy eign value can be evaluated and expressed by:

$$E_v = (v+1/2)h\nu_0 \tag{1.2}$$

where, ν_0 is the frequency of the oscillation (in Hz) of the molecule, given by:

$$\nu_0 = \frac{1}{2\pi}\sqrt{\frac{k}{\mu}} \tag{1.3}$$

where μ is the reduced mass of the molecule and k is the bond force constant and v is the vibrational quantum number has the allowed values of $v = 0, 1, 2, 3, \ldots$

In spectroscopy, the vibrational energies usually expressed in cm^{-1} and it is customary to use 'G' to represent the vibrational energies in those units:

$$G(v) = \frac{E_v}{hc} = \left(v + \frac{1}{2}\right)\tilde{\nu}_0 \ [\mathrm{cm}^{-1}] \tag{1.4}$$

$$\text{In which } \tilde{\nu}_0 = \frac{1}{2\pi c}\sqrt{\frac{k}{\mu}} \ [\mathrm{cm}^{-1}] \tag{1.5}$$

Figure 1.2 shows the quantum mechanical wave function and energy level for a few of the lowest value of a diatomic molecular system considering the potential energy function of a SHO.

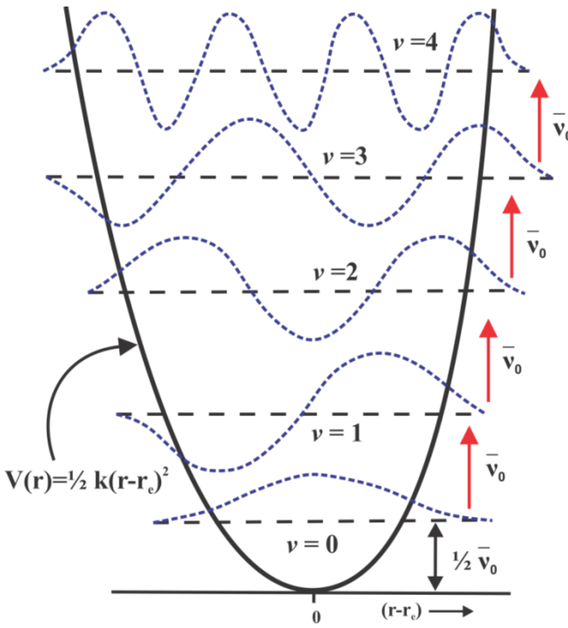

Figure 1.2 *Harmonic oscillator wave function of a diatomic rigid molecule with few lower energy levels. The separation between the adjacent energy levels is* $\tilde{\nu}_0$ *with zero-point energy* $\frac{1}{2}\tilde{\nu}_0$

The qualitative properties of the wave functions are exactly same as SHO but the lowest harmonic oscillator level allowed by quantum mechanics does not have zero vibrational energy, but rather has a *zero point energy* of

$$G(0) = \frac{1}{2}\tilde{\nu}_0 \tag{1.6}$$

The vibrational transitions are governed by the following "selection rules":

Vibrational Selection Rule 1: Vibrational transitions can only occur if the dipole moment of the molecule oscillates in the course of the vibrational motion.

Vibrational Selection Rule 2: If the molecular dipole moment varies linearly with bond stretching, a harmonic oscillator can only undergoes $\Delta v = \pm 1$ transitions.

Applying the selection rules, immediately we have the transition energies between adjacent vibrational levels of a harmonic oscillator i.e

.
$$\Delta G = G(v+1) - G(v)$$

$$= (v+1+1/2)\tilde{\nu}_0 - (v+1/2)\tilde{\nu}_0$$

$$= \tilde{\nu}_0 \text{ cm}^{-1} \tag{1.7}$$

Since all the vibrational spacing are the same, all the allowed transition would be piled up one another at exactly the same frequency $\tilde{\nu}_{vib} = \tilde{\nu}_0$. However, in reality some additional factors make the vibrational spectra more interesting. These are as follows:

(i) The angular momentum does not relate with radial vibrational motion of a molecule. Since the angular momentum must be conserved during the absorption or emission process of a photon, all vibrational spectra must really be ro-vibration spectra, with a simultaneous change in rotational quantum number J taking into account the angular momentum of photon.

(ii) For very small amplitude of oscillation from equilibrium, the dipole moment varies linearly. However, to describe it more accurately quadratic, cubic and higher order terms are required to incorporate in dipole moment function. For a harmonic oscillator those terms are allowed with the condition $|\Delta v| > 1$ and the transitions energies are given by $\tilde{\nu}_{vib} = 2\tilde{\nu}_0, 3\tilde{\nu}_0 ...$ etc. Thus the multiples of the frequency $\tilde{\nu}_0$ are observed in the vibrational spectra. The intensities of the overtone transitions rapidly become much weaker as $|\Delta v|$ increases.

(iii) The simple harmonic-oscillator potential is not a very good approximation to describe the real potential energy curve of a linear diatomic molecule. Almost all intermolecular potentials are approximately quadratic near their minima but the harmonic oscillator function goes to infinity at large $|r-r_e|$, which indicates the bonds never break. This is not practical. At $r \rightarrow 0$ i.e. as the nuclei are pushed together the real potential function must approach infinity, while as $r \rightarrow \infty$ it must approach an asymptote at the bond dissociation energy (see figure 1.3). Because of this shape asymmetry, the vibrational level spacings of a realistic potential are not constant (as they are for a harmonic oscillator), but become smaller with increasing energy, and the simple $\Delta v = \pm 1$ orthogonality selection rule is no longer strictly true.

A realistic and widely used potential function that describes the vibration of the di-atomic molecules is the Morse function and given by:

$$V(r) = D_e\left[1 - e^{-\beta(r-r_e)}\right]^2$$
$$= D_e\left[e^{-2\beta(r-r_e)} - 2e^{-\beta(r-r_e)} + 1\right] \qquad (1.8)$$

In which D_e is the depth of the potential energy well, known as bond dissociation energy, r_e is the equilibrium bond length and β defines stiffness of small amplitude vibrations near the potential minimum. The characteristic shape of the Morse potential with some properties is shown in the figure 1.3.

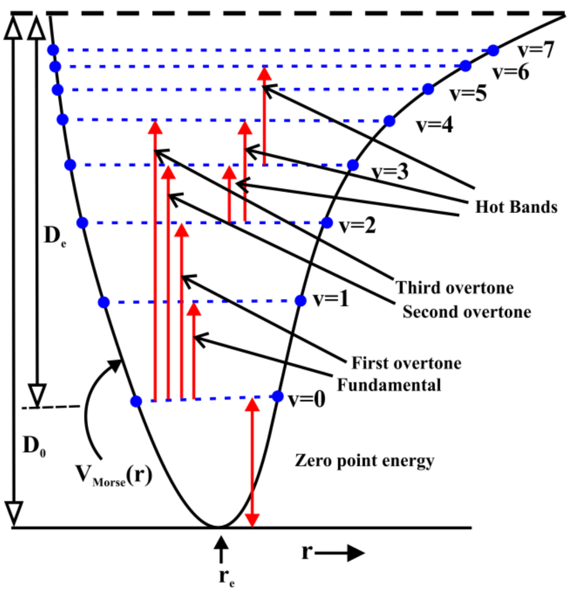

Figure 1.3 *Vibrational levels and transitions in a Morse potential energy function*

The positive first squared exponential term in equation (1.8) dominates short-range repulsive behaviour, the middle negative term is responsible for the attractive potential well and long-range behaviour whereas, the last constant term indicates the potential asymptote. Using the Morse potential function the Schrödinger equation can be solved analytically and the vibrational energy level can be expressed as:

$$G(v) = \left(v + \frac{1}{2}\right)\tilde{\nu}_0 - \left(v + \frac{1}{2}\right)^2 \tilde{\nu}_0 x_e \tag{1.9}$$

$$\text{where,}\quad \tilde{\nu}_0 = \frac{\beta}{2\pi c}\sqrt{\frac{2D_e}{\mu}}\ \ [\mathrm{cm^{-1}}] \tag{1.10}$$

$$\text{and}\ \tilde{\nu}_0 x_e = \frac{h\beta^2}{8\pi^2 \mu c}\,[\mathrm{cm^{-1}}] \tag{1.11}$$

From the equation (1.9) we can estimate the ground state energy of the molecule and given by:

$$G(0) = \frac{1}{2}\tilde{\nu}_0\left(1 - \frac{1}{2}x_e\right) \tag{1.12}$$

Using the equations (1.10) and (1.11) the value of bond dissociation energy can be obtained and given by:

$$D_e = \frac{(\tilde{\nu}_0)^2}{4\tilde{\nu}_0 x_e}\ \ [\mathrm{cm^{-1}}] \tag{1.13}$$

Thus the second term in equation (1.12) represents the correction to the vibration energy level of a molecule and effectively responsible for bond breaking. If we expand the Morse function about $r = r_e$, then,

$$V(r) \approx D_e\left\{[\beta(r - r_e)]^2 - [\beta(r - r_e)]^3 + \frac{7}{12}[\beta(r - r_e)]^4 - \frac{1}{4}[\beta(r - r_e)]^5 + \ldots\right\} \tag{1.14}$$

If $|r-r_e|$ is very small, the cubic and the higher order terms become much smaller and the potential reduces to simple harmonic oscillator potential with $k = 2D_e\beta^2$. Thus at small |r-re|, the higher order "anharmonic" terms are added to the potential function to make the shape more realistic. Because of the anharmonicity in the potential energy function, the orthogonality in the selection rule Δv = ±1 is restricted and vibration selection rule is modified as:

Transitions in which the vibrational quantum number changes by one, Δv = ±1, are strongly allowed whereas the transitions with Δv = ±2, ±3,… become much weaker with increasing |Δv|.

Therefore, the observed strongest transition is associated with |Δv| = 1 and the corresponding energies of the transition are

$$\Delta G = G(v+1) - G(v)$$
$$= \left\{ \left(v+1+1/2\right)\tilde{\nu}_0 - \left(v+1+1/2\right)^2 \tilde{\nu}_0 x_e \right\} - \left\{ \left(v+1/2\right)\tilde{\nu}_0 - \left(v+1/2\right)^2 \tilde{\nu}_0 x_e \right\}$$
$$= \tilde{\nu}_0 - 2\tilde{\nu}_0 x_e (v+1)$$

(1.15)

The equation indicates that with increasing the vibrational quantum number *v*, the vibrational energy level spacing become smaller and diminishes completely at the dissociation limit as shown in figure 1.3. The energy associated with the transition *v* = 0 → *v* = 1 is known as the *fundamental vibration* and given by

$$\Delta G = G_{v=1} - G_{v=0}$$
$$= \tilde{\nu}_0 (1 - 2x_e)\ \mathrm{cm}^{-1} \tag{1.16}$$

Since at normal temperatures, ground vibrational state has the substantial population, hence the transitions with |Δv|=1 are the most intense and have the dominant features in the vibrational spectrum. However the energy associated with *v* = 0 → *v* = 2, *v* = 0 → *v* = 3 *etc*. are known as "*first overtone*", "*second overtone*" etc. and given by

$$\Delta G = G_{v=2} - G_{v=0}$$
$$= 2\tilde{\nu}_0 (1 - 3x_e)\ \mathrm{cm}^{-1} \tag{1.17}$$

$$\Delta G = G_{v=3} - G_{v=0}$$
$$= 3\tilde{\nu}_0 (1 - 4x_e)\ \mathrm{cm}^{-1} \tag{1.18}$$

Thus the intensities of the transition associated with |Δv|= ±2, ±3 are much weaker than the fundamental. Moreover, the energy associated with transitions among higher vibrational levels is known as "hot bands" because the lower levels of such transitions would only have significant population at higher temperature. These transitions are normally very weak and found to at slightly lower wavenumber than the fundamentals.

1.2.2 Rotational spectroscopy

Each vibrational energy level consists of a large number of more closely spaced rotational lines, arise due to interaction of dipole moment of the rotating molecule with the oscillating electric field of incident IR light. If we consider a polar diatomic molecule freely rotating in free space with a fixed angular velocity, the component of its dipole along a chosen axis in the plane of rotation will oscillate sinusoidally, as shown in figure 1.4. When the frequency of the electric field of the incident IR light matches with natural frequency of rotation of the molecule, it will receive the periodic force in phase with its motion and absorb energy from the field and rotate faster.

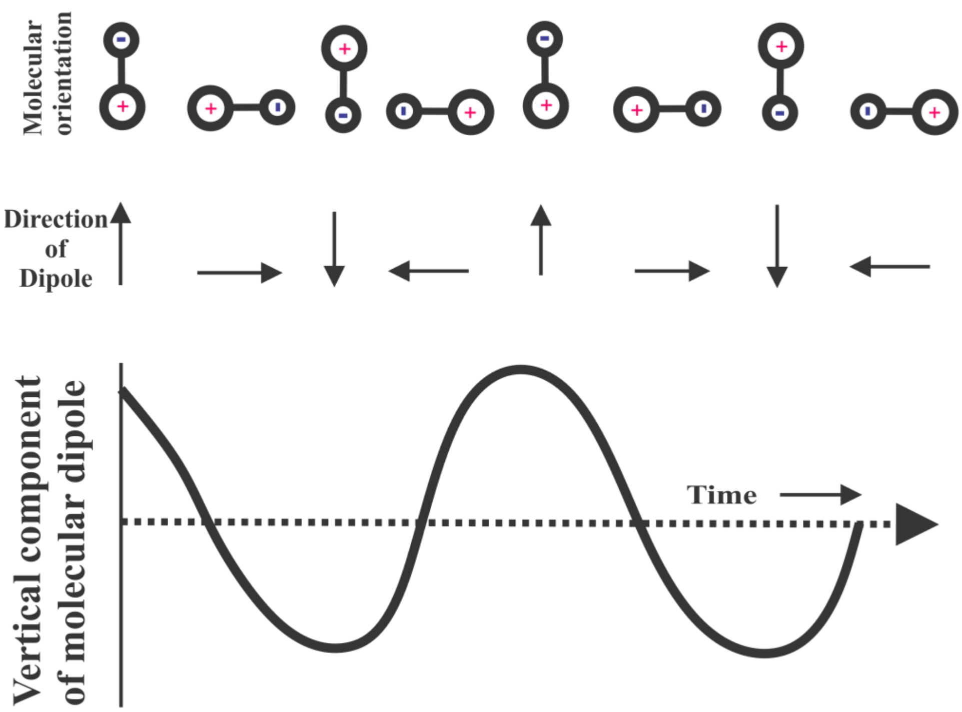

Figure 1.4 *Behaviour of the vertical component of the dipole field of a polar molecule rotating clockwise in the plane of paper*

However, the Schrödinger equation can be applied to measure the allowed energy levels of the rotating molecules. If ψ (Φ) is the analogous wave function corresponds to a particular rotational state of a molecule with energy eign value E_{rot}, then the rotational Hamiltonian for that particular state can written as

$$\hat{H}_{rot}\,\psi(\phi) = -\frac{\hbar^2}{2\mu r^2}\frac{d^2\psi(\phi)}{d\phi^2} = E_{rot}\,\psi(\phi) \tag{1.19}$$

On solving the equation (1.19), the energy eign value for the particular state can be evaluated and expressed by:

$$E_{rot} = \frac{(l\hbar)^2}{2\mu(r_e)^2} = \frac{(l\hbar)^2}{2I} \tag{1.20}$$

in which l = 0, 1, 2...etc and I is the moment of inertia of the system.

Again for a rigid molecular system rotating freely in a space, the rotational energy can be noted as

$$E = \frac{L^2}{2I} \tag{1.21}$$

where, L is the magnitude of the angular momentum ($\vec{L}$). Comparing the equation (1.20) and (1.21) it can be stated that the allowed values for the angular momentum are $L = (l\hbar)$ for any positive integer value of l. Moreover, the allowed values of the angular momentum in 3D space is given by

$$|\vec{L}| = L = \hbar\sqrt{J(J+1)} \text{ for } J = 0, 1, 2, 3, \ldots \text{etc.} \tag{1.22}$$

where, J represents the total angular momentum of the molecule and hence the rotational energy level of a rigid molecule can be written as:

$$E_{rot} = \frac{h^2}{8\pi^2 I} J(J+1) \text{ [Joule]} \tag{1.23}$$

As discussed in previous section 1.2.1, the rotational energy can also be expressed in cm^{-1} and noted by

$$F(J) = \frac{E_{rot}}{hc} = \frac{h}{8\pi^2 Ic} J(J+1) = BJ(J+1) \text{ [cm}^{-1}\text{]} \tag{1.22}$$

in which, $B = \dfrac{h}{8\pi^2 Ic}$ [in cm^{-1}] is called the rotational constant of the molecule.

From the equation (1.22), one can predict the allowed rotational energy levels of a molecule have the energies 0, 2B, 6B, 12B… etc. as shown in figure 1.5. The systematic increase in spacing between the two consecutive J values leads to identify the upper and lower level quantum numbers associated with observed transitions. The important property of a photon is that it has an intrinsic angular momentum 1 and it must be conserved whenever a molecule absorbs or emits a photon, the rotational quantum number must be changed by ΔJ = ±1. Thus the only rotational transitions between adjacent J levels are allowed and the observed transition energies are

$$\begin{aligned}\tilde{\nu}_J^{rot} = \Delta F(J) &= F(J+1) - F(J) \\ &= B[(J+1)(J+2) - (J+1)] \\ &= 2B(J+1)\end{aligned} \tag{1.23}$$

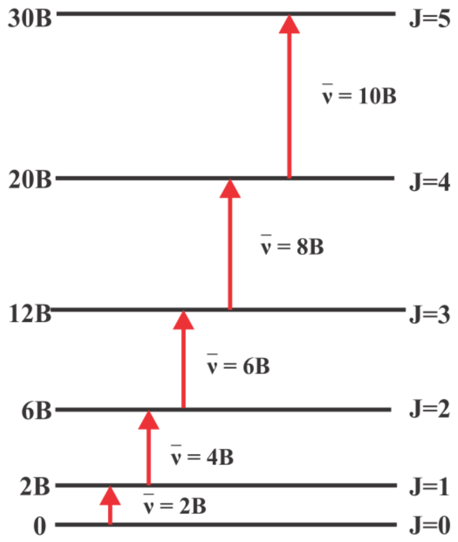

Figure 1.5 *Rotational energies and level spacings for a linear rigid molecule*

Therefore, the pure rotational spectrum is consist of a set of spectroscopic lines whose energies increases linearly with J and those lines will be equally spaced with a separation of 2B as shown in equation (1.24)

$$\begin{aligned}\Delta\tilde{\nu}_J^{rot} = \tilde{\nu}_J^{rot} - \tilde{\nu}_{J-1}^{rot} &= \Delta F(J) - \Delta F(J-1) \\ &= 2B[(J+1) - J)] \\ &= 2B\end{aligned} \tag{1.24}$$

Thus the rotational spectroscopic lines can be observed when the energy of the absorbed or emitted light exactly equals the spacing between the initial and final levels, and if the following two selection rules are obeyed.

Rotational Selection Rule 1: $\Delta J = \pm 1$; since the photon has an angular momentum of $1\hbar$ that must be added to or subtracted from the angular momentum of the molecule when a spectroscopic transition occurs.

Rotational Selection Rule 2: The molecule must possess a permanent electric dipole moment which applies a torque to the oscillating electric field of the light in order to rotational transition to occur.

In reality, the molecular bonds are not rigid. As the molecule rotates, the nuclei are pulled apart by centrifugal forces, and those forces are increased with increment in rate of rotation. Thus, rotational quantum number J increases and the effective bond length enhanced also. This in turn leads to an increase in the moment of inertia and at higher J values the rotational spacing become progressively smaller. The rotational stretching or the centrifugal distortion, is normally accounted to express the rotational energy and denoted by the following:

$$F_v(J) = B_v\left[J(J+1)\right] - D_v\left[J(J+1)\right]^2 \tag{1.25}$$

where, B_v is the vibrational dependence of the rotational constant term and D_v is the centrifugal distortion constant whose magnitude depends inversely on strength of the bond. In general, $D_v << B_v$ which implies the weak bonds distort more than strong bonds. The rotational transition energy is given by:

$$\begin{aligned}\tilde{\nu}_J^{rot} = \Delta F_v(J) &= F(J+1) - F(J) \\ &= \left\{B_v\left[J(J+1)(J+2)\right] - D_v\left[(J+1)(J+2)\right]^2\right\} \\ &\quad - \left\{B_v\left[J(J+1)\right] - D_v\left[J(J+1)\right]^2\right\} \\ &= 2B_v(J+1) - 4D_v(J+1)^3\end{aligned} \tag{1.26}$$

and the rotational energy level spacing is given by

$$\Delta \tilde{\nu}_J^{rot} = \tilde{\nu}_J^{rot} - \tilde{\nu}_{J-1}^{rot} = \Delta F_v(J) - \Delta F_v(J-1)$$
$$= 2B_v - 4D_v(J^2 + 3J + 1) \tag{1.27}$$

However, to describe the rotational energy levels of the non-rigid rotator more accurately, some additional higher order terms are added to it and can be expressed in more general fashion as shown below.

$$F_v(J) = B_v J(J+1) - D_v[J(J+1)]^2 + H_v[J(J+1)]^3 - L_v[J(J+1)]^4 + ... \tag{1.28}$$

in which H_v and L_v are the higher-order centrifugal distortion constants. In fact, the rotational energy actually depends on the set of rotational constants (B_v, D_v, H_v, L_v,… etc.) that led us to label B_v as the inertial rotational constant.

1.2.3 Ro-vibrational spectroscopy

A real molecule can rotate and vibrate simultaneously. Since the vibrational frequency is higher than the rotational frequency by one to two orders of magnitude, the molecule undergoes many vibrations (~100) during one period of rotation. In the previous section 1.2.2, we have considered the transitions between rotational energy levels associated with same vibrational level (usually v = 0). In this section, we have considered the transitions between the sets of rotational energy levels associated with two different vibrational levels. Thus, a vibrational "band", that is a transition $v' \leftrightarrow v''$, is composed of number of "lines" $v'J' \leftrightarrow v''J''$. Therefore, ro-vibrational spectroscopy describes the fine structure of vibrational spectra which arise from rotational transitions accompanying a vibrational excitation. Applying the Born-Oppenheimer approximation, we can consider that the rotational-vibrational energy levels (E^{vr}) can be expressed by sum of the rotational energy level $F_v(J)$ and the vibrational energy level $G(v)$

$$E^{vr} = G(v) + F_v(J)$$
$$= \tilde{\nu}_0(v+1/2) - \tilde{\nu}_0 x_e(v+1/2)^2 + ... + B_v J(J+1) - D_v J^2(J+1)^2 + ... \tag{1.29}$$

Figure 1.6 indicates the rotational levels associated with two vibrational levels v' and v''. And the selection rules are as follows.

Ro-vibrational Selection Rule -1:

The selection rules are the same as for each rotational and vibrational component separately, i.e. Δv = ±1, and ΔJ= ±1. The selection rule ΔJ = ±1 strictly holds for the molecules in Σ state.

Ro-vibrational Selection Rule -2:

The molecules must have change in dipole moment during simultaneous rotation and vibration, when exposed to electromagnetic radiation.

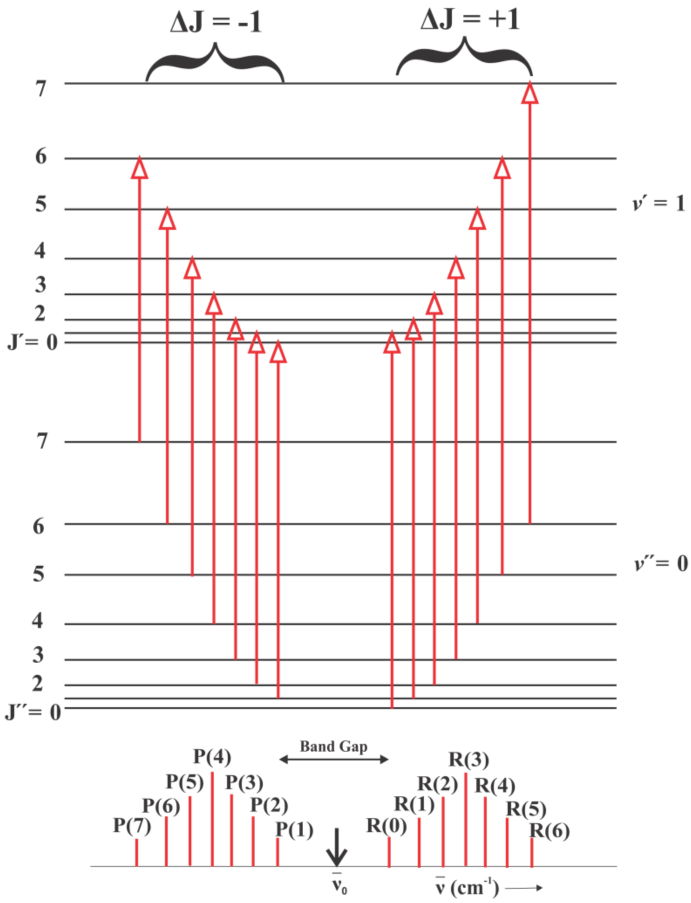

Figure 1.6 *Ro-vibrational spectrum and energy level pattern of a rigid diatomic molecule*

Transitions with ΔJ = 0 can occur when the electronic angular momentum of the molecule is non-zero. The band origin is a place where $J' = J'' = 0$ transition would occur if it were allowed. Thus the vibration band composed of number of branches which in the simplest case are:

$$\begin{aligned} R-branch &: \Delta J = J' - J'' = +1 \\ Q-branch &: \Delta J = 0 \\ P-branch &: \Delta J = J' - J'' = -1 \end{aligned} \tag{1.30}$$

It is noteworthy to mention here that Q branch transitions are forbidden in Σ state. The frequencies of the each lines of the P branch can be written as:

$$\begin{aligned}\tilde{\nu}_P(J) &= \tilde{\nu}_0 + B'J'(J'+1) - B''J''(J''+1)\\ &= \tilde{\nu}_0 + B'(J''-1)J'' - B''J''(J''+1)\\ &= \tilde{\nu}_0 - (B'+B'')J'' + (B'-B'')J''^2\end{aligned} \qquad (1.31)$$

Similarly, the frequencies of the each lines of the R branch can be written as:

$$\tilde{\nu}_R(J) = \tilde{\nu}_0 + (B'+B'')(J''+1) + (B'-B'')(J''+1)^2 \qquad (1.32)$$

If we consider that the ro-vibrational interaction term α is very small, then $B' \approx B''$ which indicates that the ro-vibrational band appears nearly symmetrical (e.g.-HCl) about the band centre $\tilde{\nu}_0$. Thus,

$$\begin{aligned}\tilde{\nu}_P(J) &= \tilde{\nu}_0 - 2BJ''\\ \tilde{\nu}_R(J) &= \tilde{\nu}_0 - 2B(J''+1)\end{aligned} \qquad (1.32\text{ a})$$

There is approximately equal spacing between the adjacent lines of P branch and twice as large a space between the first P and R branch line, i.e. $\tilde{\nu}$ [R(0)-P(1)]=4B. This spacing between R(0) and P(1) is known as zero gap. This is the region where $\tilde{\nu}_0$ falls. Also the Q branch, if present would, appears in this gap.

1.3 Intensity of the spectral line

The intensity of the spectral lines in the ro-vibrational spectra depends on the population in the rotational levels (associated with each vibrational excitation) from which the transition occurs and the transition probability. The population of rotational states at certain energies under the condition of thermodynamic equilibrium can be described using statistical thermodynamics partition function. Now, in order to specify the probability of finding the system in a particular energy level, we must sum over the populations of all distinct quantum states with that energy. Alternatively, in thermal equilibrium at temperature T, the probability of finding a molecule in a particular energy level E_i is proportional to $g_i e^{-E_i/K_BT}$, in which g_i is total degeneracy in the level E_i and K_B is Boltzman constant. As the sum of the probabilities for all possible levels must add up to 1, the fraction of all molecules (of a given species) with energy E_i is can be represented by:

$$f_i(T) = \frac{g_i e^{-E_i/K_B T}}{\sum_i g_i e^{-E_i/K_B T}} \tag{1.32 b}$$

The denominator of the right hand side of equation (1.32 b) indicates the sum running over all possible distinct energy levels E_i, is called the molecular partition function.

For a rotating linear molecule the energy levels are specified by the total angular momentum quantum number J, and their energies are given by equations (1.22), (1.25) with degeneracy g_J = (2J+1). Hence the fraction of molecules with rotational energy, $F_v(J)=B_vJ(J+1)$ is given by:

$$\frac{N_J}{N_0} = f_J(T) = \frac{(2J+1)e^{-2B_v J(J+1)/K_B T}}{\sum_J (2J+1)e^{-2B_v J(J+1)/K_B T}} \tag{1.33}$$

From the equation (1.33) it is obvious that $f_J(T)$ is the product of two terms, (2J+1) which increases linearly with J, whereas the other term $e^{-2B_v J(J+1)/K_B T}$ demonstrates the significant decrease in $f_J(T)$ value with increase in J. Thus the competition between these two terms gives the overall behaviour shown by the solid curve in figure 1.7.

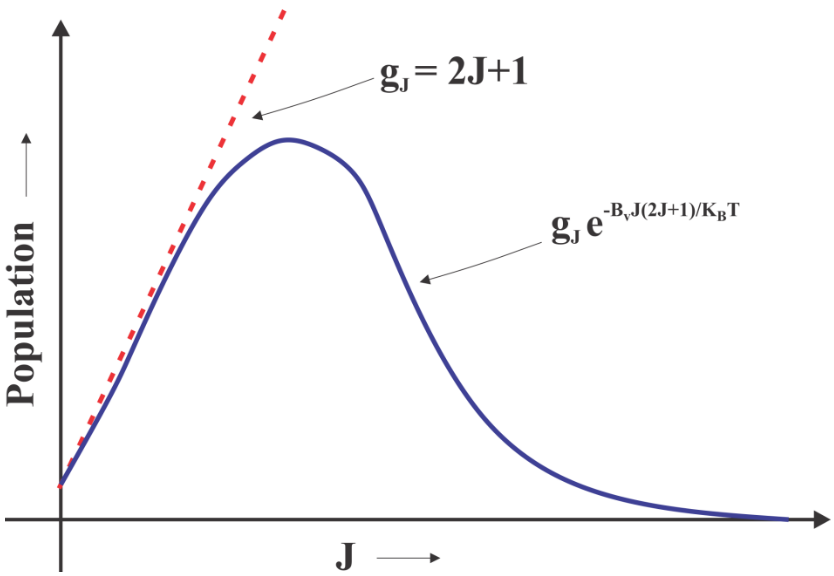

Figure 1.7 *Population distribution of rotating diatomic molecule at T ~ 296 K*

Therefore, to obtain the most highly populated rotational level, $\frac{d}{dJ} f_J(T) = 0$ which indicates J = $J_{max}(T) = \sqrt{\frac{K_B T}{2B_v}} - \frac{1}{2}$ is the most populated level at the given temperature.

Sometimes the centre of symmetry of a molecule has an interesting role in the alteration of the intensities in P and R branches of the ro-vibrational spectrum. Here the nuclear spin of the constituents atoms in a molecule determine the populations in the rotational levels. To illustrate this phenomenon, Pauli principle can be applied which states that total wavefunction of any molecule must be either symmetric or antisymmetric with respect to exchange of any indistinguishable nuclei. The wavefunction for the system of electrons (or the particles with half-integral spin) must be antisymmetric with respect to exchange of any two particles obey "Fermi-Dirac statistics". But the wavefunction for the system of neutrons (or the particles with integral spin) must be symmetric with respect to exchange of any two particles obey "Bose-Einstein statistics". Thus the electronic, vibrational, rotational and nuclear spin parts contribute to the total wavefunction and can be written as a product of them as shown in equation (1.34)

$$\psi^{total} = \psi^{el}\psi^{vib}\psi^{rot}\psi^{ns} \tag{1.34}$$

where ψ^{ns} is the nuclear spin wavefuncion. The ground state electronic and vibrational wavefunction for the linear molecules such as H-C≡C-H remains symmetrical with respect to exchange of the nuclei, whereas the rotational wavefunction (ψ^{rot}) is symmetric to exchange for even values of J and asymmetric to exchange for odd values of J. Therefore to satisfy the Pauli principle, ψ^{ns} will be asymmetric for even J and symmetric for odd J. In C_2H_2 molecule both the hydrogen nucleus are with I=1/2 nuclear spin and hence the two electrons in two ^{1}H nuclei can be combined to a triplet and a singlet function:

$$\psi^{ns} = \begin{bmatrix} \alpha(1)\alpha(2) \\ \beta(1)\beta(2) \\ \frac{1}{\sqrt{2}}\{\alpha(1)\beta(2)+\beta(1)\alpha(2)\} \end{bmatrix} \tag{1.35}$$

$$\psi^{ns} = \frac{1}{\sqrt{2}}\{\alpha(1)\beta(2)-\beta(1)\alpha(2)\} \tag{1.36}$$

where 1 and 2 are the two hydrogen atoms and α and β related to spin-up (↑) and spin-down (↓) state of the nuclei, respectively. Thus for each odd value of J, the three possible occupancies in ψ^{ns} and for even value of J, only one occupancy is possible in ψ^{ns}. Thus the molecule exhibits nuclear spin degeneracy (g_I) given by:

$$g_I = \begin{bmatrix} 3, \; for\, odd\; J \\ 1, \; for\, even\, J \end{bmatrix} \tag{1.37}$$

Therefore, including the spin degeneracy, the Boltzman distribution function to describe the populations in the lower rotational states is given by:

$$N_J \propto 3\,(2J+1)e^{-2B_v J(J+1)/K_B T} \;\; for\; odd\; J$$
$$and$$
$$N_J \propto 1\,(2J+1)e^{-2B_v J(J+1)/K_B T} \;\; for\, even\, J \tag{1.38}$$

Thus, the alternate rotational levels have the population differ by the ratio 3:1, resulting the alternation in intensity for P and R branch absorption lines in a given ro-vibrational spectra of C_2H_2 as shown in figure 1.8

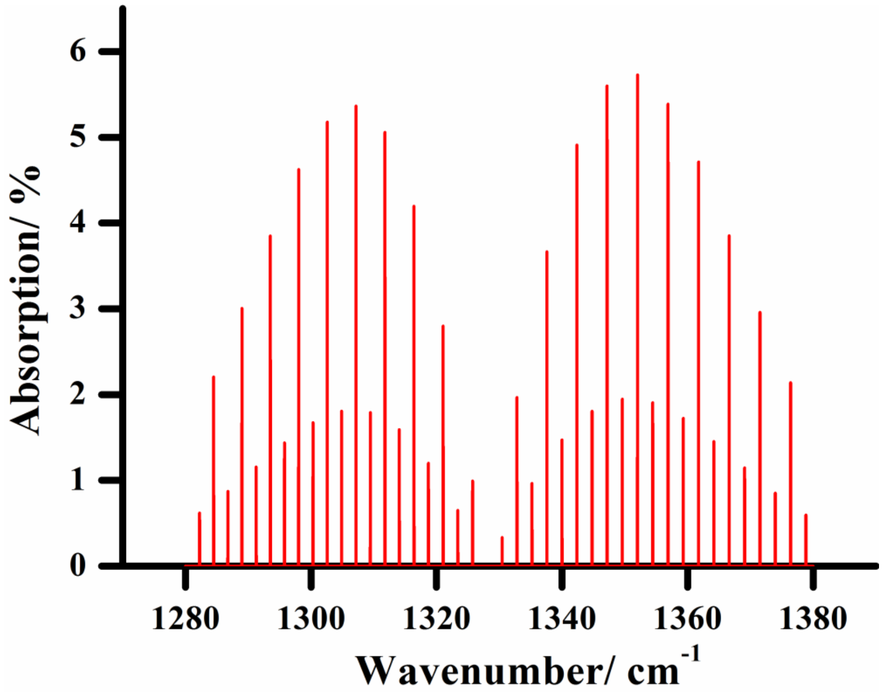

Figure1.8 *Hitran simulation of ro-vibrational spectra of C_2H_2 at 20 Torr pressure alteration of spectral line intensity for odd and even values of J.*

The intensity pattern of the ro-vibrational spectra of a heteronuclear diatomic molecule also depends on the transition probability. For electric dipole transitions, the integrated line strength G_{fi} (or integrated absorption cross section) is proportional to the absolute square of the matrix element of the electric dipole operator[17]:

$$G_{fi} = \frac{8\pi^3}{3hc}\left|M_{fi}\right|^2 \tag{1.39}$$

G_{fi} represents the appropriate integration over the molecular absorption cross section:

$$G_{fi} = \int \sigma_{fi}(\tilde{\nu})\tilde{\nu}^{-1} d\tilde{\nu} \tag{1.40}$$

and $$\left|M_{fi}\right|^2 = \sum_{\rho} \left[\langle f|\mu_\rho|i\rangle\right]^2 \tag{1.41}$$

where, the summation is taken over the components of the dipole moment operator in Cartesian co-ordinate system.

$$\mu = \sum_{\rho} \mu_\rho \hat{e}_\rho = \sum_i \vec{r}_i q_i$$

q_i s'are point charge particles in the molecules, $\vec{r}_i$ is the position vector the corresponding charge particles and $\hat{e}$ is unit vector. On evaluating the integral depicted in equation (1.40) and using the wave function depicted in equation (1.42) the intensities of the ro-vibration spectrum can be obtained.

$$\psi(R,\theta,\phi) = \Phi_{v,J}(R) Y_{J,\,M_J}(\theta,\phi) \tag{1.42}$$

where $\Phi_{v,J}$ (R) is the vibrational wavefunctions which are the solution of one dimensional Schrödinger equation with an effective J dependent potential. As vibrational wavefunction is R dependent, we can use the R dependent dipole moment function described by Mecke in 1950, shown in fig 1.9 and written in equation (1.43) to evaluate the vibrational transition moments.

$$\mu(R) = bR^n e^{-\alpha R} \tag{1.43}$$

where b, n and α are the adjustable parameters which govern the behaviour of $\mu(R)$. The homonuclear diatomic molecules do not exhibit electric dipole pure ro-vibration spectra, because μ(R) vanishes for symmetry reasons at all values of R.

The electric dipole moment function can be expanded with a Taylor series as described in equation (1.44)

$$\mu(R) = \mu(R_e) + \left(\frac{\partial \mu}{\partial R}\right)_{R=R_e}(R-R_e) + \left(\frac{\partial^2 \mu}{\partial R^2}\right)_{R=R_e}(R-R_e)^2 + \ldots \tag{1.44}$$

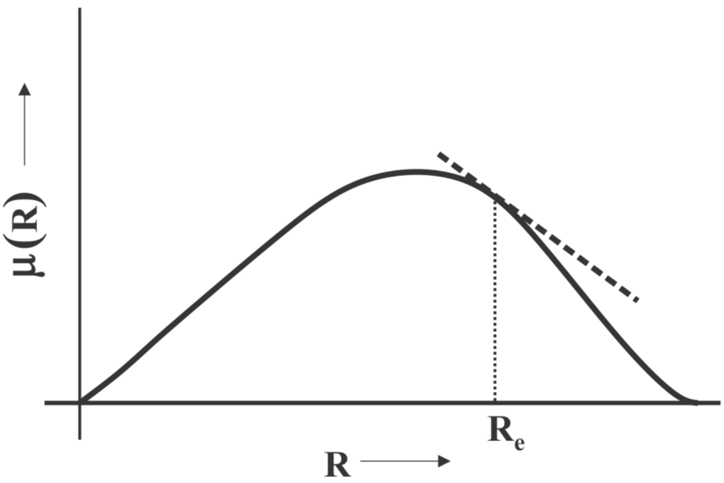

Figure 1.9 *Variation of dipole moment with internuclear distance in a heteronuclear diatomic molecule*

Thus the purely vibrational transition moments can be described as

$$M_{vv'} = \mu(R_e)\langle\psi_v|\psi_{v'}\rangle + \left(\frac{\partial\mu}{\partial R}\right)_{R=R_e}\langle\psi_v|(R-R_e)|\psi_{v'}\rangle + \left(\frac{\partial^2\mu}{\partial R^2}\right)_{R=R_e}\langle\psi_v|(R-R_e)^2|\psi_{v'}\rangle + \ldots \quad (1.45)$$

Since the vibrational wavefunctions ψ_v and $\psi_{v'}$ are the eignfunctions of the same Hamiltonian, they are orthogonal for v ≠ v':

$$\langle\psi_v|\psi_{v'}\rangle = \delta_{vv'} \quad (1.46)$$

Therefore, the leading term in equation (1.45) is

$$M_{vv'} = \left(\frac{\partial\mu}{\partial R}\right)_{R=R_e}\langle\psi_v|(R-R_e)|\psi_{v'}\rangle \quad (1.47)$$

Thus the strength of the vibrational band depends on the magnitude of the derivative of the dipole moment with inter-nuclear separation. Figure 1.9 shows, μ→0 when R→0, since the nuclei coalesce. For neutral diatomic molecules, μ→0 when R→∞ because the molecule dissociates into neutral atom. Therefore, μ has the maximum value between 0 and ∞. In the figure 1.9, the maximum occurs at $R<R_e$, giving a negative slope $\left(\frac{\partial\mu}{\partial R}\right)$ at R_e. If the maximum were occur at $R>R_e$, there would be a positive slope at R_e.

Considering the harmonic oscillator wavefunction, the selection rules are Δv = ±1 for the second term and Δv = 0, ±2 for the third term in equation (1.45). The nonlinear term provides the intensity for the overtone transition for Δv = 2. Again the linear term in the dipole moment $(\partial\mu/\partial R)_{Re}(R - Re)$ yields non-vanishing electric dipole matrix element for $|\Delta v| > 0$, when the anharmonic wavefunctions are used. Hence the mechanical anharmonicity govern the intensity of overtone transitions.

1.4 Line width and line-shape function of spectral line

The spectral lines in discrete absorption or emission spectra are not strictly monochromatic, but have the spectral distribution I(ν) about the central frequency $\nu_0 = \frac{E_f - E_i}{h}$, where E_f - E_i is the energy difference between the upper and lower energy level. The function I(ν) in the vicinity of ν_0 is called line shape or line profile. The frequency difference $\delta\nu = |\nu_2 - \nu_1|$ between the two frequencies ν_1 and ν_2 for which $I(\nu_1) = I(\nu_2) = I(\nu_0)/2$ is the full width at half maximum of the line (FWHM), also known as linewidth of the spectral line. A schematic diagram of a spectral line is shown in figure 1.10. There are several factors[18] which may contribute to the broadening of the spectral lines. In the following section, we will discuss about origins of various types of broadening in a spectral line.

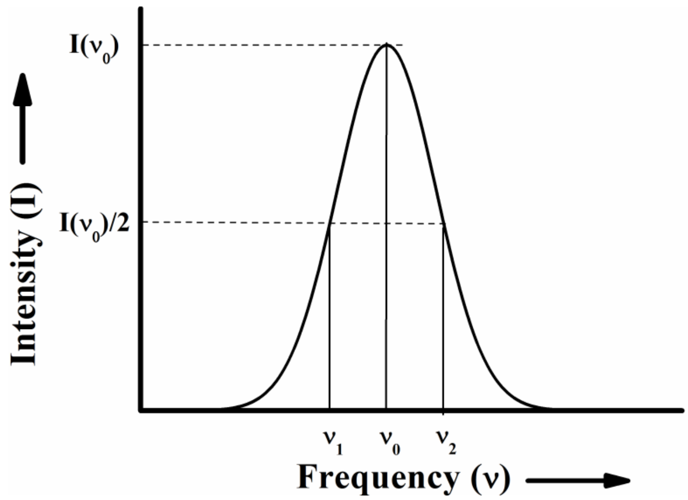

Figure 1.10 *Line shape of a spectral line with centre frequency ν_0 and FWHM $\delta\nu$ =* $|\nu_2 - \nu_1|$

1.4.1 Natural broadening

An excited atom or a molecule can emits its energy in the form of spontaneous emission and the electric field associated with the spontaneous radiation can written as $\xi(t)=\xi_0 e^{i2\pi\nu_0 t}e^{-t/2\tau_{sp}}$, where ξ_0 is the amplitude of the electric field and τ_{sp} is the spontaneous lifetime corresponds to transition from higher energy level to the lower energy level. It is observed that the electric field of the spontaneous emission decrease exponentially and the spectrum associated with the electric field can be obtained by taking the Fourier transformation of it[19]. Thus,

$$\begin{aligned}\tilde{\xi}(\nu) &= \int_{-\infty}^{+\infty}\xi(t)\,e^{-i2\pi\nu t}dt=\int_{0}^{\infty}\exp[i\,2\pi(\nu_0-\nu)t-t/2\tau_{sp}] \\ &= \frac{\xi_0}{1/2\tau_{sp}+i\,2\pi(\nu-\nu_0)}\end{aligned} \tag{1.48}$$

The power spectrum associated with the emission will be proportional to $\left|\tilde{\xi}(\nu)\right|^2$; hence the line shape function associated with the spontaneous radiation can be represented as

$$I(\nu)=\frac{1}{2\pi\tau_{sp}}\frac{1}{4\pi^2(\nu-\nu_0)^2+1/4\tau_{sp}^{\;2}} \tag{1.49}$$

and the normalized line shape function can be written as

$$I(\nu)=\frac{2\tau_{sp}}{\pi}\frac{1}{16\pi^2(\nu-\nu_0)^2\tau_{sp}^{\;2}+1} \tag{1.50}$$

The above functional form is known as Lorentzian line shape function and the full width half-maximum of the Lorentzian function is given by

$$\delta\nu_N=\frac{1}{2\pi\tau_{sp}} \tag{1.51}$$

The natural broadening can also be estimated from Heisenberg's uncertainty principle. A molecule resides in the excited level E_f with spontaneous lifetime τ_{sp} has the uncertainty in the energy $\Delta E\approx h/2\pi\tau_{sp}$. Since no excited state has the infinite lifetime, therefore there must have some broadening in the energy level in accordance with Heisenberg's uncertainty principle and the frequency of the transition terminating in the ground state has therefore the uncertainty $\delta\nu=\dfrac{1}{2\pi\tau_{sp}}$ which is same as FWHM of the spectral line in natural broadening. Thus shorter is the lifetimes of the states more broadening in spectral lines will occur.

1.4.2 Collision broadening

In a gas sample, the gas molecules randomly collide with each other and in this collision process, the energy levels of the molecules perturbed when the molecules come to very close due to their mutual interaction. When the colliding molecules are far apart, their energy levels are unperturbed but as the molecules come together their energy levels are perturbed and the frequency of the spectral line changes during the collision time ($\Delta\tau_c$). The collision time is very smaller (~10^{-13}sec) compared to the time between collisions (~10^{-6} sec) and thus the collision may be considered as almost instantaneous. Since the collision time is random, the phase of the wave after the collision is arbitrary with respect to the phase before collisions and each collisions result the random changes in phase and the spectra are no longer monochromatic. This type of broadening is called collision broadening or pressure broadening[19].

If τ_0 is the mean time between two collisions, the lineshape function for collision broadening can be represented as

$$I(\nu) = \left(\frac{\xi_0}{\pi}\right)^2 \frac{1}{2} \frac{1}{4\pi^2(\nu-\nu_0)^2 + 1/\tau_0{}^2} \tag{1.52}$$

which is a Lorentzian distribution and thus the normalized lineshape function will be

$$I(\nu) = \frac{\tau_0}{\pi} \frac{1}{1+4\pi^2(\nu-\nu_0)^2 \tau_0{}^2} \tag{1.53}$$

with FWHM of $\delta\nu_c = \dfrac{1}{\pi\tau_0}$ (1.54)

Thus a mean collision time of ~10^{-6} sec leads to the broadening in the spectral line of $\delta\nu_c$ = 0.3MHz (0.00001cm^{-1}). The linewidth of the spectral line due to collisional broadening can be minimized by working at low pressure. The rate at which the spectral lines become broadened with increase in air pressure are demonstrated by air broadening coefficient (γ_a) which can be determined from the linear relationship between the width of the broadened spectral feature and pressure of the colliding gas molecules used in the experiment.

1.4.3 Doppler broadening

In a gaseous state, the molecules can move randomly with all possible velocities from zero to infinity in any arbitrary direction in accordance with Maxwell-Boltzman statistics. During the motion of the gas molecules if they interact with an incident electromagnetic radiation, the frequency of spectral line apparently changes when it is observed by a stationary observer (e.g. optical detector); this is called the Doppler effect and the broadening in spectral line due to this effect is termed Doppler broadening[19]. If we consider that a radiation of frequency ν is passing through a collection of randomly moving molecules which have a resonant frequency ν_0 and a molecule interact with the incident radiation then the apparent frequency seen by the atom in its frame of reference be ν_0. If the radiation is assumed to propagate in z direction, then the apparent frequency seen by the molecule having z component of velocity v_z will be

$$\nu_0 = \nu(1 - v_z/c)$$
$$\Rightarrow \nu = \nu_0(1 - v_z/c)^{-1} \approx \nu_0(1 + v_z/c) \tag{1.55}$$

Hence the probability $I(\nu)d\nu$ that the frequency of the transition lies between ν and $\nu+d\nu$ is equal to the probability of z-component of velocity of the molecule lying between v_z and v_z+dv_z , where

$$v_z = \frac{(\nu - \nu_0)}{\nu_0} c \tag{1.56}$$

and the lineshape function is given by,

$$I(\nu) = \frac{c}{\nu_0}\left(\frac{M}{2\pi k_B T}\right)^{\frac{1}{2}} \exp\left[-\frac{Mc^2}{2k_B T}\frac{(\nu - \nu_0)^2}{\nu_0^{\;2}}\right] \tag{1.57}$$

which corresponds to Gaussian distribution and the and the FWHM of the lineshape function is given by, $\delta\nu_D = 2\nu_0\left(\frac{2k_B T}{Mc^2}\ln 2\right)^{\frac{1}{2}}$ (1.58)

where k_B is the Boltzman constant, M is the molecular weight and T is the absolute temperature of the gas.

Considering the molecular weight of carbon dioxide $M_{CO2} = 44\times1.67\times10^{-27}$ kg, the Doppler broadening due to vibrational transition near 10.6 μm at 300 K is found to be

$\delta \nu_D = 56$ MHz (0.00187 cm^{-1}). It is noteworthy to mention here that if the Doppler broadening and the pressure broadening contribute similarly in a particular experiment, then the spectral lines are used to fit with Voigt lineshape function which is a convolution of both the Gaussian and Lorentz lineshape function.

1.5 Techniques for the measurement of trace gases

1.5.1 Spectroscopic Techniques

Monitoring of different trace molecular species and volatile organic compounds (VOCs) have several important implications in biomedical and atmospheric science for better understanding of different physiological processes as well as the atmospheric chemistry. It is very important to perform an accurate and comparable measurement of the trace species to get a clear idea about their role in human health and demonstrating the changes in the atmosphere. Thus the necessity to identify and measuring the quantitative concentration of individual species lead to the development of different spectroscopic methods for detection of different trace molecular species and VOCs.

There are primarily two advantageous features of spectroscopic detection methods. Absorption spectroscopy is based on the Beer-Lambert law described in equation (1.59) provides the amount of absorption by the particular species to be directly related to the concentration of the species at the location of the measurements

$$\ln \frac{I}{I_0} = -\sigma [X] l \tag{1.59}$$

where I and I_0 are the light intensity of incident and transmitted radiation, respectively. σ is the wavelength dependent absorption cross-section, [X] is the concentration of the absorbing species and *l* is the pathlength through the sample. Additionally the spectroscopic fingerprint of the trace gases can sometimes be used as a unique identifying feature and prevents the need for time consuming sample preparation process. As these methods provide precise and real-time measurement of concentration of the trace gases, they are suitable for reliable, compact, robust *in situ* trace gas sensors. In this this section, we have described about different common and popular spectroscopic methods with their typical detection limits for monitoring the trace species in human exhaled breath and atmosphere.

1.5.1.1 Differential optical absorption spectroscopy (DOAS)

Differential optical absorption spectroscopy (DOAS) is an active remote measurement technique pioneered by Platt *et al*.[20] In this technique, either a thermal light source such as Xenon arc lamp, a broadband laser or natural light source such as sun, reflected light from moon or stars used as a source of radiation or a receiver placed several kilometres away to measure the concentration using the absorption spectroscopy technique. Thus the long pathlength provides the excellent sensitivity for this technique. The radiation received by the receiver, separate the light into discrete wavelength components for spectral analysis. Since the experiment is performed in open paths over the long path length of kilometres dimension, it limits the spatial resolution of the spectral lines. Moreover, the open path leads to absorption from a large number of trace species and from other absorbing/ scattering species such as aerosol, and the targeted species cannot be eliminated from the air along the analysis path. Thus the DOAS set-up does not provide the value for I_0 and concentration of the species cannot be estimated from Beer-Lambert law. However, the DOAS approach relies on measurement of the differential absorption cross-section to assess the concentration of the species of interest. This involves the separation of absorption into different wavelength (λ) components

$$\sigma_i(\lambda) = \sigma_{i0}(\lambda) + \sigma_i'(\lambda) \tag{1.60}$$

where σ_{i0} indicates low frequency of vibrations of absorption arises from scattering losses i.e. the difference between I_0 and 'true I_0' as shown in figure 1.11. The DOAS absorption cross section is denoted by the σ_i' term which exhibits rapid variation due to absorption by the analytes. The differential absorption cross-section is measured by comparing the intensity 'off' and 'on' resonance as shown in figure 1.11 at λ_1 and λ_2 respectively. On substituting the differential absorption and DOAS cross-section in equation (1.60), the concentration of the absorbing species can be evaluated[21]. The DOAS technique has been implemented for trace detection of iodine monoxide (IO)[22], hydroxyl radicals (OH)[23] and many other atmospheric pollutants such as NO_2, SO_2, O_3 *etc*[24-26].

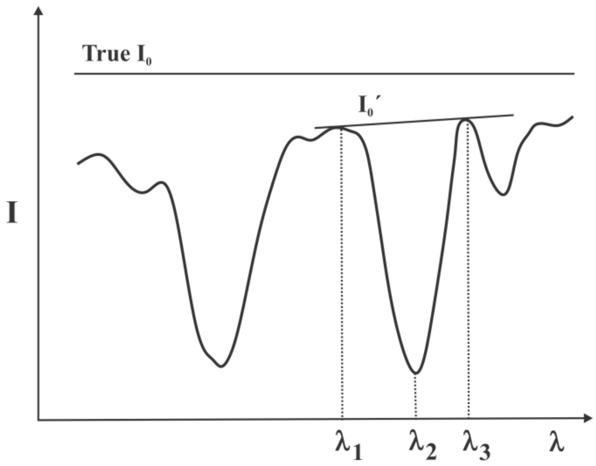

Figure 1.11 *An example of a DOAS spectrum*

1.5.1.2 Differential absorption lidar (DIAL)

Differential absorption lidar (DIAL) is a well-established technique to monitor the trace moleculer species in atmosphere[27]. The working principle of DIAL is same as the principle used in DOAS. In DIAL, two high energy pulses of radiation with a very small difference in wavelength, are directed into the measurement region and the Rayleigh and Mie scattering resulting from the molecules and aerosols, respectively in the backward direction towards the DIAL instrument is measured. In presence of absorbing species in the path between the source and the scatterer, 'on' resonance wavelength will be attenuated to a greater degree than the 'off' resonance wavelength. The time for detection of back scattered light after the initial light pulse is used to provide the range-resolved information as shown in figure 1.12.

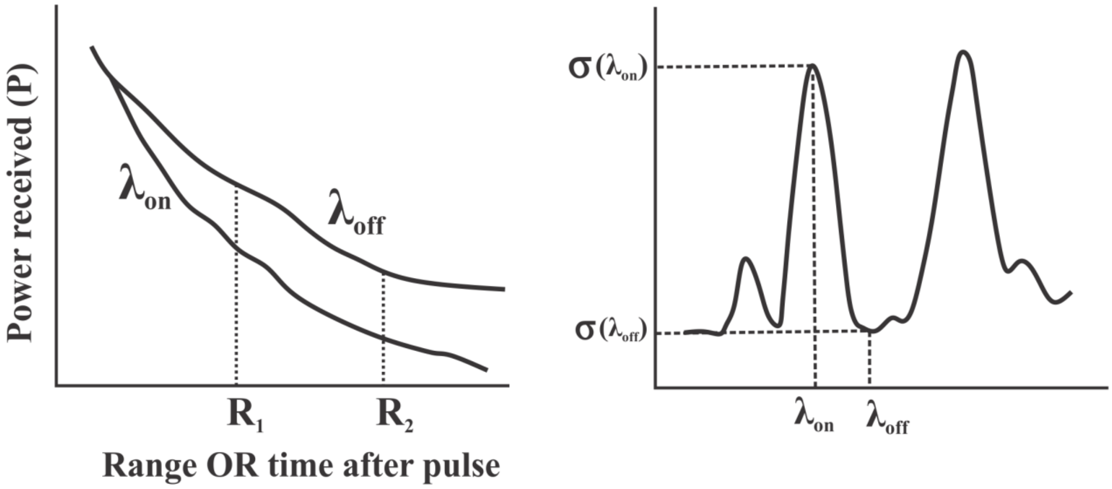

Figure 1.12 *The dial concept*

In the range of R1 and R2, the average concentration can be determined from the ratio of the backscattered signal (P) at the 'on' and 'off' resonance wavelength in accordance with equation (1.61).

$$[X] = \frac{1}{2(R_2 - R_1)(\sigma(\lambda_{on}) - \sigma(\lambda_{off}))} \ln\left(\frac{P_{on}(R_1) \times P_{off}(R_2)}{P_{off}(R_1) \times P_{on}(R_2)}\right) \tag{1.61}$$

1.5.1.3 Tuneable diode laser absorption spectroscopy (TDLAS)

Tuneable diode laser spectroscopy (TDLAS) is widely used to measure the concentration of trace molecular species in exhaled human breath sample as well as atmospheric sample[28]. It is a highly sensitive direct quantitative measurement technique in which multipass absorption cell such as White cell[29] or Herriott cells[30] are used with a tunable diode laser, most commonly lead-salt diode laser operating in the mid-IR spectral range to achieve the excellent detection limits. These mid-IR lasers often required the cryogenic cooling and hampered by multi-mode emission. Recent technological advancement leads to availability of low cost, user friendly laser device that operates in room temperature with a relatively high output (mW) of narrow bandwidth emission in the near-IR which limits the sensitivity of the technique because the researchers can access the weaker vibrational overtone transitions and combination band of most of the molecular species in NIR region.

However, the conventional absorption technique require measurement of small changes compare to large background signal, TDLAS is often combined with wavelength modulation or frequency modulation spectroscopy which indicates two fold benefits of the present technique. Firstly, it produces the different signal that is proportional to the concentration of the sample and secondly, it allows the signal to be detected at a frequency in which laser noise is significantly.

A variety of IR- Lasers have been coupled with a TDLAS to monitor the exhaled breath and atmospheric constituents. For example Lachish *et al.*[31] demonstrated the detection limit of 1 ppm of NH_3 in exhaled human for breath with an integration time of 10 sec using a diode laser operating at the central wavelength 11 μm. Moskalenko *et al.*[32] reported the detection limit of 0.5 ppm CO in the spectral range of 4.6 μm using the TDLAS technique. Wysocki *et al.*[33] reported the detection limit of 1.2 ppb of OCS in exhaled breath in the spectral range of 4.86 μm using the same technique.

Rehle *et al.*[34] demonstrated the detection limit of 320 ppt of HCHO using a tunable diode laser operating at 3.53 μm. Moreover, the TDLAS technique can be employed to measure the concentration of the atmospheric trace species such as N_2O, HONO, HNO_3, NO_2 etc.

1.5.1.4 Diode laser frequency chirping (DLFC)

Diode laser frequency chirping is an useful tool for detection molecular species in analytical chemistry exploiting the absorption spectroscopy technique. A square wave signal is used as a pulse to laser controller at a repetition rate less than 1 KHz to chirp the frequency of the laser. When the drive current of the laser exceeds some threshold value, the diode begins to emit laser radiation. The temperature of the diode increases with flow of current which in turn increases the refractive index and length of the laser medium results the change in the wavelength of the emitted radiation. This process is known as frequency chirp. The change in wavelength does not follow the linear wavelength scale in time, therefore to convert the nonlinearity into the linear wavelength or frequency scale, an etalon is employed to monitor the wavelength of the output radiation. To determine the concentration the smaple is scanned over a small spectral range of interest at high repetition rate. In principle, such fast scanning indicates acquisition and summation of more than 1000 spectra per second and rapid averaging improves the signal to noise ratio and hence the detection limit. Lindley *et al.*[35] reported the detection limits of 21 ppmv and 49 ppbv for a 4 sec optimum integration time in a single and multi-pass cell respectively employing two frequency chirped *cw*-DFB lasers operating at the centre wavelengths of ~ 1.52 μm and 1.535 μm. The detection limits mentioned here are not sufficient for monitoring the C_2H_2 concentration in the ambient air, but the rapid data acquisition rate of this technique facilitates the measurement the concentration in plasma and flames.

1.5.1.5 Laser photoacoustic spectroscopy (PAS)

Photoacoustic spectroscopy (PAS) is based on the photoacoustic effect, in which acoustic waves result from the absorption of radiation and the acoustic signal is directly related to the concentration of the analytes. In contrast with other mid-IR absorption techniques, PAS is an indirect technique in which laser beam impinges on a selected target gas and the effect on the absorbing medium is studied rather than the direct absorption of the light by the gas molecules. Light, from either pulsed or chopped *cw*-laser sources produces a transient temperature rise in an absorbing medium via non-radiative relaxation processes, which then translates into a pressure change or sound wave and detected with a sensitive microphone. The amplitude of the output electrical signal from the microscope is proportional to the concentration of the absorbing species in the cell. PAS is ideally a background-free technique but in real experiment background signals come from non-selective absorption of the gas cell windows, outside acoustic noise, scattering of the laser radiation by aerosols onto the microphone. Since the PAS signals are proportional to the pump laser intensity and therefore PAS is mostly used with high-power laser sources, in particular CO_2 and CO lasers to achieve the good detection limits[36].

The key features of the photoacoustic technique include (1) excellent detection sensitivities down to sub-ppbv concentrations with powers in the watt range, (2) a large dynamic range, (3) PAS detector responsivity is almost independent of the pump wavelength, and (4) a PAS signal that is directly proportional to the absorbed radiation intensity, but does not scale with pathlength as with the previously discussed signal enhancement techniques. Indeed, the PAS signal will increase if a laser beam passes through the same volume/detection area of a microphone. A detection limit of 100 ppbv of ammonia (NH_3) has been reported by Paldus *et al.*[37] using a cryogenically cooled *cw*-QC-DFB laser with a 16mW power output at 8.5 μm whereas Schilt *et al.*[36] demonstrated a detection limit of 0.1 ppbv of NH_3 using a CO_2 laser for the trace detection of ammonia. Other trace atmospheric species such as nitrious oxide (N_2O), ethane (C_2H_6), ethene (C_2H_4) have been monitored with sensitivities ppbv down to pptv range using PAS technique[38-42]. Furthermore Puiu *et al.*[43] reported the detection of ethane and ethylene in human exhaled breath in the spectral range of 3.3 μm and 10.5 μm respectively using the PAS technique. Using the same technique Angelmahr *et al.*[44] described the detection limit of 3 ppb HCHO in exhaled breath using a tunable laser at 3.53 μm.

However, in trace gas sensing applications, PAS is limited to extractive point monitoring due to the requirement of an absorption cell. Additionally, PAS requires sufficient sampling pressures ($\approx$ 100Torr − 1 atm) for efficient collisional transfer and generation of the acoustic waves, thus limiting the selectivity in some cases.[45] Furthermore, the effective collisional transfer can depend on the relative composition of the gas sample.

1.5.1.6 Laser induced fluorescence (LIF)

Laser induced fluorescence (LIF) technique is a direct quantitative absorption technique to determine the concentration of trace species in atmospheric as well as in exhaled human breath. In this method, the absorption transition occurs from a lower electronic state to some vibrational levels of an upper electronic state and then the molecule lose vibrational energy through collisions with other molecules and reach to the lowest vibrational state of the excited electronic level. The process is often more rapid than spontaneous emission of radiation, so that when the molecule finally re-emits the radiation from the lowest vibrational state, the emitted wavelength become longer than the absorb radiation of the near UV or visible light, can then be detected. At low concentration of the analytes, the fluorescence intensity is proportional to the sample concentration which leads to the careful calibration of the apparatus. Since fluorescence has a very low background, greater sensitivity can thus be achieved which further exploits the advantage of LIF technique over other absorption spectroscopy techniques. However, the technique is suitable for those molecules (OH^-, CN^- etc.) which have bound and optically accessible upper electronic states. Collisional quenching of fluorescence signal are often occur at atmospheric pressure and Rayleigh scattering of the laser by air molecules give the background signal. These are the two major challenges in LIF technique. To overcome the problems, samples are often expanded into low pressure vacuum chamber for detection and this reduces the concentration of targeted species in the sample and excellent sensitivity has been achieved. This is called fluorescence assay by gas expansion (FAGE)[46]. Bloss *et al.*[47] reported the sensitivity of 3.1×10^5 molecule/cm^3 and 2.6×10^5 molecule/cm^3 corresponds to the detection limits of 0.012 pptv and 0.09 pptv for OH and HO_2 respectively using this FAGE method. This method is also extensively used for atmospheric monitoring of other different species such as SO_2, NO, NO_2, IO[46-51] *etc*.

1.5.1.7 Cavity Enhanced Spectroscopy

Cavity Enhanced spectroscopy techniques are relatively new, highly sensitive, laser-based direct absorption spectroscopy technique. Cavity ring down spectroscopy (CRDS) was the first cavity enhanced technique pioneered by O'Keefe and Deacon in 1988 to detect the atmospheric oxygen in an open air cavity[52]. In CRDS experiment, the decay rate of light intensity is measured instead of measuring the transmitted light intensity in conventional spectroscopy techniques. In CRDS, light is trapped inside a high finesse optical cavity and both the *cw*-laser and pulsed laser can be used as a source of light. The basic operation principle, practical implementation of CRDS technique with it advantageous features has been demonstrated in the next chapter.

Cavity enhanced absorption spectroscopy (CEAS) is an another cavity enhanced technique in which laser light is injected into the cavity slightly in an off-axis alignment so the cavity behaves like a multi-pass cell and supports a near continuum of frequencies[53]. The frequency of the laser is swept over a small spectral range at fast repetition rate, allows accumulation of several spectra in a short time which in turn improves the signal to noise ratio and thus detection limit.

The high sensitivity of the cavity enhance techniques make them attractive for development of optical sensors for trace gas analysis. Moreover, the compact instrumentation, good temporal resolution and direct quantitative measurement of the absorber concentration facilitates the use of the techniques in real time monitoring of trace molecular species in atmosphere and exhaled human breath. Diode laser based CRDS or CEAS techniques are popular because of the low cost of the laser sources and therefore have found extensive applications for *in situ* measurements of the atmospheric trace constituent. However the availability of new generation external cavity quantum cascade lasers (EC-QCLs) coupled with high resolution cavity enhance techniques opens up a new direction in atmospheric and biomedical research. In the present thesis, we demonstrated the applicability of EC-QCL and DFB laser based cavity enhanced system as a next generation diagnostic tool in modern medical science and simultaneously the system may be employed for real time monitoring of trace species in the atmosphere. Furthermore, such high resolution system can be employed for fundamental molecular spectroscopic studies. In this sub-section, the novel features of the cavity enhance spectroscopy in different applications have been highlighted.

In 1991 Gustafsson *et al* first reported the presence of endogenous nitric oxide (NO) in exhaled breath of humans and animals[54]. The American Thoracic Society recommends that an NO detection system has a sensitivity of 1 ppb and response time <0.5 s[55,56]. Nelson *et al*.[57] reported the measurement of NO in air with a detection limit <1 ppb using a thermoelectrically cooled pulsed QCL operating at 5.26 μm coupled with a multi-pass cell. Kosterev *et al.*[58] reported the measurement of NO in using a QC-DFB laser operating at 5.2 μm and single ring-down event sensitivity to absorption of 2.2×10^{-8} cm^{-1} was achieved. Rao *et al.*[59] demonstrated detection of NO_2 in zero air using a tunable QCL operating at 6 μm coupled with a cavity ring down spectrometer and sensitivity of 1.2 ppb has been reported. Wang *et al.*[60] reported the detection of acetone in exhaled breath using a single-mode Q-switch Nd:YAG laser (λ ~266 nm) based cavity ring-down spectrometer and a range of 0.80 to 3.97 ppmv of acetone have been measured for Type 1 Diabetes (T1D) subjects which is higher than the mean acetone concentration of 0.49 ppmv in non-diabetic healthy subjects. Employing the same technique Corrosion *et al*.[61] reported the isotope selective measurement of breath CO_2 ($^{13}CO_2/^{12}CO_2$) using a DFB laser (λ ~1.6 μm) with a precession of 0.2‰. Recently, N_2O gas analyser[62] (capable of measuring on N_2O isotopes and concentration in atmosphere) working on CRDS principle is commercially available which exhibits a precession of 0.5‰ for *in situ* measurement of N_2O isotopes in atmospheric sample. Parks *et al*.[63] demonstrated the detection of N_2O in atmosphere using a near infrared external cavity diode laser (NIR-ECDL, λ ~1.525 μm) coupled with cavity ring down spectrometer and a limiting sensitivity of mixing ratio of 23ppm at 1 atm pressure was reported[64]. The same research group demonstrated the detection of hydrocarbons such as ethylene and ethane with a limiting sensitivity of mixing ratios' of 21 ppb and 222 ppb, respectively using the CRDS technique. Pradhan *et al*.[65] reported the mixing ratios' of C_2H_2 of 1.8 ppb and 3.87 ppb in outdoor and indoor air sample respectively using a NIR Laser based cavity ring down spectrometer. Fawcett *et al.*[66] reported the detection of CH_4 in ambient air via $2\nu_3$ overtone band and a detection limit of ~ 52 ppb was achieved which low enough to monitor tropospheric CH_4 (average mixing ratio~1.7 ppm) Brown *et al.*[67] reported the in situ measurement of atmospheric NO_3 by CRD spectrometer coupled with a pulsed dye laser of narrow bandwidth. Simultaneously Simpson *et al*.[68] described the monitoring of N_2O_5 with a detection limit of 2.4 ppt using a diode laser (λ~662 nm) based CRDS system. A portable *cw*-CRDS instrument employing a diode laser in a visible range (λ ~ 410 nm) was used to measure the atmospheric NO_2 in an urban environment with an estimated detection limit of 100 ppt[69].

Broadband cavity ring–down spectroscopy (BB-CRDS) is an alternative to cavity enhance spectroscopy method that has been used to monitor atmospheric NO_3[70]. In BB-CRDS a broadband light source is used to excite an optical cavity and the entire spectrum is recorded on a broadband charge couple device (CCD). A broadband Nd:YAG pumped dye laser coupled with a BB-CRDS instrument was used to monitor I_2, IO_2, NO_3 and N_2O_5 in North Atlantic Marine Boundary Layer Experiment (NAMBLEX) in 2002 and the detection limits between 1-20 pptv have been reported with integration time of 100s to 10 min[71]. Compact light emitting diodes (LEDs) based BB-CRDS instrument has been used for measurement of atmospheric NO_2 in the laboratory and a detection limit of 100ppt with 60s integration time was reported[72].

Optical cavity feedback CRDS (OF-CRDS) is an alternative to CRDS and also has potential for monitoring the trace molecular species[73]. Light from a *cw* laser is injected to the cavity and coupled into a fixed length cavity by chirping the laser until the laser frequency matches with the cavity mode. As soon as the overlapping between the laser frequency and the cavity mode occur, a feedback is sent to the laser to fix it frequency and intensity is build up inside the cavity. At the end of the current pulse the laser is extinguished and exponential decay of light inside the cavity is recorded by an optical detector. The OF-CRDS technique provides the high temporal resolution due to the repetition rate at which the laser frequency may be chirped. The technique has been employed for sensing of CH_4 and HF and the baseline noise level equivalent to 2.5×10^{-8} cm^{-1} with a ring-down time of 14μs has been reported. Butler *et al.*[74] demonstrated OF-CRDS measurement of single aerosol particles in atmosphere employing a NIR diode laser λ ~1.65 μm.

Off-axis CEAS has the similar sensitivity to cw-CRDS and provide rapid measurement of certain trace species in exhaled breath. Silva *et al.*[75] demonstrated the off-axis CEAS measurement of NO concentration in exhaled breath using a EC-QCL at 5.2 μm with detection limit of 1 ppb within the integration time of 4 sec. Using the same technique and the same light source McCurdy *et al.*[76] demonstrated the measurement of NO in exhaled breath and the detection limit of 400 ppt has been reported. Miller *et al.*[77] reported detection limit of 150 ppb of HCHO using a interband laser (λ ~ 3.53μm) coupled with OA-CEAS system. Parameswaran *et al.*[78] reported the measurement of ethane in exhaled breath using a mid-IR interband laser with detection limit of 0.12 ppb. Exploiting the same technique the isotope selective measurement of $^{13}C/^{12}C$ and $^{18}O/^{16}O$ isotope ratios in exhaled breath CO_2 have been performed with precession of 0.02‰ and 1‰, respectively[79]. Baer *et al.*[80] reported the measurement of concentration of numerous trace gases (Such as CO, CH_4 etc) in the ambient urban atmosphere using the Off-axis CEAS technique and detection limit of ~1 ppb in 1 sec integration time at $\lambda \sim 1.653$ μm. Measurement of dilute NH_3 and C_2H_2 have been performed with detection limits of 2 and 0.3 ppbv, respectively employing a NIR diode laser at $\lambda \sim 1.531$ μm.

Although theses cavity enhances techniques provide excellent sensitivity for quantitative detection of concentrations of trace molecular species, their applications are limited due to unavailability of widely tunable laser. But the recent development of mid-IR widely tunable continuous wave external-cavity quantum cascade laser with mode-hop-free (MHF) tuning features opens up a new frontier area of research for development of novel gas sensors to detect a variety of molecules by probing their fundamental ro-vibrational absorption lines. Certain cavity enhance absorption techniques employing actively locked cavities, particularly Noise-Immune Cavity-Enhanced Optical Heterodyne Molecular Spectroscopy (NICE-OHMS)[81,82] have exhibit significant better sensitivity than NIR *cw* CRDS. However the considerable technical difficulties to maintain a lock between diode laser and high finesse cavity hinder their use as a particular optical sensor. Nevertheless, all these developments have suggested the progress in research of next generation optical sensor technology for monitoring the trace components in exhaled breath as well as in atmosphere.

1.5.2 Non – spectroscopic detection methods

Monitoring of trace constituents in atmospheric sample or exhaled breath which do not rely on the spectroscopic discrimination for selectivity, either gas chromatographic (GC) separation or mass spectrometry commonly use to distinguish between the species and then different analytical detectors are exploited for subsequent detection. In this section, we have discussed about GC separation and detection in which sample pre-concentration is used to enhance the concentration of the trace species prior to GC separation and that leads to achieve sensitivities below the atmospheric mixing ratios of trace gas species. Finally, we have discussed about the mass spectroscopy (MS) technique for monitoring the trace species.

1.5.2.1 Gas chromatographic separation and detection

The processes involved in GC separation and detection may be divided in four stages: sample acquisition, preparation and injection, separation and detection. Analysis of trace molecules may be performed either *in situ* or post acquisition, depending on the stability of species of interest. Post-acquisition generally involves collection of the sample in a teflon coated containers or Tedlar bags for analysis in the laboratory in later date. This method is suitable for the species which are unreactive whereas *in situ* analysis is recommended for the unstable molecules such as PAN. The sample acquisition method also involve passing of gas sample through a trap containing the selective absorbent material, such that the molecules of interest are retained in the trap whilst the remaining species in the sample are flowed into vent. The trap then heated to desorb the retain molecules and analysed in the laboratory.

The molecules those are present in relatively higher concentrations in the atmosphere (such as CH_4), the direct injection into GC column gives the detection limit below the atmospheric concentration. But for the analysis of the trace species in the atmosphere, sample pre-concentration is necessary before GC separation. A large volume of sample is passed through an absorbent trap which retains a small fraction of the molecules in the original sample. The molecules then thermally desorbed from the trap and a small volume of the carrier gas is used to transfer them directly into the GC column. Subsequently, the species are separated depending on their affinity for the stationary phase of the column and detected by the suitable detector. A chromatogram is obtained and the area under the each peak associated with the concentration of the individual species.

Water removing is necessary before passing the sample through the absorbent trap, particularly if the trap is maintained at sub-ambient temperature. Condensation of water onto the absorbant reduces the trapping capacity and the formation of ice may cause the blockage. Water may also affect some GC columns and detection system. Water removal is commonly done by using a Nafion dryer, in which a sample is passed along a tube with a counter flow of dry gas, separated by a memebrane that is permeable to highly polar water molecules. A sharp concentration gradient promotes osmosis of the water from the sample to dry gas.

The concentration of the trace species eluting from a GC column is measured by the various commercially available detectors. Flame ionisation detector (FID), electron capture detectors (ECD) etc. are attached with a GC column and widely used for the detection purposes. A comprehensive description of these detectors may be found in different literatures[83,84]. In brief, FID is generally used for detection of hydrocarbons (HC) because of its simplicity, high sensitivity and good linear response across a wide range of concentration[85,86]. The ECD is highly sensitive to electrophilic compounds such as halocarbons and remain inactive to HC[85,87,88]. However, all the detector mentioned here require careful calibration for precise analytical measurement which is usually done by standard gas sample. After successful calibration the system is ready to provide the quantitative and reliable measurements. At present fully automated computer controlled GC-FID/ECD instruments are commercially available and extensively used in biomedical and atmospheric research.

1.5.2.2 Mass spectrometry

Mass spectroscopy is based on ionisation of the molecule and subjected them to an electromagnetic field through which ions with different mass/charge (m/z) ratio follow different trajectories and thus they are separated. Subsequently, the ions are detected by a detector and may be identified individually. The ions are formed through highly energetic processes such as electron impact and fragmentation occurs which provide the mass spectrum of the sample. However, it is more difficult to identify and quantify of the individual species using the mass spectrum. Hence, the GC separation is required to achieve the selectivity in the measurement. But GC separation sometime limits temporal resolution, making GC-MS not suitable for real time sample analysis.

Chemical ionisation mass spectrometry (CIMS) is another technique which may be used to avoid GC separation. In CIMS technique, the high energetic electron impact is prevented and the gas sample is ionised by charge-transfer reaction mechanism which is less energetic. As a result, the ions are relatively stable and tend not to fragment before detection. The reagent ions are generated by electron attachment or electron impact ionisation before reaction with the sample gas, and the generated ions are usually mass selected using a quadruple mass spectrometer before detection. A wide variety of reagent gases are used in CIMS for ionisation of the sample molecules including methane, ammonia and isobutane[89]. The technique is also used for detection of ethanol, acetone and isoperene in exhaled breath. Moreover, it has been used for detection of trace atmospheric species including HO_2 and RO_2 via reaction of NO and SO_2[90] and isoperene whereas the VOCS are detected via reaction with benzene cations[91].

Proton transfer mass spectrometry (PRT-MS) is an alternative of CIMS in which H_3O^+ ions are used to protonated the VOCs. The reagent ion i.e. H_3O^+ are generated by ionisation of water vapour using gas glow discharge and subsequently passing through a drift tube which is flushed with a gas sample such as air. The H_3O^+ exclusively protonate the VOCs as they have higher affinity than water and the reaction with other the inert species (e.g. N_2, O_2, Ar and CO_2) do not occur as they have lower proton affinities to water. Since proton transfer is a non-dissociative process, it only produces one product ion corresponds to each VOCs. For those species that do dissociate, the products that are formed follow the predictable pathway to facilitate the identification.

The rapid detection of VOCs and their quantitative measurement at very low concentration (10-100 pptv) is possible using the equation (1.62) if the reaction rate constant for protonation and the reaction time is known[92].

$$[R] = \frac{1}{kt}\frac{[RH^+]}{[H_3O^+]} \tag{1.62}$$

High sensitivities in PRT-MS technique is achieved when the ratio of the product ion signal to the density of neutral compound is high, thus sufficient time for reaction in the drift tube is necessary. But the identification of ions with the same mass is still challenging and clustering of water molecules around the product reduces the sensitivity of the technique. However, the technique can be applied to numerous applications in exhaled breath analysis and atmospheric monitoring and is a powerful tool for detecting large numbers of VOCs[93-95].

1.6 References

1. C. N. Banwell, E. M. McCash, *Fundamentals of molecular spectroscopy*, 1993 (Tata McGraw-Hill Publishing Ltd, New Delhi).

2. P. W. Atkins, *Physical Chemistry*, 2002 (Oxford University Press).

3. R. J. Le, Roy, *A Spectroscopy Premier*, 2003 (Lecture notes, University of Waterloo).

4. J. Wojtas, Z. Bielecki, T. Stacewicz, *Opto-Electron. Rev.*,2012, **20**, 26.

5. J. Wojtas, *Sensors*, 2015, **15**, 14356.

6. M. R. McCurdy, Y Bakhirkin, G. Wysocki *et al*., *J. Breath Res*., 2007, **1**, 014001.

7. R. Goody, *Principles of Atmospheric Chemistry and Physics*, 1995 (Oxford University Press).

8. B. Fawcett, *Diode laser based cavity ring-down spectroscopy for the measurement of trace gases*, PhD Thesis, University of Bristol, 2003.

9. V. I. Stsiapura, V. K. Shuali, B. M. Gaston, *Anal Chem*., 2015, **87**, 3345.

10. R. Engeln, G. Helden, A. J. A. Roij, *J. Chem. Phys*., 1999, **110**, 2732.

11. S. Mackenzie, *High Resolution Molecular Spectroscopy* (Lecture Notes 1-7, University of Chembridge).

12. J. V. Auwera and A. Fayt, *J. Mol. Struct*, 2006, **780**, 134.

13. A. G. Maki, *J. Phys. Chem. Ref. Data*,, 1974, **3**, 221.

14. K. Sung, R. A. Toth, L. R. Brown *et al*., *Quant. Spectrosc. Radiat. Transf*., 2009, **110**, 2082.

15. F. K. Tittel, D. Richter, and A. Fried., *Topics Appl. Phys*., 2003, **89**, 445 (Springer-Verlag Berlin Heidelberg).

16. Y Yao, A. J. Hoffman and C. F. Gmachl, *Nature Photonics*, 2012, **6**, 432.

17. S. Albert, K. K Albert and H. Hollenstein, *Handbook of High-Resolution Spectroscopy*, 2011, **1** (Wiley Chichester).

18. G. Peach, *Contemp. Phys*., 1975, **16**, 17.

19. A. Ghatak, K. Thyagrajan, *Optical Electronics*, 1989 (Chembridge University Press).

20. U. Platt, D. Perner, H. W. Patz *et al*., *J. Geophys. Res*., 1979, **84**, 6329.

21. M. W. Sigrist, *Air Monitoring by spectroscopic Techniques* (Wiley-Interscience, New-York, 1994).

22. B. J. Allan, G. McFiggans, J. M. C. Plane *et al*., *J. Geophys. Res*., 2000, **105**, 14363.

23. D. E. Heard and M. J. Pilling, *Chem. Rev*., 2003, **105**, 5163.

24. G. Honninger, U. Platt, *Atmos. Envir*, 2002, **36**, 2481.

25. H. Edner, P. Ragnarson, S. Spannare *et al*., *Appl. Opt*., 1993, **32**, 327.

26. U. Platt and D. Perner, *J. Geophys. Res*., 1980, **85**, 7453.

27. E. R. Murry and J. E. van der Laan, *Appl. Opt*., 1978, **17**, 814.

28. E . D. Hinkley, *Appl. Phys. Lett*., 1970, **16**, 351.

29. J. U. White, *J. Opt. Soc. Am*, 1976, 66, 411.

30. D. R. Herriott and H. J. Schulte, *Appl. Opt*., 1964, **4**, 883.

31. U. Lachish, S. Rotter, E. Adler *et al*., *Rev. Sci. Instrum*. 1987, **58**, 923.

32. K. L. Moskalenko, A. I. Nadezhdinskii and I. A. Adamovskaya, *Infrared Phys. Tech*. 1996, **37**, 181.

33. G. Wysocki, M. McCurdy, S. So *et al*., *Appl. Opt*. 2004, **43**, 6040.

34. D. Rehle, D. Leleux, M. Erdelyi *et al*., *Appl. Phys. B: Laser Opt*. 2001, **72**, 947.

35. R. E. Lindley, M. Pradhan, and A. J. Orr-Ewing, *The Analyst*, 2006, **131**, 731.

36. S. Schilt, L. Thevenaz, M. Nikles *et al*., *Spectrochemica Acta Part A*, 2004, 3259

37. B. A. Paldus, T. G. Spence, R. N. Zare *et al*., *Opt. Lett*., 1999, **24**, 178.

38. M. Jahjah, W. Ren, P. Stefanski *et al*, *Analyst*, 2014, **139**, 2065.

39. J. P. Lima, H. Vargas, A. Miklos, M. Angelmahr and P. Hess, *Appl. Phys. B*, 2006, **85**, 279.

40. A. A. E. Martis, S. Buscher, F. Kuhnemann *et al*., *Instrum. Sci. Technol*, 1998, **67**, 177.

41. F. M. J. Harren, F. G. C. Bijen, J. Reuss *et al*., *Appl. Phys. B*, 1990, **50**, 137.

42. T. Fink, S. Buscher, R. Gabler *et al*., *Rev. Sci. Instrum*., 1996, **67**, 4000.

43. A. Puiu, G. Giubileo, C. Bangrazi *et al*., *Int. J. Environ. Anal. Chem*. 2005, **85**, 1001.

44. M. Angelmahr, A. Miklos and P.Hess, *Appl. Phys. B: Lasers Opt*., 2006, **85**, 285.

45. A. Fried and W.W. Berg, *Opt. Lett*., 1983, **8**, 160.

46. D. E. Heard, M. J. Pilling, B. J. Whitaker, *J. Chem. Soc. Faraday Trans*., 1997, **93**, 2907.

47. W. J. Bloss, T. J. Gravestock, D. E. Heard *et al*., *J. Environ. Monit*., 2003, **5**, 21.

48. I. R. Sims and I. W. M. Smith, *J. Chem. Soc., Faraday Trans*., 1988, **84**, 527.

49. Y. Matsumi, H. Shigemori and K. Takahasi, *Atmos Enviro*., 2005, **39**, 3177.

50. E. J. Lanzendorf, T. F. Hanisco, N. M. Donahue *et al*., *Geophys. Res. Lett*., 1997, **24**, 3037.

51. J. A. Thornton, P. J. Wooldridge and R. C. Cohen, *Anal. Chem*., 2007, **58**, 19.

52. A. O’Keefe and D. A. G. Deacon, *Rev. Sci. Instrum*., 1988, **59**, 2544.

53. A. O’Keefe, *Chem. Phys. Lett*., 1998, **293**, 331.

54. L. E. Gustafsson, A. M. Leone, M. G. Persson, *Biochem. Biophys. Res. Commun*., 1991, **181**, 852.

55. American Thoracic Society; European Respiratory Society ATS/ERS, 2005, *Am. J. Respir. Crit. Care Med*., **171**, 912.

56. P. E. Silkoff, P. A. McClean, A. Slutsky, *Am. J. Respir Crit. Care Med*., 1997, **155**, 260.

57. D. D. Nelson, J. H. Shorter, J. B. McManus *et al*., 2002, *Appl. Phys. B*, **75**, 343.

58. A. A. Kosterev, A. L. Malinovsky, F. K. Tittel *et al*., *Appl. Opt*., 2001, **40**, 5522.

59. G N Rao and A. Karpf, *Appl Opt*, 2010, **49**, 4906.

60. Z. Wang, C. Wang, *J Breath Res*, 2013, **7**, 037109.

61. E. R. Crosson, K. N. Ricci, B. A. Richman, *Anal Chem*., 2002, **74**, 2003.

62. http://www.picarro.com/products_solutions/isotope_analyzers/15n_18O_for_n2o.

63. A. M. Prakes, R. E. Lindley and A. J. Orr-Ewing, *Phys. Chem. Chem. Phys.*, 2004, **6**, 5313-5317.

64. A. M. Parkes, B. L. Fawcett and R. E. Austin *et al*., *Analyst*, 2003, **128**, 960.

65. M. Pradhan, R.E. Lindley, R. Grilli *et al*., *Appl. Phys. B,* 2008, **90**, 1.

66. B. L. Fawcett, A. M. Parkes, D. E. Shallcross *et al*., *Phys. Chem. Chem. Phys*., 2002, **4**, 5960.

67. S. S. Brown, H. Stark and A. R. Ravikrishankara, *Appl. Phys. B*., 2002, **75**, 173.

68. W. R. Simpson, *Rev. Sci. Instrum*., 2003, **74**, 3442.

69. R. Wada and A. J. Or-Ewing, *Analyst*, 2005, **130**, 1595.

70. S. M. Ball and R. L. Jones, *Chem. Rev*., 2003, 103, 5239.

71. M. Bitter, S. M. Ball, I. M. Povey *et al*., *Atmos. Chem. Phys*., 2005, **5**, 2574.

72. J. M. Langridge, S. M. Ball, R. L. Jones, *Analyst*, 2006, **131**, 916.

73. J. Morville, D. Romanini, A. A. Kachanov *et al*., *Appl. Phys. B*., 2004, **78**, 465.

74. T. J. A. Butler, J. M. Miller, A. J. Orr-Ewing, *J. Chem. Phys*., 2007, **126**, 174302.

75. M.L. Silva, D.M. Sonnenforh, D.I. Rosen *et al*., 2005, *Appl. Phys. B*., **81**, 705.

76. M. R. McCurdy, Y. Bakhirkin, G. Wysocki *et al*., 2007, *J. Biomed. Opt*., **12**, 034034:1.

77. J. H. Miller, Y. A. Bakhirkin, T. Ajtai *et al*., 2006, *Appl. Phys. B: Laser Opt*., 2006, 85, 391.

78. K. R. Parameswaran, D. I. Rosen, M. G. Allen, *Appl. Opt*., 2009, **48**, B73.

79. A. Maity, S. Som, C. Ghosh, *J. Anal. Atom. Spectrom*., 2014, **29**, 2251.

80. D. S. Bare, J. B. Paul, M. Gupta *et al*., *Appl. Phys. B*., 2002, **75**, 255.

81. J. Ye, L. S. Ma and J. L. Hall, *J. Opt. Soc. Am. B*., 1998, **15**, 6.

82. N. J. van Leeuwen and A. C. Wilson, *J. Opt. Soc. Am. B*., 2004, **21**, 1713.

83. A. Braithwaite and F. J. Smith, *Chromatographic Methods*, 1995 (Blackie Academia and Professional).

84. R. L. Grob and E. F. Barry, *Modern Practices of Gas Chromatography*, 2004 (Wiley).

85. A. C. Rivett, D. Martin, G. Nickless *et al*., *Atmos. Environ*, 2003, **37**, 2221.

86. J. R. Hopkins, A. C. Lewis and K. A. Read, *J. Environ. Monit*., 2003, **5**, 8.

87. P. G. Simmonds, S. O'Doherty, G. Nickless *et al*., *Anal. Chem*., 1995, 67, 717.

88. S. R. Sousa, S. E. Bialkowski, *Analytica. Chimica. Acta*., 2001, 433, 181.

89. J. Beauchamp and E. Zardin, *Odorant Detection by On-line Chemical Ionization Mass Spectrometry*, (Springer).

90. X. Ren, W. H. Burne, C. A. Cantrell *et al*., *J. Atoms. Chem*., 2005, **52**, 231.

91. E. Leibrock and L. G. Huey, *Geophys. Res. Lett*., 2000, **27**, 1719.

92. W. Lindinger, A. Jordon and A. Hansel, *Chem. Soc. Rev*., 1998, **27**, 247.

93. W. Lindinger, A. Hansel and A. Jordon, *J. Mass. Spectrom. Ion. Process,* 1998,173, 191.

94. A. Jordan, A. Hansel, R. Holzinger *et al*., *Anal. Chem., J. Mass Spect. Ion Proc*. 1995, **148**, L1.

95. A. Boschetti, F. Biasioli, M. Opbergen *et al*., *Postharvest Biol. Technol*., 1999, **17**, 143.

2 Cavity Ring-down Spectroscopy

Contents

2.1 Introduction

When a radiation of light passes through a sample, the light is absorbed by the sample and the intensity of the transmitted light is measured by a detector placed at the other end of the sample cell. If l is the length of the sample, I_0 and I are the intensities of input and transmitted radiation, respectively, then according to Beer-Lamberts law, the relation between I_0 and I is as follows:

$$\ln\left(\frac{I}{I_0}\right) = -\sigma[X]l \tag{2.1}$$

where [X] is the concentration of the sample and σ is the frequency dependent molecular absorption cross-section. Equation (2.1) can be re-written as

$$\ln\left(\frac{I_0}{I}\right) = \sigma[X]l = A \tag{2.2}$$

A is known as absorbance of the molecular species which is directly proportional to the concentration of the sample. By monitoring the frequency dependent absorption of the particular species, the absorption spectrum can be obtained. All the conventional absorption spectroscopy techniques that are discussed in the previous chapter are based on the Beer-Lamberts law. The traditional spectroscopy technique has few major limitations. The first drawback is the limited sensitivity which arises from the need to measure the small change in light intensity, i.e. $\delta I = \frac{I - I_0}{I_0}$, against a relatively large background level of transmitted light. Another drawback is the overlapping spectral features of different molecular species in a very narrow spectral window. This restricts the use of conventional spectroscopy in high resolution spectroscopy studies. To overcome the existing drawbacks of the traditional techniques, different alternative techniques have been proposed such as photo acoustic spectroscopy (PAS), laser induced fluorescence (LIF), and resonance enhanced multi-photon ionisation (REMPI) to improve the sensitivity of the measurements. On the other hand long path absorption techniques, modulation in wavelength or frequency also offer alternative strategies to enhance the sensitivity. However, the experimental complexity, difficulties in data extraction and measurement of the absolute concentration of the sample limit their use in many cases. Over the past two decades, there has been extensive research on optical resonator system which demonstrates the use of stable optical cavity, enhancing the sensitivity in the measurement procedure and can be comparable with sensitivities of LIF and REMPI methods. The substantial improvement in sensitivity is mainly due to multiple reflections of light within a high-finesse optical cavity comprised of two ultra -high reflectivity mirrors. The light is trapped inside the cavity for few tens of micro-seconds (μs) resulting the enhancement in absorbance. Thus the sensitivity improves few orders of magnitude over the conventional absorption techniques. In 1988[1], O'Keefe and Deacon first introduced such optical cavity-based absorption spectroscopy technique to measure a very weak absorption band of molecular oxygen and after their pioneering work, the technique so called cavity ring-down spectroscopy (CRDS) has found very popular. It is a high sensitive, laser based direct absorption measurement technique which has a wide range of applications in molecular spectroscopy[2-7] and kinetics studies[8,9]. CRDS has also been used to study the chemistry of liquids[10], thin-flims[11], surfaces[12] and solids[13]. The technique can also be applied to probe the species in harsh environment such as in plasma torches[14], flames[15,16], discharges[17] and in supersonic molecular beam[18]. The research area in which the application of CRDS has proven particularly valuable is that ultra-sensitive trace gas sensing in biomedical science[19,20] and atmospheric chemistry[21,22]. The development of the CRDS sensor using the continuous wave (*cw*) laser operating in the mid-IR (MIR) or near-IR (NIR) spectral region offers the possibility of developing compact, lightweight and high sensitive sensor for monitoring the trace species in exhaled human breath and atmospheric samples. The principal advantages of the CRDS technique over the high sensitive LIF and REMPI methods are as follows:

- The CRDS technique is insensitive to shot-to-shot power fluctuation of the incident laser beam because the measurement is done in time domain.
- In CRDS experiment, the light inside the cavity traverses a long effective absorption path length by means of multiple reflections. Thus enhancing the sensitivity of the technique.
- The technique offers the sensitivity upto 10^{-8} to 10^{-10} cm^{-1}. This in turns demonstrates the direct, high resolution temporal and spatial measurement of absorption of the trace species from parts per billion by volume (ppbv) down to parts per trillion by volume (pptv) levels.
- Since CRDS is a direct absorption measurement technique, it does not require calibration with secondary standard gas.
- It is a general technique for detection of gas phase atoms, molecules and radicals.

In this chapter we will discuss about the basic principle of operation and practical design of ring down cavity (RDC) with fundamentals of sensitivity limits of the *cw*-CRDS apparatus used in this thesis. Finally we discuss about the “Allan Variance” analysis which demonstrates the stability of the optical cavity.

2.2 Principle of CRDS operation

The basic principal of operation of cavity ring-down spectroscopy is depicted in figure 2.1. In this technique, the laser light is injected along the central axis of a high finesse optical cavity comprised of two high reflectivity mirrors with reflectivity (R)>99.98%. The optical cavity is used as the sample cell in the ring-down experiment.

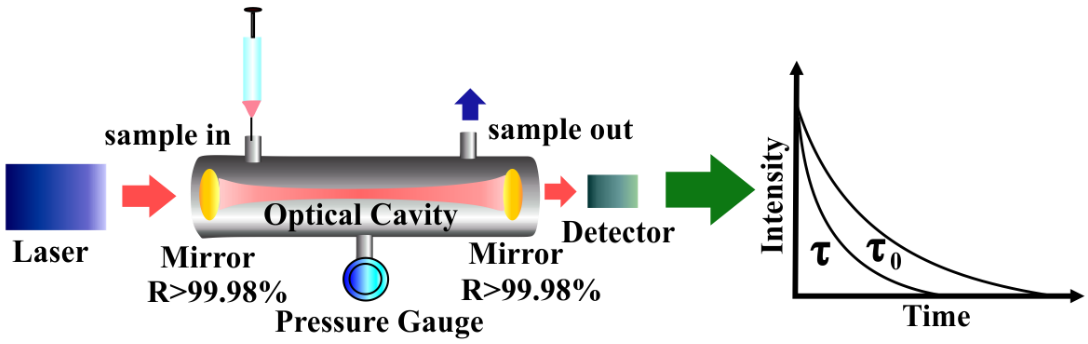

Figure 2.1 *Shows the principle of cavity ring-down spectroscopy technique*

A fraction of laser light that is successfully coupled into the cavity suffers back and forth reflections inside the optical cavity with a tiny amount of laser light being transmitted through the mirrors upon each reflection. The transmission through one of the mirrors is measured by a fast-response photo-detector which measures the decay of light intensity with time and can be described as follows:

In absence of any absorber or any loss mechanism present, the time dependence of the exponential decay of light intensity from an optical cavity can be expressed by equation[23]

$$\begin{aligned} I(t) &= I_0\, e^{\left[-\frac{c(1-R)}{l}t\right]} \\ &= I_0\, e^{\left(-\frac{t}{\tau_0}\right)} \end{aligned} \tag{2.1}$$

Where $\tau_0 = \dfrac{l}{c\,(1-R)}$ (2.2)

here l is the length of the cavity, R is the reflectivity of the mirror and c is the speed of the light. Here τ_0 is the time required for the intensity exiting from the cavity to decay 1/e times of the initial light intensity is called the empty cavity ring-down time (RDT). The reciprocal of RDT is defined as decay rate (k_0) follows the relation

$$k_0 = \frac{1}{\tau_0} \tag{2.3}$$

As an example, an optical cavity of length 50 cm comprised of two high reflectivity mirrors with R=0.9999, exhibits the empty cavity ring-down time τ_0=16.67 μs and the light trapped inside the cavity traverses an effective optical pathlength ~5 km in this time.

In presence of an absorber inside the optical cavity, the decay become faster and in accordance with Beer-Lambert law output intensity exiting from the cavity can be expressed as[36]

$$\begin{aligned} I(t) &= I_0\, e^{\left[-\frac{c\,(1-R)}{l}t+(\alpha d)\bullet\left(\frac{tc}{l}\right)\right]} \\ &= I_0 e^{\left(-\frac{t}{\tau}\right)} \end{aligned} \tag{2.4}$$

where $\tau = \dfrac{l}{\left[c\,(1-R)+\alpha d\right]}$ (2.5)

Here *d* is the length of the sample inside the cavity, α is the absorption coefficient of the sample. α is directly proportional to the concentration ([X]) of the sample and the relation is as follows:

$$\alpha = \sigma[X] \tag{2.6}$$

where σ is the wavelength dependent absorption cross-section. All the CRDS experiments performed in this thesis are based on $d = l$ which implies the sample fills the whole RDC. From equation (2.3) and (2.5) it can be stated that RDT depends on the length of the cavity and reflectivity of the mirror thus it is independent on laser intensity fluctuation

During the experiment, τ and τ_0 are recorded as a function of laser frequency and absorption spectrum of the sample is obtained by tuning the laser frequency into resonance with the absorption feature of the gas sample. Using equation (2.2) and (2.5) α can be evaluated as follows:

$$\alpha = \frac{\Delta k}{c} \tag{2.7}$$

where $\Delta k = k - k_0 = \dfrac{1}{\tau} - \dfrac{1}{\tau_0}$, the change in ring-down decay rate coefficient in presence of the sample inside the cavity. A plot of Δk against the wavelength of the laser (or wavenumber) gives the absorption spectrum of the sample. If the absorption cross-section of the particular molecular species is known at a particular wavelength, then the concentration of the sample can be estimated easily by measuring the changes in the RDT or ring-down decay rate in presence and absence of the sample. Therefore in the CRDS experiment the direct and quantitative determination of concentration of the sample is possible without need for secondary calibration.

2.3 Sensitivity of CRDS experiment

CRDS is a highly sensitive technique and the limiting sensitivity of the cavity ring-down spectrometer can be defined as the minimum value of the absorption coefficient, α_{min} that can be measured by the spectrometer. This can be determined from the equation (2.7):

$$\alpha = \frac{\Delta k}{c} = \frac{1/\tau - 1/\tau_0}{c} = \frac{\tau_0 - \tau}{c\tau_0\tau} \tag{2.8}$$

In the low absorption regime, $\tau \rightarrow \tau_0$ and therefore equation (2.9) can be used to determine the limiting sensitivity of the spectrometer

$$\alpha_{\min} = \frac{\Delta\tau_{\min}}{c\tau_0^{\,2}} = \frac{1}{c\tau_0}\left(\frac{\Delta\tau_{\min}}{\tau_0}\right) \tag{2.9}$$

where $\Delta\tau_{min}$ is the minimum detectable change in the cavity ring-down time and $\left(\frac{\Delta\tau_{\min}}{\tau_0}\right)$ corresponds to the relative error in ring-down time (τ) measurement. In practice, a large number ($\geq$ 100) of ring-down measurements are used to determine the value of $\left(\frac{\Delta\tau_{\min}}{\tau_0}\right)$. The sensitivity of the spectrometer can be improved in two ways, either by increasing the reflectivity of the mirror or by increasing the cavity length. Moreover, good mechanical stability of the cavity and reduction of the noise in the electrical signal ensure the minimisation of $\left(\frac{\Delta\tau_{\min}}{\tau_0}\right)$ value which further improves the sensitivity of the spectrometer. In CRDS experiment, when scanning across the absorption line of a molecular species, a typical limiting sensitivity α_{min} ~ 10^{-8}-10^{-9} cm^{-1} can be achieved and the minimum detection limit for the particular molecular species can be obtained directly by dividing the α_{min} value by the wavelength dependent peak absorption cross-section. Thus the minimum detection limit for a particular analyte in CRD experiment can be expressed as

$$[X]_{\min} = \frac{\alpha_{\min}}{\sigma_{\lambda}} \tag{2.10}$$

The sensitivity of the spectrometer can often be stated in terms of detection limit. This is defined as the minimum concentration that can be detected by a spectrometer and can be presented by the equation (2.11)

$$[X]_{\min} = \frac{1}{c\tau_0\sigma}\frac{\Delta\tau}{\tau_0} \tag{2.11}$$

Thus larger is the absorption cross-section, lower is the detection limit of the spectrometer for the detection of the particular molecular species. The detection limit can also be expressed as in terms of a mixing ratio i.e.in ppbv (parts per billion by volume) in pptv (parts per billion by volume) at 1 atmosphere pressure of air. In that case the air broadening coefficient has to be taken into account to estimate the minimum detection limit of the sample.

As an alternative to the detection limit of the spectrometer, the sensitivity of the spectrometer can also be stated in terms of noise-equivalent absorption (NEA) coefficient and can be expressed as[24]

$$NEA = \left(\frac{2}{f_{rep}}\right)^{1/2}\alpha_{\min} \tag{2.12}$$

where f_{rep} is the data collection rate in unit of Hz. NEA indicates the smallest absorption coefficient that can be distinguished from empty cavity losses during a 1-s measurement interval, with a 1σ certainty, provided that the data collection rate (f_{rep}) is large enough to determine adequately the relative standard deviation $\left(\frac{\Delta\tau_{\min}}{\tau_0}\right)$. The values of NEA in CRDS experiments typically vary between 10^{-8}-10^{-11} cm^{-1}Hz$^{-1/2}$ [23,24].

2.4 Cavity modes

In the previous section 2.1 it was assumed that the laser light coupled to the optical cavity without considering the length of the cavity and frequency of the laser. But in actual experimental condition, the cavity length and the frequency of the laser have to be taken into account for generation of stable cavity modes. The high-finesse optical cavity behaves like a Fabrey-Perot etalon and only the selected modes are transmitted. The back and forth reflection of light inside the cavity results in the formation of the standing wave patterns inside the cavity, when the mirror separation is about multiple integer of half wavelength of the injected light or alternatively, twice of the separation of the cavity mirrors divided by the wavelength of the laser must be an integer for a certain length of the cavity. The frequencies of the radiation that satisfy the wavelength requirements are determined by the longitudinal mode structure of the cavity. The frequency spacing between two consecutive longitudinal modes is described as free spectral range (FSR) of the cavity and denoted by the following equation:

$$\Delta\nu_{FSR} = \frac{c}{2l} \tag{2.13}$$

The free spectral range also depends on the round-trip time of the light inside the optical cavity. For a cavity of length 50 cm the FSR will be 300 MHz.

The finesse of the optical cavity attributes to the resolving power of the cavity. The finesse of the optical cavity is dependent on the reflectivity of the mirror and can be expressed as

$$F = \frac{\pi\sqrt{R}}{1-R} \tag{2.14}$$

However, the longitudinal modes can be described by Lorentzian line shape function whose FWHM decreases with increase in reflectivity of the mirror. The full width at the half maximum of the cavity modes can also be quoted in terms of finesse of the optical cavity as follows:

$$\Delta\nu_{1/2} = \frac{\Delta\nu_{FSR}}{F} \tag{2.15}$$

Therefore, the cavity modes become sharper with increase in finesse of the optical cavity. For example, a cavity of length 30 cm consists of two high reflectivity mirrors of R=0.9999, exhibits the optical finesses of ~31400 and $\Delta\nu_{1/2} = 9.55$ KHz.

So far we have discussed about the formation of the cavity mode excluding the geometric configuration of the cavity. The design of the optical cavity plays a significant role for good stability of the optical cavity which reduces diffraction losses and more importantly diminishes beam walk-off or divergence loss. To confine the laser beam within the optical cavity for a CRDS measurement, the cavity must be optically stable. As a result, the stable cavity provides longer effective pathlength which in turn enhances the sensitivity for measurement of ultra-low concentration. A laser beam propagating along the central axis of the optical cavity has the Gaussinan intensity profile[25] with amplitude distribution of the beam is shown in equation (2.16)

$$\Psi(x,y) = \Psi_0 \sqrt{\frac{2}{\pi}} \frac{w_0 \exp\{-i[\Phi_0 - \Phi(z)]\}}{w(z)} \exp\left[-i\frac{kx^2}{2R(z)} - \frac{x^2}{w^2(z)}\right] \tag{2.16}$$

The function *w(z)* gives the evaluation of the Gaussian beam inside the optical cavity, *R(z)* is the radius of curvature of the wave front and $\phi(z)$ is related to the phase of the beam. *k* is the wavenumber which is equal to $\frac{2\pi}{\lambda}$, where λ is the wavelength of the wave propagating through the cavity. Since the laser beam traverses back and forth reflection along the central axis inside the symmetric cylindrical optical cavity only the zeroth oreder transverse modes are TEM_{00} modes are excited and described by equation (2.16). The Gaussian beam propagating along z axis through the optical cavity, the wave front curvature of the Gaussian beam must match with the curvature of the mirrors which formed the optical cavity as shown in figure 2.2. The Gaussian beam will have the specific beam waist (w_0), defined as the distance from the centre to the point where the intensity of the become 1/e times of its maximum value. The waist diameter $2w_0$ is called the spot size of the beam inside the cavity.

However, the beam radius is minimum at the reference plane z = 0 i.e. at the beam waist and varies along the propagation direction z according to equation (2.17) as described below.

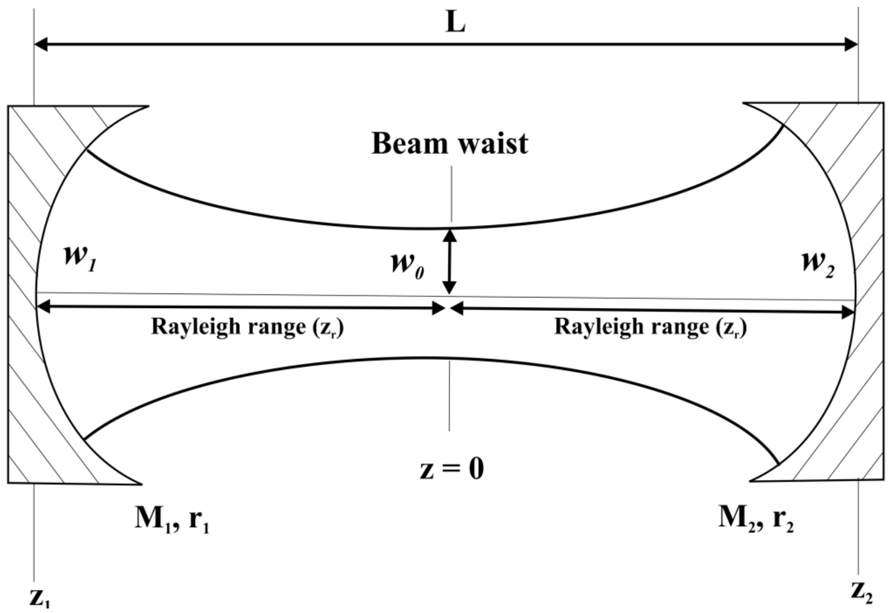

Figure 2.2 *Schematic diagram of a Gaussian beam through a two-mirror optical resonator*

$$w(z) = w_0 \sqrt{1 + \left(\frac{z}{z_R}\right)} \qquad (2.17)$$

where z_R is known as Rayleigh range which is an important parameter to characterise the propagation of the Gaussian beam in a stable optical cavity. The Rayleigh range[26] may be defined as the distance from the beam waist that the Gaussian beam travels before the diameter increases by √2 and the beam area doubles, as described by in equation (2.17).

$$z_R = \frac{\pi w_0^{\ 2}}{\lambda} \qquad (2.18)$$

The Rayleigh range also indicates the length over which the beam can propagate without significant divergence. Close to the beam waist, the Gaussian beam is almost parallel with a cross-section equal to that beam waist. Moreover, in the far field ($z >> z_R$) the beam radius increases approximately linearly along the z axis with an angular divergence θ as described in equation[26] (2.19) and shown in figure 2.3

$$\theta \cong \frac{\lambda}{\pi w_0} \qquad (2.19)$$

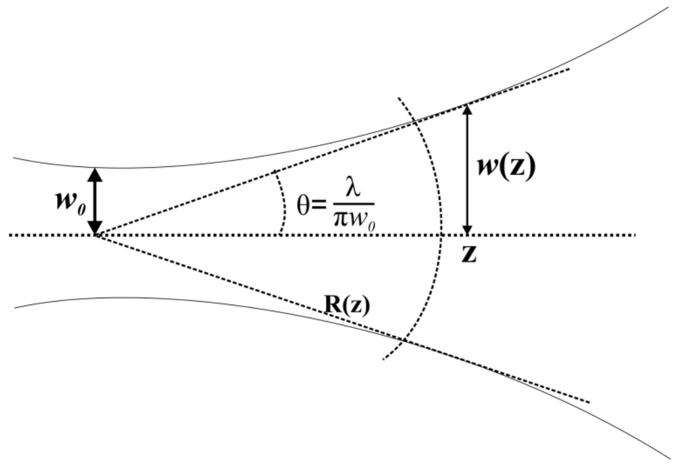

Figure 2.3 *Schematic diagram of a Gaussian beam intensity propagating along z axis*

For example, a Gaussian TEM_{00} beam passing through the cavity having the beam waist of ~ 0.07 mm and wavelength λ ~5200 nm, the beam divergence half angle will be ~2.5 mrad which is very shallow. From equation (2.19) it is obvious that higher is the beam diameter smaller is the divergence and vice-versa. Furthermore, in w_1 and w_2 are the beam radii, defined as the distances from the centre at which the intensity falls to $1/e^2$ of its peak value on the two end mirrors as shown in figure 2.2.

The Rayleigh range of the trapped Gaussian beam can be expressed in terms of "resonator g parameters", g_1 and g_2, and is given by[25]

$$z_R = \frac{g_1 g_2 (1 - g_1 g_2)}{(g_1 + g_2 - 2 g_1 g_2)} L^2 \tag{2.20}$$

where, $g_1 = 1 - \frac{L}{r_1}$ and $g_2 = 1 - \frac{L}{r_2}$, r_1 and r_2 are the radius of curvature of the two mirror M_1 and M_2 as shown in figure 2.2.

During the design of the cavity of small volume, it is useful to know the position of the mirrors relative to the beam waist and also the beam waist at the centre and the two end mirrors to avoid the diffraction losses arises from the edges of the mirrors and also the spot size of the laser beam at each mirror should be less than radius of the mirror. The relative positions of the mirrors, the beam parameters such as beam waist, beam radii w_1 and w_2 at the end mirrors are given by the following equations:

$$z_1 = \frac{g_2(1-g_1)}{(g_1+g_2-2g_1g_2)}L \text{ and } z_2 = \frac{g_1(1-g_2)}{(g_1+g_2-2g_1g_2)}L \tag{2.21}$$

$$w_0^{\ 2} = \frac{L\lambda}{\pi}\sqrt{\frac{g_1g_2(1-g_1g_2)}{(g_1+g_2-g_1g_2)^2}} \tag{2.22}$$

$$w_1^{\ 2} = \frac{L\lambda}{\pi}\sqrt{\frac{g_2}{g_1(1-g_1g_2)}} \text{ and } w_2^{\ 2} = \frac{L\lambda}{\pi}\sqrt{\frac{g_1}{g_2(1-g_1g_2)}} \tag{2.23}$$

From these equations, it is clear that real and finite solutions for the Gaussian beam parameters can only possible if the stability parameters g_1 and g_2 satisfy the relation as described in equation (2.24)

$$0 \le g_1g_2 \le 1 \tag{2.24}$$

Figure 2.4 shows the stability diagram for a two-mirror optical resonator, plotted as g_1 against g_2. The shaded region on the stability diagram contains all two-mirror resonators that will support a Gaussian beam and leads to stable periodic focusing of the laser beam. But if the two-mirror optical resonator lies outside the shaded region, then it will not support the Gaussian beam and leads to unstable periodic focusing.

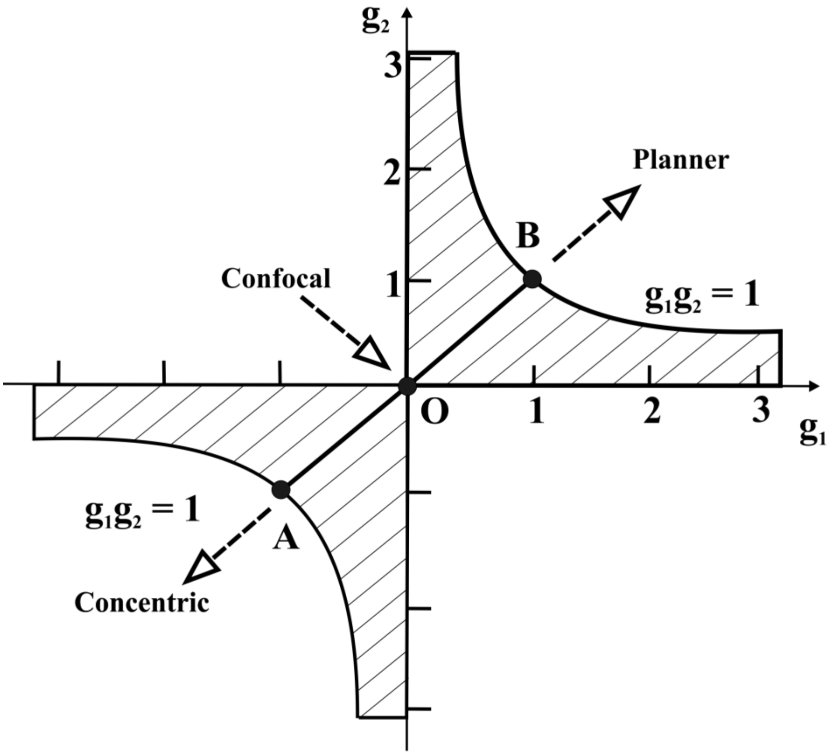

Figure 2.4 *A stability diagram for a two mirror optical resonator system*

However, in CRDS experiments two identical mirrors ($R_1 = R_2 = R$ and $r_1 = r_2 = r$) are used and the geometry of the cavity can be described by a point on the line that connect the points A, O and B with a straight line of slope 45^0 angle with respect to the either axes of the graph. The points A, O and B demonstrate the three different cavity geometries. At point A, $g_1 = g_2 \approx -1$ and $R_1 = R_2 = L/2$ which indicate the concentric configuration of the optical cavity with large spot size on each of the mirrors with small beam waist. These types of cavities are not suitable in CRDS experiment. At point B, $g_1 = g_2 \approx 1$and $R_1 = R_2 = \infty$ which indicate the planar configuration of the optical cavity with large spot size on each of the mirrors and large beam waist. This type of configuration is also not suitable for CRDS experiments. Furthermore, both A and B lie on the limits of cavity stability restricted the use of concentric and planner cavity in the experiments with stable optical resonators. At point O, $g_1 = g_2 \approx 0$ and $R_1 = R_2 = L$ which indicate the confocal configuration of the cavity that lies in the central point of the stability diagram. It provides the smallest beam waist with a value at the centre of the cavity:

$$w_0 = \sqrt{\frac{\lambda L}{2\pi}} \tag{2.25}$$

and at the mirrors,

$$w_1 = w_2 = \sqrt{2}\, w_0 \tag{2.26}$$

In symmetric confocal configuration, the two mirrors focus the beam to the centre of the resonator and the mirrors are separated by Rayleigh range which diminishes the diffraction losses and the cavity become extremely stable. It is therefore, insensitive to slight misalignment of either mirror. The CRDS experiments presented in this thesis were carried out using cavity geometries located at the middle point of O and B with g ~ 0.5.

The frequency of the stable cavity modes can be described by the g parameters of the optical cavity as shown in equation[25,27] (2.27)

$$\nu = \frac{c}{2l}\left[n + (n+m+l)\frac{\cos^{-1}\sqrt{g_1 g_2}}{\pi} \right] \tag{2.27}$$

where n, *l*, m are the integers used to index the modes, n is used to describe the longitudinal mode, and *l* and m are used to describe the transverse mode structure. For the lowest order transverse mode *l*= m = 0 and the mode is termed as TEM_{00} mode. The TEM_{00} mode is only excited if the light is injected into the cavity along its central axis. *l* and m greater than 1 corresponds to higher order transverse mode and those mode will be generated if light enters slightly off-axis into the cavity. These higher order modes associated with different cavity losses because of unevenness of the mirror coatings or different diffraction losses. As a result, the cavity ring-down time may be different with large variation in ring-down decay rate for measurement of fixed concentration and hence an artificially large $\left(\frac{\Delta\tau}{\tau}\right)$value.

2.5 Mode matching

As described in preceding section, the optimum performance of a CRD spectrometer can be achieved by proper design and careful alignment of the optical cavity. If the cavity is poorly designed, the FSR of the cavity might exceed the width of the absorption spectrum to be studied. In that case, the light frequency corresponds to the absorption feature of interest may not be injected into the cavity and this feature will be absent from the resultant absorption spectrum[28]. Similarly, the laser bandwidth is also an essential parameter for trapping of laser light into the cavity. If the bandwidth of the laser is narrower than the FSR, the light will not be coupled into the cavity at all laser frequency as shown in figure 2.5.

In pulsed CRDS experiment, the bandwidth of the laser is typically in order of 500 MHz or more and using of cavity length of ~1 m ensure that mode spacing (FSR~150 MHz) is smaller than the bandwidth of the laser and hence the light can be coupled very easily into the optical cavity[29]. However, in *cw* CRDS experiment, the bandwidth of the laser (e.g. diode lasers have the bandwidth ~ 2 MHz) is significantly narrower than the FSR. Therefore an extra arrangement is required to ensure overlap of the laser and cavity mode frequencies. This can be done in several ways during the absorption measurement. Engeln *et al.*[30] demonstrated the changed in the cavity length by mechanical vibrations result the accidental coincidences of the cavity mode

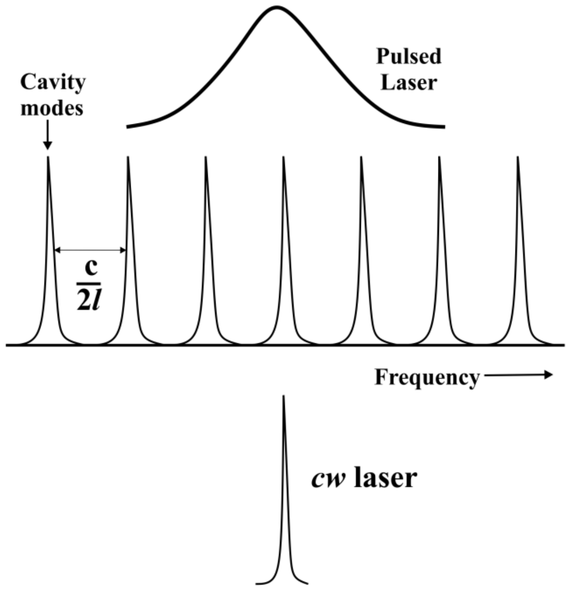

Figure 2.5 *A schematic diagram of linewidth of pulsed and cw lasers with cavity mode spacing*

with laser frequency. Whereas Romanini *et al.*[31] reported the active modulation of cavity length in a more uniform way using a pizeo-electric transducer attached to one of the cavity mirror mount. Figure 2.6 shows the cavity transmission as a triangular signal is applied to a PZT mirror mount to sweep the cavity length over one FSR of the cavity.

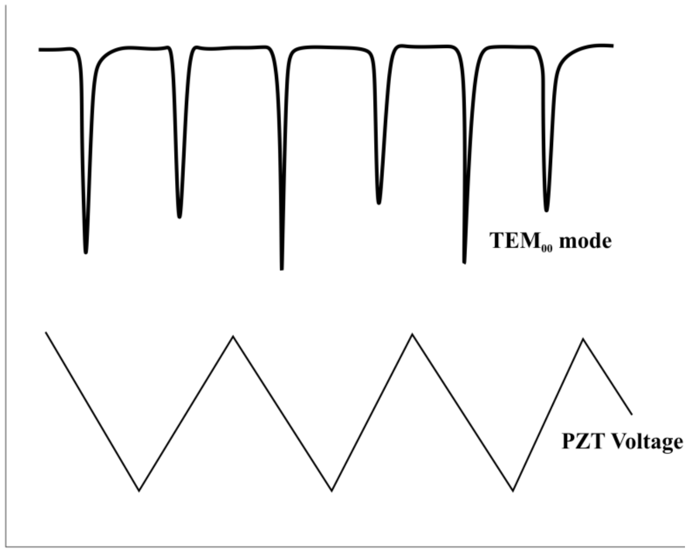

Figure 2.6 Top: *Inverted TEM_{00} mode intensity measured from the output of a scanning cavity*. Bottom: *The triangular voltage applied to the PZT for scanning of the cavity over one FSR*

At certain voltages, or the cavity lengths, the cavity mode comes into resonance with the laser frequency and the light is coupled into the cavity, as shown by spikes in the output intensity. In both of the described method cavity length is modulated so that the cavity mode structure comes into resonance regardless of the laser frequency. In this case, spectral resolution is limited by the bandwidth of the laser. Alternatively, the laser frequency can be modulated to ensure overlap with a particular longitudinal cavity mode[32]. In this case the resolution is limited by the FSR of the cavity and the technique is suitable for measurement of broadband absorber.

2.6 Continuous wave cavity ring-down spectroscopy (cw-CRDS)

Once the light is successfully coupled into the optical cavity, the light has to be switched off to allow the intracavity light to decay in intensity and the ring-down decay to be observed. The decay will follow a first order exponential decay if the cavity is well aligned, with the laser both frequency and spatially matched to one transverse mode. In pulsed CRDS measurement, the off-period between the pulses allows the intracavity light to decay and no further light can be injected into the cavity. But in *cw*-CRDS, a fast optical switch such as an acousto optic modulator (AOM) connected with a trigger circuit is used to initiate the decay of light. When the light intensity in the cavity reaches a pre-selected threshold level on a trigger generator, a trigger is sent to the AOM to switch off the light, allowing intracavity light to decay. This is depicted in figure 2.7. Though there are many complexities associated with *cw*-CRDS technique, several advantageous features made this approach very popular for trace gas analysis, when compared with pulsed CRDS technique. As stated earlier, narrow bandwidth of the cw-laser enables to record the spectra at higher resolution. This can also help to enhance the sensitivity of the technique as the laser can be tuned to the wavelength of the maximum absorption in spectral features and the resulting spectra are not the convolution of instrumental bandwidth function. The bandwidth of the pulsed laser being comparable with the linewidth of the absorption spectral features, leads to multi-exponential decay in ring-down signal which in turn provide the inaccurate measurement of absorption of the targeted molecular species[33]. The problem can be resolved easily by using a *cw*-laser as a light source. Furthermore, in *cw*-CRDS the light intensity or the energy is build-up inside the cavity as the cavity mode is in resonance with the laser frequency which is primarily done by length modulation of the cavity.[34]

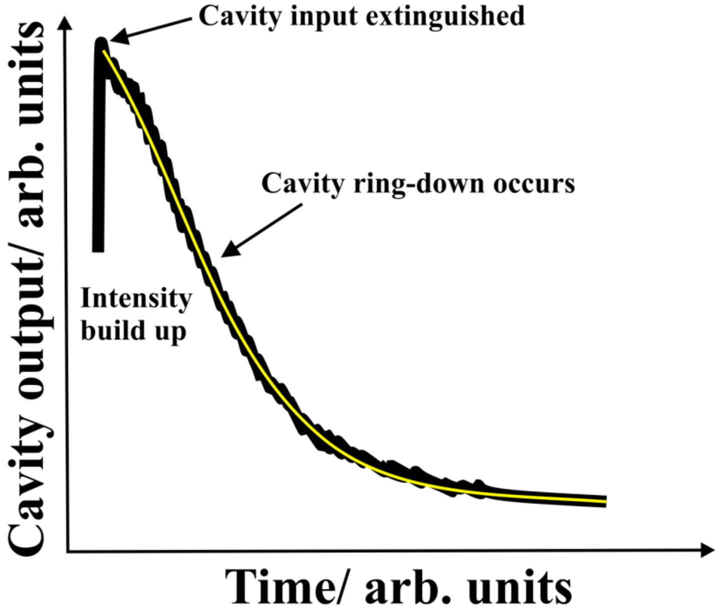

Figure 2.7 *A CRD trace shows the build-up of intra cavity light intensity. At the threshold voltage AOM extinguishes the laser light and the intra cavity light decays exponentially with time.*

Thus more slowly scanning of the cavity, greater the build of light intensity occurs. As a result the detector receives higher light intensities and subsequently improvement in signal to noise ratio is observed. The use of *cw* diode laser is beneficial because of low cost, compactness, low power consumption, user friendly and cryogen free cooling operation, suggest the potential for use in field instruments stationed at remote location for analysis of trace molecular species[35].

The potential drawback of the diode lasers is the narrow tuning. The distributed feedback (DFB) lasers operate over a tuning range of 2-4 nm. The external cavity diode laser (ECDL) operates over a tuning range of 50 nm which restricted their use for monitoring the trace molecular species in exhaled human breath or in atmospheric samples. Now-a-days, the use of *cw* external-cavity quantum cascade laser (cw-EC-QCL) removes the barriers. It offers wide tunibility with mode-hop-free tuning feature, extremely narrow linewidth, cryogen free cooling, and room temperature operation. Thus it becomes very popular and widely used in trace gas sensing as well as in fundamental molecular spectroscopic studies. In the present thesis work, we have investigated the performance of an EC-QCL based cavity ring-down spectrometer for ultrasensitive detection of trace molecular species in exhaled human breath and atmospheric sample and subsequently utilized the spectrometer for high-resolution fundamental molecular spectroscopy studies.

2.7 Allan variance analysis

Allan Variance analysis is a traditional method to determine the optimum integration time period for a particular resonator system. It is named after David W. Allan and utilized to determine the stability of the optical cavity. The improvement in detection limit for any spectroscopic system depends on the stability of that specific system. Thus longer is the stability of the system, higher is optimum integration time which in turn maximizes the signal to noise ratio for that particular system[36]. In the present thesis, the Allan variance analysis was performed to characterize the overall stability of the developed mid-IR EC-QCL based CRDS system and has been discussed in section 3.2.3 in details. The Allan variance is evaluated using the equation (2.28), where A_1 and A_2 are the averages of adjacent time series of data.

$$\sigma_A{}^2 = \frac{1}{2}\left(A_2 - A_1\right)^2 \tag{2.28}$$

An Allan plot is a log-log plot of $\sigma_A{}^2$ against the number of data points averaged to calculate A_1 and A_2. From the plot, the optimal integration time of the CRDS system can be estimated. As the integration period increased, the Allan variance should decrease so long as increased signal averaging leads to a reduction in the noise level. The sensitivity of the system usually increase with more signal averaging and enhancement in sensitivity occurs until some long term instabilities such as drift in alignment, laser power come into effect and cause the Allan variance to either remain constant or increase. Thus the longer averaging of the ring-down decay signals beyond such long-term instabilities would not provide a better precession for the measurement of the targeted absorption spectral line.

The Allan-variance can be written as summation of different noise sources which are encountered in most CRDS system:

$$\sigma_A{}^2(\xi) = c_{whitenoise}(1/\xi) + c_{1/f} + \sum_a c_{drift,\alpha}\, \xi^{\alpha} \tag{2.29}$$

where ξ is the integration time. The noise contributions come from frequency independent random transient fluctuations known as white noise and frequency dependent *1/f* and $1/f^{\alpha}$ (α>1) noise. The 1/*f* noise is also called flicker or pink noise and $1/f^{\alpha}$ noise is dominate in low frequencies and related to the drifting of the system, whereas the intermediate *1/f* noise exhibits a balance between random ness and correlation at all time scale. In CRDS experiment, the primary contribution of different noises in time domain is shown in Table 2.1

Table 2.1 *Allan variance as a function of integration time ξ for different spectral noise density*

Noise Type	Spectral noise density [S(f)]	Allan variance (σ_A^2)
White	f^0	$\infty\ \xi^{-1}$
1/*f*	f^1	constant
Drift	f^2	$\infty\ \xi$
Drift (Linear)	f^3	$\infty\ \xi^2$

To determine the stability of the CRDS system, the Allan variance analysis may be performed on different parameters such as ring-down decay signal, output laser intensity, the laser temperature or the current and the estimated concentration values from the calibrated setup. There are three major sections of the plot. At the initial part, the Allan variance decreases with increasing integration time, suggesting increasing signal averaging leads to the reduction in noise level and the gradient of the line best fitted to -1which corresponds to a white noise source. In the second part the Allan variance remains constant and governed by 1/f noise. Finally, Allan variance increases with increase in integration time and shifted from 1/f noise to drift dominated region and the gradient of the line best fitted to 1. The drifting may be due to mechanical vibration that results the change in optical alignment, change in laser temperature/ current etc[37].

2.8 Conclusions

In this chapter, we have demonstrated the basic operation principle of cw-CRDS system and discussed about the sensitivity of the spectrometer for analysis of trace molecular species. We have also discussed about the different stability parameters that should be taken into account to construct a stable optical resonator system which in turn improve the sensitivity of the system and hence the detection limit. Furthermore, we demonstrated the advantageous features of the cw-CRDS technique over the pulsed CRDS systems and discussed about the Allan variance analysis to describe the stability of the *cw*-CRDS system. In this thesis, we have demonstrated the advantages of a *cw*-EC-QCL based high resolution cavity ring down spectrometer in trace gas sensing as well as in high resolution molecular spectroscopy experiments that have been described in the subsequent chapters in detail.

2.9 References

1. A. O'Keefe and D. A. G. Deacon, *Rev. Sci. Instrum.*, 1988, **59**, 2544.

2. M. D. Wheeler, A. J. Orr-Ewing and M. N. R. Ashfold, *J. Chem. Phys.*, 1997, **107**, 7591.

3. M. D. Wheeler, S. M. Newman and A. J. Orr-Ewing, *J. Chem. Phys.*, 1998, **108**, 6594.

4. W. H. Howie, I. C. Lane and S. M. Newman *et al.*, *Phys. Chem. Chem. Phys.*, 1999, 3079.

5. W. H. Howie, I. C. Lane and A. J. Orr-Ewing, *J. Chem. Phys.*, 2000, **113**, 7237.

6. A. Teslja, B. Nizamov and P. J. Dagdigian, *J. Phys. Chem. A.*, 2004, **108**, 4433.

7. S. J. Greaves, E. L. Flynn, E. L. Futcher *et al.*, *J. Phys. Chem. A.*, 2006, **110**, 2114.

8. D. B. Atkinson, J. W. Hudgens, A. J. Orr-Ewing, *J. Chem. Phys.*, 1999, **103**, 6173.

9. A. J. Hallock, E. S. F. Berman, R. N. Zare, *J. Am. Chem. Soc.*, 2003, **125**, 1158.

10. S. Xu, C. Sha and J. Xie, *Rev. Sci. Instrum*, 2002, **73**, 255.

11. R. Engeln, G. Helden, A. J. A. Roij, *J. Chem. Phys.*, 1999, **110**, 2732.

12. A. C. Pipino, J. W. Hudgen and R. E. Huie, *Rev. Sci. Instrum.*, 1997, 68, 2978.

13. R. Engeln, G. Berden, E. van den Berg *et al.*, *J. Chem. Phys*, 1997, **107**, 4458.

14. G. P. Miller and C. B. Winstead, *J Anal, Atom. Spectrosc*, 1997, **12**, 907.

15. G. Meijer, M. G. H. Boogarts, R. T. Jongma *et al.*, Chem. Phys. Lett., 1995, **217**, 112.

16. J. J. Scherer, K. W. Aniolke, N. P. Cernansky et al., *J. Chem. Phys.*, 1997, **107**, 6196.

17. D. Romaninin, L. Biennier, F. Salama *et al.*, *Chem. Phys. Lett.*, 1999, **303**, 165.

18. J. B. Paul, C. P. Collier, R. J. Saykally *et al.*, *J. Chem. Phys.*,1995, **102**, 5190.

19. M. R. Mccurdy, Y. A. Bakhirkin and F.K. Tittel, *Appl. Phys. B*, 2006, **85**, 445.

20. Y. A. Bakhirkin, A. A. Kosterev and C. Roller, *Appl. Opt.*, 2004, **43**, 2257.

21. B. L. Fawcett, A. M. Parkes, D. E. Shallcross *et al*., *Phys. Chem. Chem. Phys*., 2003, **128**, 960.

22. A. M. Parkes, R. E. Lindley and A. J. Orr-Ewing, *Anal. Chem*., 2004, **76**, 7329

23. M. I. Mazurenka, A. J. Orr-Ewing, R. Peverall, *Ann. Rep. C*., 2005, **101**, 100.

24. R. D. Van Zee, J. T. Hodges and J. P. Looney, *Appl. Opt*., 1999, **38**, 3951.

25. A. E. Siegman, *Lasers*, 1986 (Oxford University Press).

26. A. J. Orr-Ewing, *Optics and Optical cavities*, 2003 (Lecture notes, University of Bristol).

27. H. Kogelnik and T. Li, *Proc. IEEE*, 1966, **54**, 1312.

28. K. K. Lehmann and D. Romanini, *J. Chem. Phys.*,1996, **105**, 10263.

29. R. E. Lindley, *Development of diode laser based optical sensors for quantitative trace gas analysis*, PhD Thesis, University of Bristol, 2007.

30. R. Engeln, G. Helden, G. Berden *et al*., *Chem. Phys. Lett*., 1996, **262**, 105.

31. D. Romanini, A. A. Kachanov and F. Stoeckel, *Chem. Phys. Lett*., 1997, **270**, 538.

32. A. M. Parkes, B. L. Fawcett, R. E. Austin *et al*., *Analyst*, 2003, **128**, 960.

33. P. Zaliki and R. N. Zare, J. Chem. Phys, 1995, **102**, 2708.

34. A. M. Parkes, *Trace detection of atmospheric gas sensing using cavity enhanced spectroscopy*, PhD Thesis, University of Bristol, 2004.

35. G. Berden, R. Peeters and G. Meijer, *Int. Rev. Phys. Chem*., 2000, **19**, 565.

36. P. Werle, R. Mucke and F. Slemr, *Appl. Phys. B*., 1993, **57**, 131.

37. M. Pradhan, *Development of diode –laser based optical sensor for continuous monitoring of trace gases in the atmosphere*, PhD Thesis, University of Bristol, 2008.

3 Development of a quantum cascade laser based cavity ring-down spectrometer for ultra-sensitive detection of nitrous oxide at 5.2 μm

Contents

3.1 Introduction

Nitrous oxide (N_2O) is one of the most important atmospheric greenhouse gases, contributing to global warming as well as climate change. The global warming potential (GWP) of N_2O is about 300 times greater than carbon dioxide (CO_2) over a 100 year time horizon[1-3]. In the atmosphere, N_2O is primarily originated from anthropogenic sources and also strongly influenced by human activities, in particular, the use of agricultural fertilizers[4,5]. However, its mixing ratios in the troposphere are typically from 270 to 330 parts per billion by volume (ppbv, 1 part in 10^9)[1,6] and have been measured upto ~ 2000 ppbv in areas where soils are cultivated with artificial fertilizers[4]. Therefore these values may differ strongly because of influence of the different anthropogenic and biogenic sources as well as depending on the level of local pollution. N_2O has atmospheric lifetime of several years (~120 years) and contributes to the ozone destruction in the stratosphere[7]. Because of its stability and long atmospheric lifetime, even a small change in concentration of N_2O will have long-term effects in the atmosphere[8]. Considering the environmental importance, real-time monitoring and molecule-specific detection of N_2O in the atmosphere with high sensitivity is of growing interest.

Laser-based high-resolution direct absorption spectroscopy and mid-infrared (mid-IR) molecular fingerprint region are ideally suited for trace gas analysis since most of the atmospheric species have their strong fundamental vibrational transitions in this spectral region, allowing highly sensitive and selective detection of trace gases. The recent commercial availability of continuous wave (cw) external-cavity quantum cascade lasers (EC-QCLs) in the mid-IR spectral region has opened up new possibilities for high-resolution spectroscopic detection of numerous trace molecular species in the atmosphere[9-11]. Because of their high output powers, room temperature operation, extremely narrow linewidth, wide tunability in addition to compactness, the *cw* EC-QCLs systems are gradually becoming the preferred mid-IR light sources for developing new-generation trace gas sensors in a wide range of applications, including atmospheric and environmental monitoring, industrial process monitoring and fundamental molecular spectroscopy.

However, to achieve the required sensitivities for real-time monitoring of trace species in ppbv down to the pptv (parts per trillion by volume, one part in 10^{12}) levels, cavity enhanced absorption spectroscopy exploiting high-finesse optical cavities such as cavity ring-down spectroscopy (CRDS)[12,13] can be used in combination with the most modern *cw*-EC-QCL technology. High-resolution CRDS technique has previously been proved to be a powerful method for trace gas detection in real-time with ultrahigh sensitivity and specificity in a variety of environments because of its ability to achieve a long effective optical path length (of the order of few kilometres) in a small volume sampling cell[14]. In a CRDS setup, the rate of decay of the intensity of light leaking from a high-finesse optical cavity is measured. The ring-down measurements are performed in the time-domain and thus independent of laser intensity fluctuations. Another salient feature of CRDS technique is that one can obtain the number density of a molecular species in an absolute scale without the need for secondary calibration if the line strength of the molecular transition is known. All these features of the CRDS technique are attractive for designing a trace gas sensor with a high degree of sensitivity and molecular selectivity. The aim of the present work is therefore to couple a widely tunable *cw* EC-QCL system to the high-resolution CRDS technique for accurate and selective measurements of N_2O in ppbv levels in ambient air.

The most widely used analytical method for measuring atmospheric N_2O is gas chromatography (GC) coupled with an electron-capture detector (ECD)[1,15]. Although this method is well-established for atmospheric monitoring but there are several intrinsic drawbacks to such method based on GC separation. Firstly, the instruments necessitate frequent calibration to confirm the accuracy of the measurements using calibration standards. Another drawback is that as the detector is not usually species selective, therefore a careful separation of the components in the sample is required prior to detection. As the GC separation of a large number of compounds is a time-consuming process, thus the short-time changes in mixing ratios are very difficult to measure using the GC-based method and consequently the methodology does not provide the real-time measurements. To overcome these issues, recently a number of groups have employed several laser-based spectroscopy techniques for the detection of N_2O levels in a variety of environments because of the wavelength dependent molecular absorption[3-6] although each technique has its own advantages and drawbacks. Vargas *et al.*[4,6] demonstrated the detection of N_2O levels released from soils using a pulsed distributed feedback (DFB)-QCL operating around 7.8 μm and photoacoustic spectroscopy (PAS) technique (which requires instrument calibration) and they reported a sensitivity limit of 50 ppbv. Jahjah *et al.*[16] have used a DFB-QCL operating at ~7.83 μm combined with quartz enhanced photoacoustic spectroscopy (QEPAS) technique for sensitive measurements of N_2O at the levels of 6 ppbv. Hamilton and Orr-Ewing[3] have recently demonstrated a cw DFB-QCL-laser based optical-feedback cavity-enhanced absorption spectroscopy (OF-CEAS) at 7.84 μm for the measurement of N_2O in air and they reported a sensitivity limit of 8 ppbv for N_2O at atmospheric pressure. More recently, Valiunas *et al.*[7] utilized a fiber laser-based intracavity absorption spectroscopy with a Herriot cell for sub-ppmv (parts per million by volume, 1 part in 10^6) detection of N_2O at 1.5 μm in the near-IR spectral region. Furthermore, Ma et. *al.*[17] demonstrated a N_2O sensor based on QEPAS technique employing a DFB-QCL and a minimum detection limit of 23 ppb at 100 torr pressure has been reported. Mohn et. *al.*[18] reported mid-infrared quantum cascade laser absorption spectroscopy (QCLAS) coupled with an automated pre-concentration unit for simultaneous and specific analysis of the stable isotopic species of N_2O. In view of the earlier studies, the detection of N_2O in ambient air using an EC-QCL coupled with high-resolution cw-CRDS technique is very limited.

In this chapter, we have demonstrated, the development of a high-resolution *cw*-CRDS method based on a widely tunable room temperature EC-QCL with mode-hop-free (MHF) frequency tuning capability operating at the centre wavelength of ~ 5.2 μm that allowed us to measure the atmospheric mixing ratios of N_2O in a variety of environments with high sensitivity and specificity. The ultrasensitive CRDS measurements of atmospheric N_2O in ppbv levels are performed in the mid-IR spectral region by recording a sharp rotationally resolved R(8e) ro-vibrational transition $[(11^10)\leftarrow(00^00)]$ in the combination band of N_2O centred at 1887.666 cm^{-1}, a region free from overlapping absorption features of other atmospheric species

3.2 Experimental technique

3.2.1 Instrumentation section:

A schematic diagram of the experimental setup is shown in figure 3.1. A widely tunable room-temperature external-cavity (EC) QCL (TLS-41053, Daylight Solutions, USA) was employed as an excitation source for N_2O detection in the mid-IR spectral region. The water-cooled *cw* EC-QCL produces radiation at a centre wavelength near 5.2 μm (1923.07 cm^{-1}) with a tuning range from 1832-1974 cm^{-1} and a specified fine MHF tuning range of 1847-1965 cm^{-1} which permitted the high-resolution ro-vibronic spectroscopic measurements. The QCL emits a single-mode collimated beam with a beam waist <0.5 mm and a narrow spectral linewidth of ~ 0.001 cm^{-1}. The laser provided output powers > 80 mW throughout the tuning range. Moreover, the QCL could be fine-tuned over ~ 1 cm^{-1} to acquire a rotationally resolved absorption line of N_2O using the piezoelectric transducer (PZT) attached to the tunable diffraction grating of the EC system. The collimated EC-QCL beam was primarily passed through an optical isolator (Innovation Photonics, FIO-5-5.3) to avoid back reflections from the optical cavity into the laser system and then the laser beam focused into a fast optical switching device such as an acousto-optic modulator (AOM) (IntraActionCorp; AGM-406B11M) which was connected to a 40 MHz RF driver (model: GE4020). The AOM facilitated the EC-QCL beam to be diffracted into the first and zeroth orders. The first order AOM output was coupled to ring-down cavity using two bending mirrors (BM1 and BM2) and the zeroth order beam was directed to wavemeter (Bristol Instruments, 621B) through another two bending mirrors (BM3 and BM4) for real-time monitoring of QCL wavelengths whilst a rotationally resolved spectrum was recorded with an accuracy of ± 0.001 cm^{-1}.

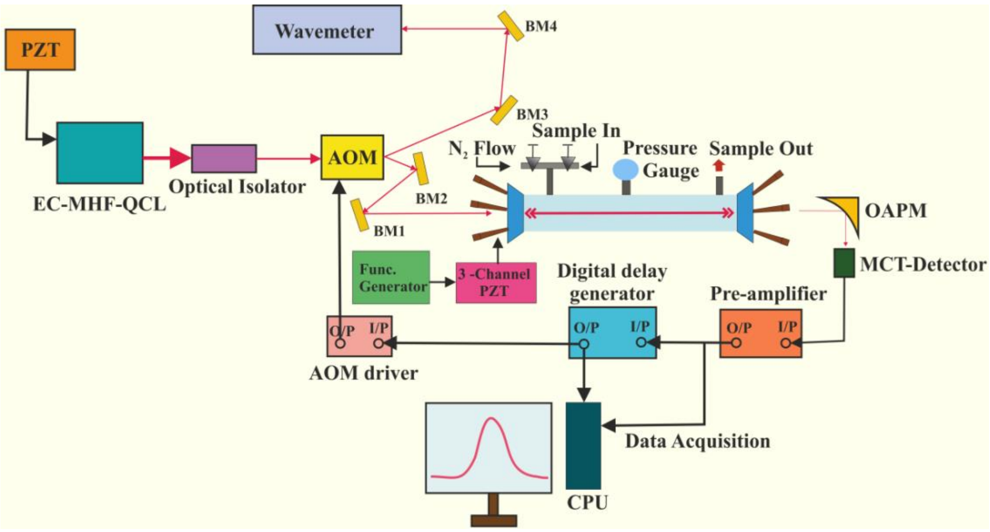

Figure 3.1 *Schematic diagram of cavity ring-down spectrometer set-up with an external-cavity quantum cascade laser (EC-QCL) at 5.2µm as a light source. AOM: acousto-optic modulator; PZT: piezo electric transducer; BM: bending mirror; OAPM: off-axis parabolic mirror; MCT Detector: Mid-IR Thermoelectrically cooled Mercury Cadmium Telluride (HgCdTe) photo-detector.*

The quartz-coated ring-down cell is 50 cm long. The cavity mirrors with 1" diameter and a radius of curvature of 1 m have a specified reflectivity of R ≥ 99.98% (CRD Optics Inc.; USA) over the full tuning range of the QCL light. The QCL beam exiting the cavity was focused by a gold-coated off-axis parabolic mirror (10.16 cm focal length, Newport Corporation, 50338 AU) and subsequently detected by a three-stage TE-cooled photovoltaic mercury cadmium telluride (MCT) detector (VIGO, PVI-

3TE-6) which was optically immersed in a high refractive index, hyper hemispherical lens. The output signal from the detector was sent to a low-noise voltage preamplifier (Stanford Research Systems, SR560) for further amplification and filtering. The resulting ring-down signal was then recorded by a high-speed data-acquisition card (PCI 5122, National Instruments) and further processed using a custom written LabVIEW program on a computer.

To achieve the laser cavity coupling condition, a triangular voltage (V_{pp} = 5v, frequency = 53 Hz) was applied in parallel to three pizeo-electric transducers (PZT, Thorlabs PE4) which were attached to one of the cavity mirrors. During the scanning of the CRD cell, the laser was kept at a fixed frequency 1887 cm^{-1} and the triangular voltage facilitates the mirror to move back and forth which in turn modulate the length of the cavity over one free spectral range (FSR).

When the laser frequency overlaps with one of the cavity modes, a rapid increase of the detector signal (TEM_{00} modes) was observed. A typical set of TEM_{00} modes observed during mirror oscillations when the laser light was allowed to pass directly along the central axis of the cavity as shown in figure 3.2 (a). When the QCL light intensity in the RDC reached a pre-selected threshold level, a digital delay generator (Stanford Research systems, DG565) was utilized to extinguish the first-order diffracted beam from the AOM, thus initiating an exponential decay of intra-cavity light as a function of time (figure 3.2 (b)). The exponential decay was then recorded by a PC holding 14 bit, 100-MHz bandwidth data-acquisition card capable of collecting the data at a sampling rate of 100 MS/s (PCI 5122, National Instruments) and analysed using custom written LabVIEW programs.

3.2.2 Determination of ring-down time and detection limits for the CRDS system

The reciprocal of the time constant (τ) is called the ring-down decay rate constant (k) and the changes in the decay constant (Δk) in presence and absence of the analyte molecule species in the cavity is directly related to the absorption coefficient, α by $\Delta k = c\alpha$ where c is the speed of light. The concentration of the absorbing species [X] is related to $\alpha = \sigma_\lambda[X]$ where σ_λ is the wavelength dependent absorption cross-section for a specified spectroscopic transition at a particular pressure and temperature of the gas sample. The minimum absorption coefficient and hence the minimum detection limit of an analyte is expressed by

$$\alpha_{\min} = \frac{1}{c\tau_0} \frac{\Delta\tau_{\min}}{\tau_0} \tag{3.1}$$

$$\text{and } [X]_{\min} = \frac{\alpha_{\min}}{\sigma_\lambda} \tag{3.2}$$

where, τ_0 is the empty cavity ring-down time (RDT) and $\Delta\tau_{min}$ is the smallest detectable change in τ in presence of an absorbing molecular species inside the cavity. Figure 3.3 (a) shows the distribution of the ring-down times in empty cavity condition at a fixed EC-QCL frequency.

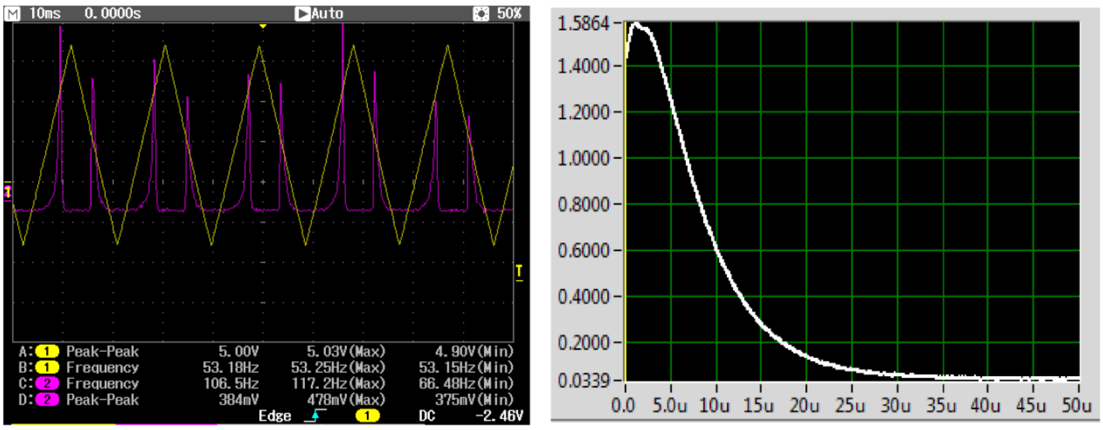

(a) **(b)**

Figure 3.2 *(a) A typical set of TEM_{00} modes under the laser–cavity resonance condition at a fixed wavenumber during the scanning of the optical cavity by a triangular signal over one FSR. (b) An empty cavity RDT trace of LabVIEW front panel.*

The distribution can be fitted with a Gaussian function, exhibiting $<\tau_0>$ =5.56 μs and $\Delta(\tau_0)/<\tau_0>$ =3.18×10^{-4}. This indicates that the standard deviation of a single-shot absorption measurement is α =1.9×10^{-9} cm^{-1} according to the equation (3.1). Moreover, the light trapped inside the cavity travels an optical path length of ~ 1.67 km in this time and the round-trip time of the trapped light inside the cavity was found to be 3.3 ns. From the experimentally obtained ring-down time, we estimated that the actual mirror reflectivity was R = 99.97%.

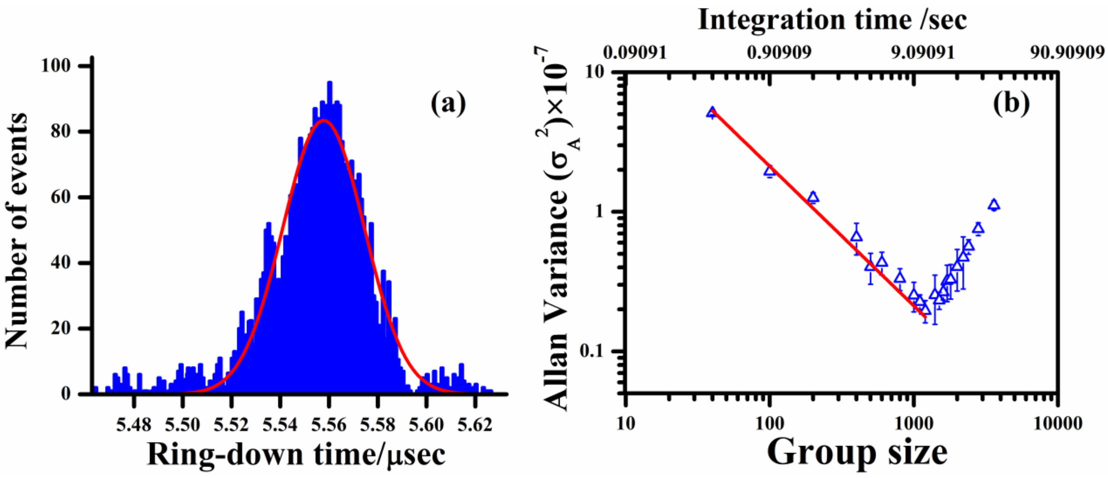

Figure 3.3 *(a) Distribution of the ring-down times at a fixed laser frequency. (b) An Allan-variance plot to estimate the stability of the spectrometer.*

It is also noteworthy to mention here that in our *cw*-CRDS set up, the width of an individual cavity mode enabled us to assess the laser linewidth ($\Delta\nu_{QCL}$), because it represents the time required for a moving cavity mode to cross the laser line. From our experiment, $\Delta\nu_{QCL}$/ FSR = Δt (cavity mode width) / Δt (FSR) = 0.062. Taking into account the cavity FSR = $c/2l$ = 300 MHz (0.01 cm^{-1}), we obtain $\Delta\nu_{QCL}$= 18.2 MHz (0.0006 cm^{-1}), which is in agreement with the linewidth reported for Daylight Solutions MHF-EC-QCL (0.0003 cm^{-1}). In our experiment it has been considered that the spectral width of the cavity mode $\Delta\nu_{cav}$ is negligibly small compared to the laser linewidth. In fact, from the measured τ_0=5.56 µs and the relation $\Delta\nu_{cav} = 1/2\pi\tau_0$ it follows that $\Delta\nu_{cav}$ = 28.6 kHz.

However, In our current EC-QCL-based high-resolution *cw*-CRDS setup, while scanning across a rotationally resolved R(8e) line of N_2O at 1887.666 cm^{-1}, a typical detection limit corresponded to $\alpha_{min} = 4.8 \times 10^{-9}$ cm^{-1}. This value was calculated using the typical ring-down time of 5.56 µs and standard deviation (1σ) of 0.08% with averaging 6 RDT determination. Based on the value of α_{min}, we also determined the minimum detectable concentration for N_2O in our present setup and using equation (3.2) we found a value of $[X]_{min}$=1.13×10^{11} molecules/cm^3 when the CRDS measurements are constrained under the Doppler-broadened limiting conditions.

However, with inclusions of pressure broadening effects on the spectral line by an ambient pressure of 1 atm of air (air broadening coefficient, γ_{air} (N_2O) = 0.08 cm^{-1} atm^{-1}), the detection limit for N_2O would then correspond to 4.5 ppbv. The estimated detection limit is sufficient for direct detection of ambient N_2O levels. We have also illustrated the typical detection limits for sensing of N_2O obtained by several other groups (Table 3.1) using several other spectroscopy techniques. We also estimated the noise-equivalent absorption (NEA) coefficient of the present *cw*-CRDS apparatus as an alternative to the detection limit according to the equation as described in chapter 2.

$$NEA = \sqrt{\frac{2}{f_{rep}}}\alpha_{\min}$$

where f_{rep} represents the data collection rate. In the present setup, we obtained a typical NEA value of 7.16×10^{-10} cm^{-1} $Hz^{-1/2}$ with 90-Hz data accumulation of individual ring-down events.

Table-3.1 Typical detection limits of N_2O reported by different research group

	Min detectable Concentration of N_2O (in air)	Technique	Remarks
G5131-i Picarro N_2O analyzer	~ 0.05 ppb	*Cavity Ring-down Spectroscopy (CRDS)*	• Fully automated and commercial system for high precision continuous measurement of N_2O in ambient air. • The system is capable of measuring the isotopic species of N_2O.
J. P. Lima *et. al*[6]	84 ppb	*Photoacoustic Spectroscopy (PAS)*	• Lab-based setup.
F. M. Cuoto *et. al.*[4]	50 ppb	*Photoacoustic Spectroscopy (PAS)*	• Lab-based setup.
M. Jahjah *et. al.*[16]	6 ppb	*Quartz Enhanced Photoacoustic Spectroscopy (QEPAS)*	• Lab-based setup.
J. Mohn[18].	-	*Multipass Absorption Spectroscopy*	• Lab-based setup. • Pre-concentration technique is utilized • The system is capable of measuring the isotopic species of N_2O.
Y. Ma *et al.*[17]	23 ppb	*Quartz Enhanced Photoacoustic Spectroscopy (QEPAS)*	• Lab-based setup.
Present study	4.5 ppb	*Cavity Ring-down Spectroscopy (CRDS)*	• Lab-based setup.

3.2.3 Allan Variance analysis

We estimated the stability of the current CRDS instrument by Allan variance analysis. Figure 3.3 (b) demonstrates a graph of Allan variance (σ^2_A) plot against integration time at fixed wavenumber~ 1887.00 cm^{-1} with empty cavity condition. In the initial part of the graph, where σ^2_A is decreasing with increasing integration time and the gradient of the best fitted line is -1 which indicates that the cavity is in white noise region[19] and σ^2_A improves further by the increase of the integration time. For our CRDS set up, the optimum integration time was found to be ~15 s which corresponds to 1400 ring-down decay signals at the data accumulation rate used. After this point there in no further improvement in the σ^2_A and consequently there is no benefit in additional signal averaging because numerous instabilities arise in the system.

3.3 Results and Discussion:

We first assessed the performance of the EC-QCL-based N_2O sensor exploiting the CRDS technique by measuring a certified calibration gas mixture of 13±0.5 ppmv N_2O in N_2 (Air Liquide, UK, 99.99%) inside the ring-down cell. The Doppler-limited studies were conducted by injecting the gas sample in the cavity with different pressures. Figure 3.4 (a) shows an example of the high-resolution *cw*-CRDS spectrum probing the R(8e) ro-vibronic transition of N_2O centred at 1887.666 cm^{-1} with a pressure of 8 Torr inside the cavity. The line integrated absorption cross-section is $\sigma_{line} = 1.5\times10^{-22}$ cm^2 $molecule^{-1}$ cm^{-1} reported in the HITRAN database at 296 K[20]. The measured Doppler width is 0.003506 cm^{-1} which is in good agreement with the calculated value of 0.0035062 cm^{-1}. The rotational R (8e) absorption line was fitted by a Gaussian line-shape function with FWHM of 0.00361 cm^{-1} which corresponds to the expected Doppler broadening at the measured wavelength. The integrated area was then used to calculate the concentration of N_2O in the cavity using the known value of σline at 1887.666 cm^{-1}. We measured the N_2O concentration inside the ring down cavity (RDC) of $[X]_{N2O} = (3.40 \pm 0.02)\times10^{12}$ $molecules/cm^3$. In figure 3.4(b), the absorption coefficient (α) is plotted as a function of the N_2O concentration at different pressures inside the optical cavity. The change in decay rate (Δk) at different N_2O concentrations divided by the speed of the light yield the absorption coefficients at a range of N_2O partial pressures inside the cavity.

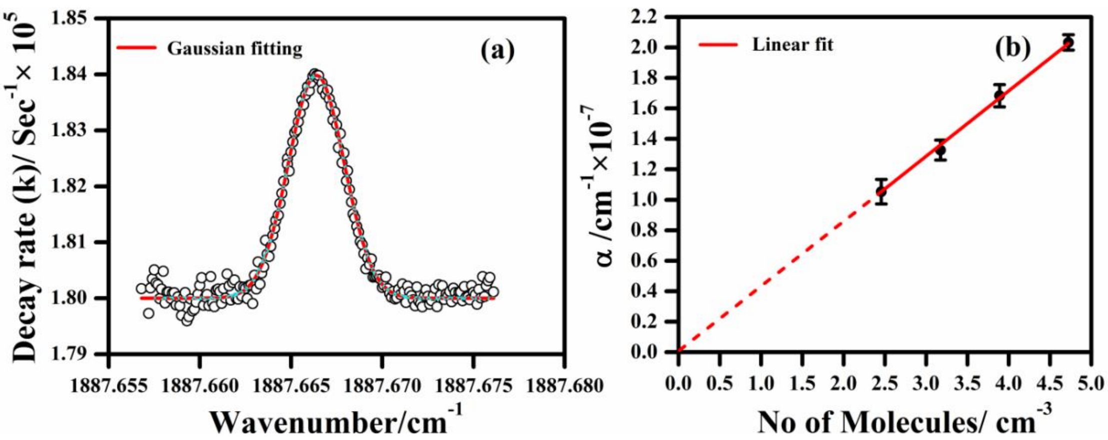

Figure 3.4 *(a) CRDS spectrum of R(8e) rotational line of N_2O at 1887.666 cm^{-1} (b) Plot of absorption coefficient (α) as a function of N_2O concentrations inside the optical cavity to determine the line integrated absorption cross-section (σ_i) of N_2O.*

The errors correspond to the standard errors (S.E) from the mean values when three or more spectra are recorded. The wavelength dependent absorption cross-section (σ_λ) of N_2O at a particular wavelength was derived from fitting of each spectral feature with a Gaussian line- shape function whose FWHM was constrained to Doppler broadening at 296 K. The linear relationship between α and N_2O concentration enabled us to determine σ_λ from the gradient of the straight line. σ_λ calculated in this way can be directly converted to line integrated absorption cross-section (σ_i) by multiplying with experimentally observed Doppler width at the centre wavelength 1887.666 cm^{-1} (figure 3.4b). Thus the $\sigma_{experimental} = (1.503 \pm 0.01) \times 10^{-22}$ cm^2 $molecule^{-1}$ cm^{-1} which is in excellent agreement with the value reported in the HITRAN database[20].

Next in order to illustrate the CRDS measurements under the influences of pressure broadening effects, we recorded the CRDS spectra of N_2O beyond the Doppler-broadened limiting conditions. An accurate measurement of the pressure broadening coefficient for the rotational line utilized to detect N_2O is important to allow detection limits obtained at low pressure to be scaled correctly for atmospheric sample measurements. The pressure broadening coefficient of the R(8e) rotational line of N_2O was determined with increasing pressure of air inside the optical cavity.

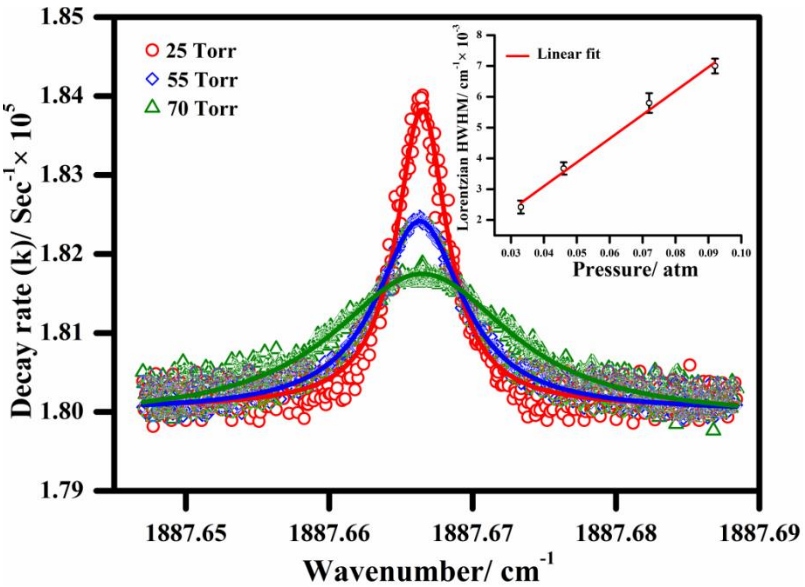

Figure 3.5 *Demonstrates the pressure broadening effects of the R(8e) rotational line .The inset figure shows the variation of HWHM at different pressures inside the cavity. The pressure broadening coefficient was determined to be 0.077±0.001 $cm^{-1}atm^{-1}$.*

Lorentzian profiles centred at known line positions (as obtained from low pressure spectra) were used to fit the shape of the spectra, with the FWHM of Lorentzian functions floated in the fit. Figure 3.4 illustrates the pressure broadening effects on the R(8e) absorption line. The inset in figure 3.5 depicts the Lorentzian HWHM as a function of air pressure and the gradient is equal to the pressure broadening coefficient and is 0.077±0.01 cm^{-1} atm^{-1} which is in good agreement with the HITRAN database value of 0.08 cm^{-1} atm^{-1}.

Finally, we have investigated the applicability of *cw*-CRDS technique combined with the EC-QCL technology for measuring trace amounts of N_2O levels in real atmospheric samples. The samples were collected from the five different localities surrounding S. N. Bose Centre, Kolkata on seven consecutive days (November, 4-10, 2016) in two different periods, morning (07:00-09:00 h) and afternoon (14:00-16:00 h). The sub-areas of our study included industrial sector (L1), highly traffic area (L2), residential complex (L3), agricultural land (L4) and garbage disposal ground of Kolkata metropolitan (L5). Air samples were analyzed by the *cw*-CRDS setup and the measured N_2O mixing ratios in the atmosphere were from 399 pbbv to 604 pbbv (see in Table 3.2) which lies in the typical range of N_2O emitted in the atmosphere depending on the level of local pollution. In our study, whilst we observed a significant change in N_2O levels in different sub-areas, interestingly we also observed a statistically significant difference ($p<0.001$) in N_2O concentrations between morning and afternoon sessions of the day in all sub-areas apart from the residential complex area ($p = 0.03$) (figure 3.6)[21,22]. In the cultivated land area, we found a significant change in N_2O levels in the afternoon session. This observation might be attributed to the release of N_2O from the soil by an increase in soil microbial activity in the afternoon and also for use of different types of organic and inorganic fertilizers in the agricultural land as the samples were collected from such areas. On the other hand, in our study a higher level of N_2O was observed in the waste disposal land compared to the other sub-areas. This is possibly caused by the enhancement of biological processes of nitrification and denitrification of organic material by the different types of bacteria and fungus.[23] Moreover, we also did not observe any significant changes of N_2O levels in the morning period between the traffic area and industrial sector, but N_2O concentration rises in the afternoon which is most likely a result of higher emission of anthropogenic sources in that period.

Table-3.2 Distribution of N_2O concentration (in ppb) in different localities

Date	L1		L2		L3		L4		L5	
	Morning	Afternoon	Morning	Afternoon	Morning	Afternoon	Morning	Afternoon	Morning	Afternoon
4.11.2016	399 ± 5	527 ± 7	410 ± 4	549 ± 7	401 ± 3	409 ± 5	456 ± 4	570 ± 3	495 ± 8	595 ± 5
5.11.2016	402 ± 4	533 ± 6	418 ± 3	553 ± 7	404 ± 3	413 ± 4	454 ± 6	570 ± 3	498 ± 6	604 ± 6
6.11.2016	404 ± 7	529 ± 7	413 ± 5	554 ± 4	401 ± 5	404 ± 8	453 ± 4	568 ± 4	498 ± 3	600 ± 3
7.11.2016	403 ± 9	528 ± 4	412 ± 5	553 ± 6	402 ± 5	404 ± 6	457 ± 3	574 ± 5	499 ± 7	596 ± 5
8.11.2016	409 ± 8	528 ± 4	412 ± 4	555 ± 5	402 ± 6	408 ± 6	458 ± 3	576 ± 7	499 ± 6	598 ± 8
9.11.2016	415 ± 6	529 ± 4	416 ± 3	549 ± 6	401 ± 7	403 ± 6	455 ± 4	574 ± 6	506 ± 4	597 ± 7
10.11.2016	410 ± 4	529 ± 6	411 ± 5	556 ± 5	407 ± 6	402 ± 5	454 ± 5	569 ± 6	501 ± 3	598 ± 4

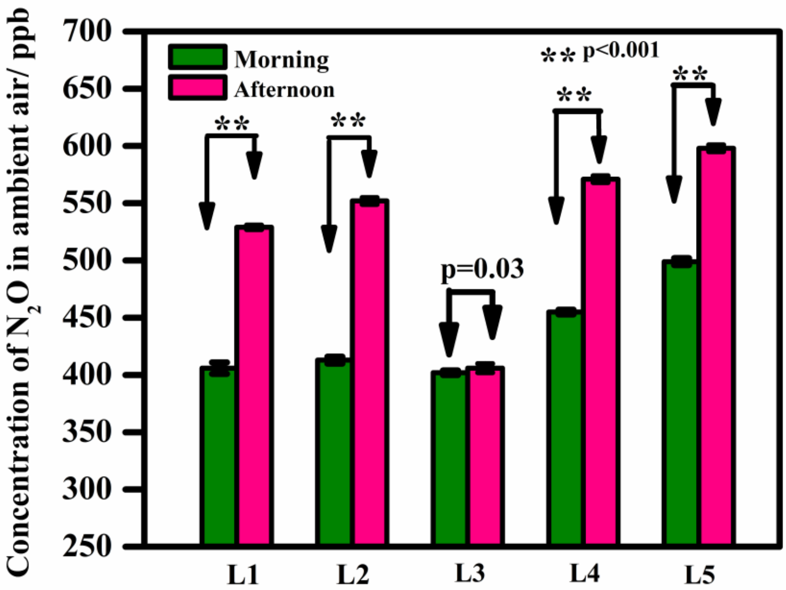

Figure 3.6 *Variation of ambient N_2O mixing ratios in different periods of the days in various sub-areas. L1: industrial sector, L2: highly traffic area, L3: residential complex, L4: agricultural land and L5: garbage disposal ground of Kolkata metropolitan.*

3.4 Conclusions:

The EC-QCL based cw-CRDS detection described in this work offers an effective method for direct and quantitative measurement of N_2O in ambient air with high sensitivity at ppbv levels and high molecular selectivity. The high selectivity in the measurements arises from the high-resolution spectroscopic detection and probing a sharp, rotationally resolved R(8e) absorption line of N_2O that has well-defined central frequency and a Doppler-broadened line profile. We did not observe any overlapping absorption features of other dominant atmospheric constituents such as H_2O and CO_2 in this spectral region. Consequently, the use of EC-QCL-based high-resolution cw-CRDS methodology with careful wavelength selection in the MHF frequency tuning range also eliminates the necessity for instrument calibration using the standard calibration gas mixtures. Furthermore, as the detection of N_2O is performed at the low pressure used in the RDC, the CRDS measurement thus avoids any deleterious effects of pressure broadening by ambient air and consequently also works in favour of improving detection limits. The detection limit of the current EC-QCL-based CRDS sensor for N_2O detection could be improved further by the improvements on the performance of the RDC, associated optics and laser. We also believe that the present CRDS technique has enormous potential not only to monitor simultaneously many other trace atmospheric species along with N_2O within the tuning range of the laser, but also the N2O sensor to be made portable in the future for field deployment which is facilitated because of the compactness and room temperature operation of the EC-QCL light source.

3.5 References

1. T. D. Rapson and H. Dacres, *Trends. Anal. Chem.*, 2014, **54**, 65.
2. S. Kang, S. Kim, S. Kang *et al.*, J. Lee, C. S. Cho, J. H. Sa and E. C. Jeon, *Sensors*, 2014, **14**, 14399.
3. D. J. Hamilton and A. J. Orr-Ewing, *Appl. Phys. B*, 2011, **102**, 879.
4. F. M. Couto, M. S. Sthel, M. P. P. Castro *et al*., *Appl. Phys. B*, 2014, **117**, 897.
5. A. J. Thomson, G. Giannopoulos, J. Pretty *et al*., *Phil. Trans. R. Soc. B*, 2012, **367**, 1157.
6. J. P. Lima, H. Vargas, A. Miklos *et al*., *Appl. Phys. B*, 2006, **85**, 279.
7. J. K. Valiunas, G. Stewart and G. Das, *IEEE Photonic Tech Lett*., 2016, **28**, 359.
8. J. Wojtas, Z. Bielecki, T. Stacewicz *et al.*, *Acta. Phys. Pol. A*, 2011, **120**, 794.
9. R. Lewicki, H. Doty, R. F. Curl *et al.*, *PNAS*, 2009, **106**, 12587.
10. Y. Cao, N. P. Sanchez, W. Jiang *et al.*, *Opt. Express*, 2015, **23**, 2121.
11. J. Li, U. Parchatka and H. A. Fischer, *Anal. Methods*, 2014, **6**, 5483.
12. M. Pradhan, M. S. I. Aziz, R. Grilli *et al.*, *Environ. Sci. Technol*., 2008, **42**, 7354.
13. M. Pradhan, R. E. Lindley, R. Grilli *et al*., *Appl. Phys. B*, 2008, **90**, 1.
14. A. M. Prakes, R. E. Lindley and A. J. Orr-Ewing, *Phys. Chem. Chem. Phys.*, 2004, **6**, 5313.
15. A. Hensen, U. Skiba and D. Famulari, *Environ. Res. Lett*., 2013, **8**, 1.
16. M. Jahjah, W. Ren, P. Stefanski *et al.*, *Analyst*, 2014, **139**, 2065.
17. Y. Ma, R. Lewicki, M. Razeghi et al., *Opt. Express*, 2013, 21, 1008.
18. J. Mohn, B. Tuzson, A. Manninen *et al.*, *Atmos. Meas. Tech*., **5**, 2012, 1601.
19. P. Werle, R. Mucke, F. Slemr, *Appl. Phys. B*., 1993, **57**, 131.
20. L. S. Rothmana, I. E. Gordona, A. Barbeb *et al*., *J. Quant. Spectrosc. Radiat. Transf*., 2009, **110**, 533.
21. G. Rubasinghege and V. H. Grassian, *J. Phys. Chem. A*, 2009, **113**, 7818.
22. D. M. B. Lesko, E. M. Coddens, H. D. Swomley *et al.*, *Phys. Chem. Chem. Phys.*, 2015, **17**, 20775.
23. M. A. Kebede, D. L. Bish, Y. Losovyj *et al.*, *Environ. Sci. Technol.*, 2016, **50**, 8649.

4 Simultaneous monitoring of multiple chemical species using high-resolution CRDS technique

Contents

4.1 Introduction

The innovation and the recent technological advances of continuous wave (cw) external-cavity (EC) quantum cascade lasers (QCLs) with mode-hop-free (MHF) frequency tuning capability operating in the mid-infrared (mid-IR) molecular fingerprint region covering the spectral range 4 to 24 μm have transformed the way to access strong fundamental rotational-vibrational transitions of numerous molecular species[1-3]. Now-a-days, the cw-EC-QCLs are becoming very popular mid-IR light sources for high-resolution fundamental molecular spectroscopy and chemical sensing applications because of their high output powers, room temperature operation, wide tunability, intrinsic narrow linewidth, and compactness[3-8]. However, when such widely tunable cw-EC-QCL technology is coupled with high-finesse optical cavity-enhanced absorption spectroscopy (CEAS) techniques such as cavity ring-down spectroscopy (CRDS)[9-11], the detection limits of ppbv (parts per billion by volume) down to the pptv (parts-per-trillion by volume) levels are easily achieved[12,13] and the new methodology will allow for simultaneously monitoring of multiple species in a variety of environments in real-time.

The laser-based CRDS is a highly-sensitive direct optical absorption technique that exploits the measurements of decay rate of light circulating in a high-finesse optical cavity. The scheme provides long effective path lengths of the order of several km in a small cavity volume and thus improved sensitivity of detection. In CRDS, one can easily calculate the number density of a molecular species in an absolute scale from the knowledge of the molecular absorption cross-section without need for secondary calibration standard. Additionally, the CRDS measurements are performed in the time-domain and thus it is insensitive to laser intensity fluctuations, which enables the technique to reach a shot-noise-limited sensitivity[14]. Therefore the application of CRDS technique with an EC-QCL light source offers an attractive new option for mid-IR high-resolution absorption spectroscopy. The aim of the present study was thus to exploit the new-generation widely tunable EC-QCL technology coupled with an optical cavity-enhanced cw-CRDS detection technique for high sensitive, selective, and quantitative optical measurements of multiple trace molecular species by probing rotationally resolved ro-vibronic transitions in the mid-IR spectral region. The MHF laser frequency tuning along with extremely narrow line-width of ~0.0001 cm^{-1}, the new-generation EC-QCL technology makes feasible the simultaneous detection of numerous molecular species probing their respective rotationally resolved absorption line, employing a single QCL within a relatively small spectral range of ~ 0.05 cm^{-1}. In this study, we have specifically targeted some unique panels of molecular species within the tuning range of the QC laser which are important for various real-world applications involving environmental sensing and atmospheric chemistry (e.g., C_2H_2 and N_2O) as well as non-invasive biomedical diagnostics (e.g., NO and OCS). In the medical field, exhaled nitric oxide (NO) is considered to be an important biomarker for asthma and other respiratory diseases[15,16]. On the other hand, carbonyl sulphide (OCS) has been proposed as a marker for liver related diseases[16,17]. However, one breath molecule may be linked with multiple diseases and conversely, one particular disease or metabolic disorder can be marked by more than one breath molecular species. Furthermore, in the field of environmental science, the monitoring of acetylene (C_2H_2) and nitrous oxide (N_2O) in ambient air is of immense importance because both play an important role in atmospheric chemistry and photochemistry[18-23]. Therefore, simultaneous and molecule-specific real-time detection of these particular molecular species with high-sensitivity are of increasing interest and still remains a challenge.

In this chapter, we demonstrate the simultaneous monitoring of multiple chemical species using the high resolution CRDS technique coupled with a *cw*-EC-QCL system operating at $\lambda \sim 5.2$ μm. We subsequently demonstrate its application for high-resolution rotational-vibrational spectroscopy along with simultaneous detection of multiple trace molecular species such as NO, OCS, N_2O and C_2H_2 with high sensitivity and specificity in ambient air as well as in human breath by probing their Doppler-limited or pressure-broadened ro-vibronic transitions in the mid-IR region within the tuning range of the present QC laser.

4.2 Experimental Arrangement

The schematic of the EC-QCL-based CRDS setup is depicted in figure 4.1. The light source consists of a water-cooled *cw* EC QC laser (TLS-41053, Daylight Solutions, USA) which operates in the centre wavelength $\lambda \sim 5.2$ μm (1923.07 cm^{-1}) in the mid-IR spectral region. The *cw*-EC-QCL system can continuously be tuned from 1832-1974 cm^{-1}, allowing a MHF range of 1847-1965 cm^{-1} with output powers ≥ 80 mW over this tuning range. An optical isolator (FIO-5-5.3, Innovation Photonics) was used at the laser output to prevent optical feedback from back-reflected light.

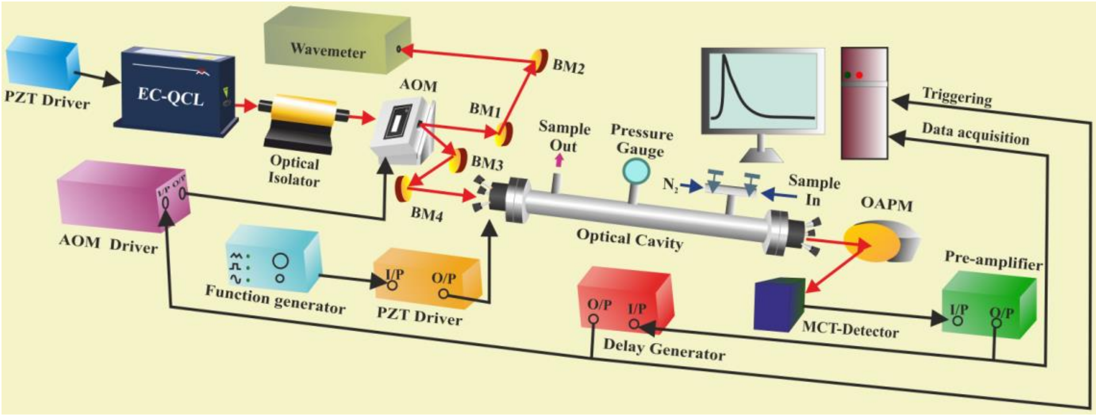

Figure 4.1 *Schematic diagram of the cavity ring-down spectrometer coupled with an external-cavity quantum cascade laser (EC-QCL) at 5.2µm.*

The output of the QCL beam from the isolator was then passed through an acousto-optic modulator (AOM) (AGM-406B11M, IntraActionCorp.). The AOM was employed as a fast optical switch and the first-order deflected beam from the AOM was utilized for the ring-down experiments. The zeroth-order AOM output was directed to a wavemeter (621B, Bristol Instruments, USA) for monitoring of laser wavelengths in real-time with an accuracy of ± 0.001 cm^{-1} whilst a rotationally resolved spectrum was recorded. The laser can be fine tuned over the rotationally resolved absorption line by utilizing the piezoelectric transducer (PZT) attached to the intra-cavity grating of the EC-QCL system.

The cylindrical ring-down cavity (RDC) consisted of two ultra-high reflective mirrors (manufacturer specified reflectivity R ≥ 99.98% at 5.2 µm, 1" diameter and radius of curvature =1 m; CRD Optics Inc.; USA) separated by a distance (l) of 50 cm, which corresponds to a free spectral range (FSR = $c/2l$) of 300 MHz (0.01 cm^{-1}) and optical finesse of ~15706. The RDC was connected to a vacuum system that allowed the measurements of molecular absorption with different sample concentrations. The light behind the RDC was focused by a gold-coated off-axis parabolic mirror (10.16 cm focal length, Newport Corporation, 50338 AU) onto a thermoelectrically cooled photovoltaic MCT detector (VIGO PVI-3TE-6) and subsequently output of the detector signal was amplified by an external low-noise voltage preamplifier (Stanford Research Systems, SR560). However, to enable the periodic laser-cavity coupling, one cavity mirror was placed in a mirror mount with three piezo electric transducers

(PZT, Thorlabs PE4) and a triangular voltage was applied in parallel to three PZTs, making the mirror move back and forth. In this way, the cavity length was modulated over one FSR to ensure TEM_{00} excitation at each laser frequency. The intra-cavity light is build up when the laser frequency comes into resonance with one of the cavity modes. When the light intensity in the cavity reached a user-specified threshold level, a trigger pulse from a digital delay generator (Stanford Research systems, DG565) is sent to the AOM to switch-off the first-order diffracted beam and consequently the light intensity decays exponentially with time. This exponential decay was captured by a high-speed data-acquisition card with a sampling rate of 100 MS/s (14 bit, 100-MHz bandwidth digitizer; PCI 5122, National Instruments) and subsequently analysed by weighted least-squares fittings using custom written LabVIEW 8.0 software.

However, in the present EC-QCL based CRDS setup, the typical empty cavity ring-down time (τ_0) was 5.51 μs and standard deviation (1σ) of 0.08% with averaging of 6 RDT determinations. Consequently, the light trapped inside the RDC traversed an effective optical path length of ~ 1.7 km and the round-trip time of the light inside the cavity is 3.3 ns. Based on the experimentally obtained RDT, we estimated that the actual mirror reflectivity in the current EC-CRDS setup was R = 99.969% which provides the finesse of the optical cavity~10132 and line-width of the optical cavity mode ~ 29.6 KHz. We also calculated the laser linewidth from the width of an individual cavity mode in our experiments and we obtained $\Delta\nu_{QCL}$ = Δt (cavity mode width)×FSR/Δt (FSR) ~ 18.2 MHz (0.0006 cm^{-1}), which was in excellent agreement with the manufacturer specified linewidth of QCL (~ 0.0003 cm^{-1}). It is also worth mentioning that in our setup the spectral width of the cavity mode (i.e. $\Delta\nu_{cav} = 1/2\pi\tau_0$ = 28.88 kHz ~ 29 KHz) was considerably small when it is compared with the QCL linewidth (i.e. $\Delta\nu_{QCL}$ ~ 18.2 MHz). Moreover, in the present EC-QCL system when combined with the CRDS technique, the typical detection limit corresponded to αmin ~ 4.8×10^{-9} cm^{-1} while scanning across a rotational line of a gaseous species of interest in this study and the noise-equivalent absorption (NEA) coefficient of the order of ~10^{-10} $cm^{-1}Hz^{-1/2}$ was also achieved.

4.3 Results and Discussion:

4.3.1 Assessment of the CRDS set-up using standard calibration gas

To evaluate the performance of the mid-IR EC-QCL system exploiting the cw-CRDS detection technique, we first focused to target absorption lines of a particular molecular species for example, acetylene (C_2H_2) which is one of the simplest non-methane volatile organic compounds (VOCs) that has well-resolved ro-vibrational spectrum within the MHF tuning range of the current QC laser. To check the ability of performing quantitative measurements of C_2H_2, we injected a certified gas sample of 5±0.25 ppm C_2H_2 in N_2 (Air Liquide, UK, 99.99 %) inside the optical cavity. An example of the high-resolution cw-CRDS absorption spectrum of C_2H_2 probing the P(13e) rotational line of the $(0000^00^0)\rightarrow(0002^11^2)$ combination band of C_2H_2 centred at peak wavenumber of 1909.597 cm^{-1} is shown in figure 4.2(a) as recorded with a pressure of 15 Torr inside the optical cavity. To determine the absolute concentration in the cavity, the absorption line was fitted by a Gaussian line-shape function with FWHM of 0.00471 cm^{-1} under the Doppler-broadened limiting condition.

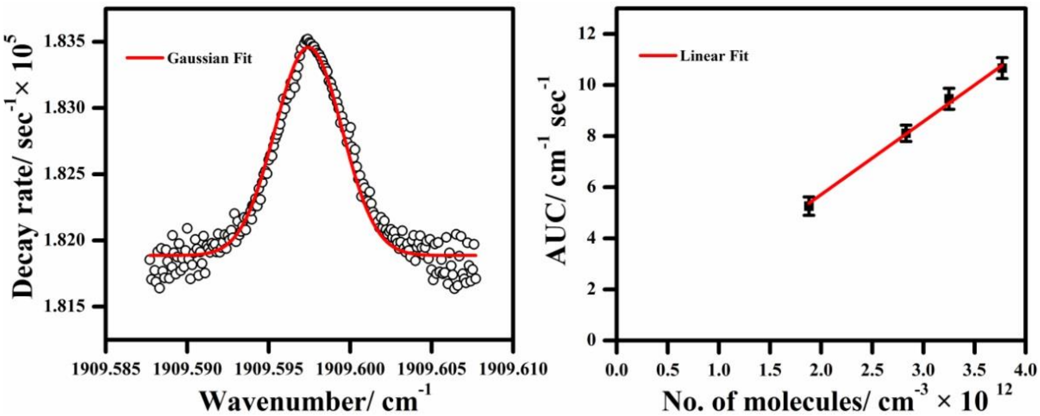

Figure 4.2 *(a) Depicts CRDS spectra of P(13e) rotational line of the ($2\nu_4+\nu_5$) vibrational combination band of C_2H_2 at 1909.597cm^{-1} to illustrate the performance of the set-up. (b) Plot of area under curve (AUC) at different C_2H_2 concentration inside the optical cavity to determine the line integrated absorption cross-section (σ_i) of C_2H_2.*

We utilized the integrated area of the absorption line and line-integrated absorption cross-section $\sigma_{line}=1.093\times10^{-22}$ $cm^2molecule^{-1}cm^{-1}$ at 296 K from the high-resolution transmission (HITRAN) database[24] to calculate the concentration of C_2H_2 in the cavity and we obtained $[X]_{C2H2}=(2.39\pm0.07)\times10^{12}$ molecules cm^{-3}.

We subsequently verified the absorption cross-section data reported in the HITRAN database[24] by the present EC-QCL-based CRDS detection method to ensure the suitability of the measurements. For this purpose, we have plotted the area under the curve (AUC) as a function of C_2H_2 concentration at different pressure inside optical cavity as shown in figure 4.2(b). The error bars correspond to the standard errors (S.E) from the mean when more than three spectra were recorded. The Gaussian line-shape function was used to fit each spectral line with FWHM constrained to Doppler broadening at 296 K. The linear relationship between AUC and C_2H_2 concentration enabled us to determine the line-integrated absorption cross-section (σ_i) at particular wavenumber. The gradient of the straight line divided by the speed of light gives the line integrated absorption cross-section $(1.1\pm0.01)\times10^{-22}$ cm^2 $molecule^{-1}$ cm^{-1}, which was in excellent agreement (to within 0.6%) with the value reported in the HITRAN database[24]. We next investigated the pressure broadening effects on the P (13e) ro-vibrational line in order that the measurements were not only constrained under the Doppler-broadened limiting conditions.

Figure 4.3(a, b, c) illustrates the broadening of the absorption line as the pressure of air inside the cavity increased. Under this condition, we utilized Lorentz lineshape function to ensure reliable fittings on such unblended rotational lines. Lorentzian profiles centred at known line positions (as obtained from low pressure spectra) were used to fit to the shapes of the spectra, with the FWHM of the Lorentzian functions floated in the fit. The pressure broadening coefficient was determined to be γ_{air} = 0.0698 ± 0.01 $cm^{-1}atm^{-1}$ from the plot of Lorentzian HWHM (cm^{-1}) of the spectral lines versus the pressure (in atm) of air used (Figure 4.3(d)).

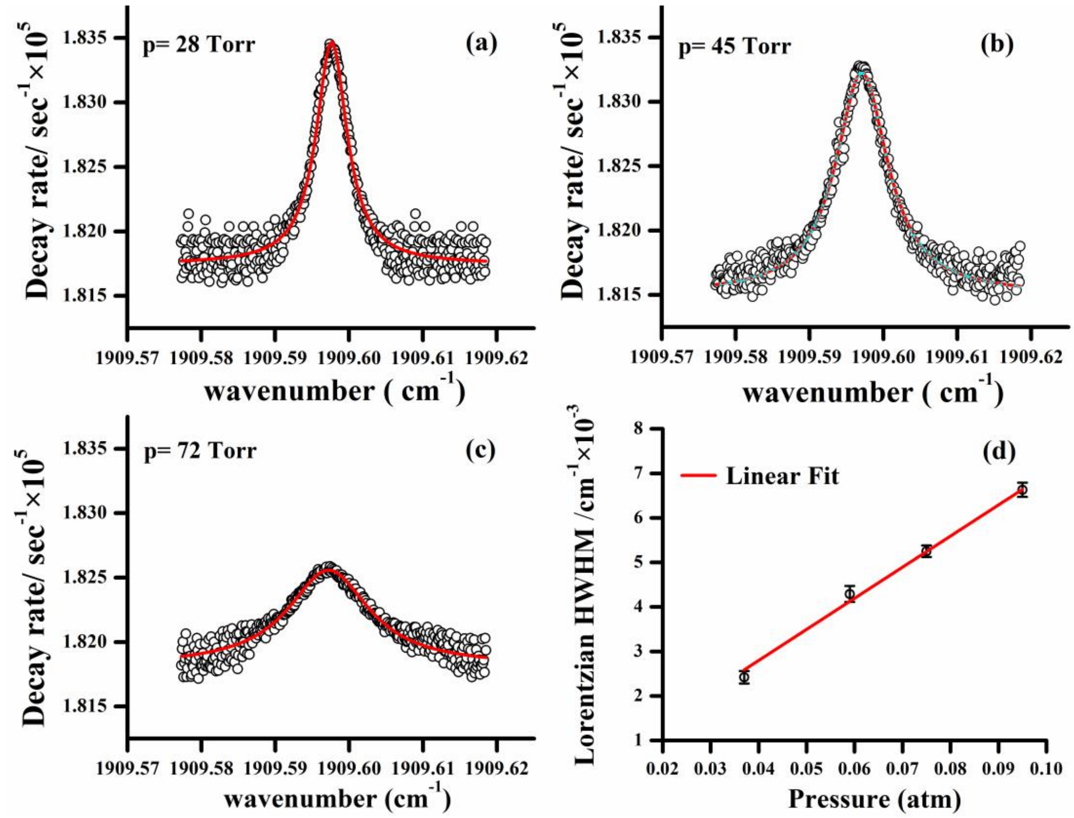

Figure 4.3 *(a), (b) and (c) Demonstrate the pressure bordering effects of the P(13e) rotational line of C_2H_2 to study the sensitivity of the CRD spectrometer at different pressures inside the cavity. The spectra were fitted with Gaussian, Lorentz and Voigt line-shape function wherever it was applicable. (b) Variation of HWHM at different pressures inside the cavity to determine the pressure broadening coefficient of C_2H_2 molecule at 1909.597cm^{-1}.*

The coefficient we determined from the CRDS measurements was in good agreement with the value reported in the HITRAN database of γ_{air} = 0.07 cm^{-1} atm^{-1}[24]. It is noteworthy to mention here that the high-resolution CRDS spectra should be recorded at low pressure to avoid the deleterious effects of pressure broadening on the absorption line. Moreover, using the present experimental set-up the detection limit of C_2H_2 would be 8.2 ppb on further broadening of the spectral line by an ambient pressure of 1 atm of air.

4.3.2 Evaluation of the set-up for multi-component chemical sensing

We next evaluated the performance of the widely tunable EC-QCL system for simultaneous monitoring of three environmentally and biomedically important molecular species i.e. NO, OCS and N_2O in a single laser scan within the MHF tuning range. We probed three rotationally resolved lines R(2.5f) of $^2\Pi_{3/2}$ of NO at 1887.636 cm^{-1}, P(10f) of (ν_1 + 2ν_2) of OCS at 1887.648 cm^{-1} and R(8e) of (ν_1 + ν_2) of N_2O at 1887.668 cm^{-1} for simultaneous measurement of the molecular species. The minimum detectable concentrations ($[X]_{min}$) 5.09×10^9 molecules/cm^3, 3.39×10^{10} molecules/cm^3 and 1.13×10^{11} molecules/cm^3 for NO, OCS and N_2O respectively, have been obtained from the present system. The HITRAN database[24] was used to simulate the high-resolution absorption spectra of these three gaseous species in presence of ~1% of water and ~400 ppm of CO_2 in the spectral region of 1887.625-1887.675 cm^{-1}. The simulation result is shown in figure 4.4 (a) which indicates no overlapping of the spectral lines with water and CO_2 in the spectral region mentioned above. A mixture of 200 ppbv of NO, 935 ppbv of OCS and 2 ppmv of N_2O with N_2 (Air Liquide, UK, 99.99%) was utilized to record this CRDS spectra at a pressure of 10 Torr inside the optical cavity. The experimentally observed high-resolution *cw*-CRDS spectra of the three neighbouring strong absorption lines of NO, OCS and N_2O in a narrow spectral range of ~ 0.05 cm^{-1} are depicted in figure 4.4(b)

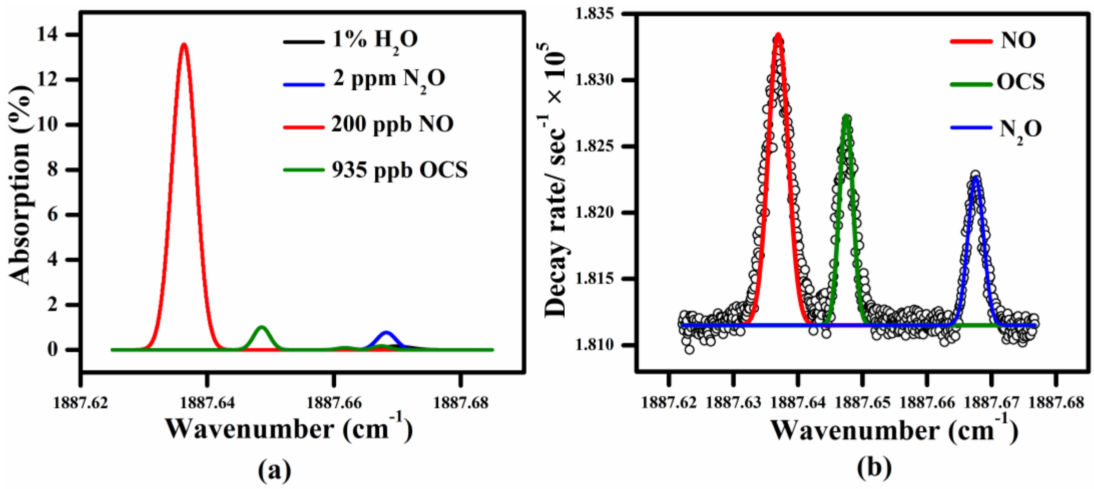

Figure 4.4. *(a) Indicates simulation results of high-resolution absorption spectra of three molecular species (200 ppb of NO, 935 ppb of OCS and 2 ppm of N_2O probing the R(2.5f) of $^2\Pi_{3/2}$, P(10f) of $(v_1 + 2v_2)$ and R(8e) of $(v_1 + v_2)$ ro-vibrational lines, respectively) in presence of 1% water vapour and 400 ppm of CO_2 in the tuning range of ~0.05 cm^{-1} ($1887.625cm^{-1}$-$1887.675cm^{-1}$) using HITRAN-2008 database. (b) Experimental cw-CRDS spectra of the same molecular species probing the same ro-vibrational lines at a pressure of 10 Torr inside the optical cavity, demonstrating the high sensitivity and unprecedented molecular selectivity of the current set-up within the same tuning range of the laser.*

The integrated areas' under the curve of each spectral line and their respective line integrated absorption cross-sections' were utilized to determine the concentrations of individual analytes which corresponds to $(6.38\pm0.02)\times10^{10}$ molecules/cm^3 of NO, $(3.06\pm0.05)\times10^{11}$ molecules/cm^3 of OCS and $(6.66\pm0.03)\times10^{11}$ molecules/cm3 of N_2O at 10 Torr pressure inside the optical cavity. The calculated concentrations match well with the simulation results. Additionally, if we allow further broadening of each spectral lines by an ambient pressure of 1 atm of air, the detection limits would then corresponds to the mixing ratios' of 200 ppt of NO, 1.37 ppb of OCS and 4.5 ppb of N_2O.

Moreover, the experimental observations of the line parameters, peak centre positions and integrated absorption cross-sections of all these molecular species investigated in the present study are summarized in Table-4.1. It shows an excellent agreement between the experimentally measured and database simulated results, thus confirming the high-resolution ro-vibronic spectroscopic capability of the new-generation EC-QCL-based CRDS detection method. The estimated detection limits were sufficient for direct monitoring of these molecular species in real atmospheric or human breath samples.

Table-4.1 Expeimentally observed line parameters of different molecules species

Molecular Species	Peak Centre (cm^{-1})	Line int. abs. cross-section ($cm^2mol^{-1}cm^{-1}$)	Doppler width (MHz) @ 296K
NO	1887.636	$(4.012\pm0.03)\times10^{-21}$	127.390
OCS	1887.647	$(4.282\pm0.02)\times10^{-22}$	90.031
N_2O	1887.667	$(1.494\pm0.03)\times10^{-22}$	105.186
C_2H_2	1909.597	$(1.1\pm0.01)\times10^{-22}$	138.344

4.3.3 Simultaneous detection of multiple trace species in exhaled breath and atmospheric sample

Figure (4.5 a, b, c) illustrates the examples of the representative cw-CRDS spectra of NO and OCS in human breath samples along with the individual CRDS spectrum of C_2H_2 and N_2O in atmospheric air samples. The integrated areas with the pressure-broadened or Doppler-broadened line profiles were used to calculate the concentrations of these molecular species in the relevant environments and the values were determined to be ~ 28 ppbv for NO, ~ 21 ppbv for OCS and ~ 403 ppbv for N_2O. The observed mixing ratios of NO and OCS lie in the typical range usually found in human breath samples[25-27]. Moreover, the N_2O mixing ratio we measured in air sample is also relevant to the typical value of N_2O concentrations in ambient air sample[19,28-30]. We also measured the C_2H_2 mixing ratios in ambient air sample collected from a highly polluted areas and it was found to be ~ 450 ppbv[31,32]. But the direct detection of C_2H_2 in pollution free atmosphere (which typically lies in 1-2 ppbv) is not suitable in this spectral region of the present QCL system as our estimated detection limit (which is 8.2 ppbv at 1 atm. pressure) is not quite enough for direct sensing of C_2H_2 in the troposphere. However, all these observations suggest the high-resolution capability of an EC-QCL-based CRDS sensor for multi-component chemical sensing applications with ultra-high sensitivity and unprecedented molecular selectivity. The combination of broadband wavelength coverage and high-resolution

MHF frequency tuning capability in this EC-QCL system with careful wavelength selection also eliminates the need for instrument calibration and consequently allows the simultaneous detection of either multiple trace species or a particular molecular species in a variety of environments such as in human breath or in ambient air without any spectral interference from other species such as H_2O and CO_2.

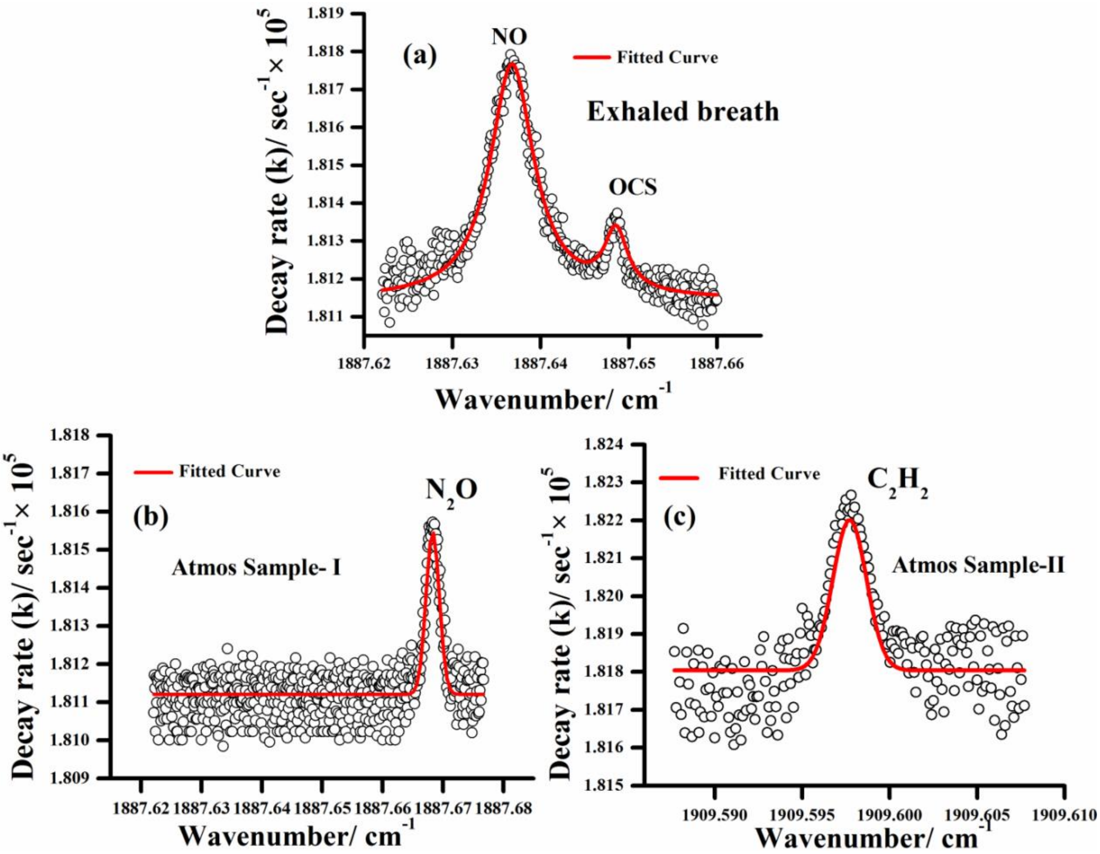

Figure 4.5. *(a) Illustrates cw-CRDS spectra of nitric oxide (NO) and carbonyl sulphide (OCS) in human exhaled breath at 1887.637 cm^{-1} and 1887.647 cm^{-1} at a pressure of 55 Torr inside the cavity. (b) Indicates typical cw-CRDS spectrum of nitrous oxide (N2O) in ambient air sample (Atmos sample-I). (c) Depicts CRDS spectrum of acetylene (C_2H_2) in a highly polluted atmospheric sample (Atmos sample-II).*

4.4 Conclusion:

In summary, we have demonstrated the application of a widely tunable room-temperature MHF frequency tuning EC-QCL-based CRDS detection method for quantitative and simultaneous detection of a unique panel of biomedically and environmentally important molecular species such as NO, OCS, N_2O and C_2H_2 with high sensitivity and unprecedented molecular selectivity[33]. The high specificity arises by recording rotationally resolved ro-vibronic transitions with well-defined central frequency in the mid-IR molecular fingerprint region within a narrow spectral range of the QC laser. However, the detection limit of the current EC-QCL-based CRDS sensor for simultaneous detection of the multiple species could be improved further by the enhancing the mirror reflectivity and reducing the detector noise. The full potential of the 5.2 μm EC-QCL-based high-resolution *cw*-CRDS sensor for in depth biomedical diagnostics by means of non-invasive breath test along with environmental sensing is yet to be investigated in the future but the merits of mid-IR EC-QCL technology for high-resolution molecular spectroscopy and multi-component chemical sensing are now established.

4.5 References

1. F.K. Tittel, D. Richter and A. Fried, *Solid-State Mid-Infrared Laser Sources*: *Topics Appl. Phys. Springer Berlin Heidelberg*, 2003, **89**, 445.

2. F.K. Tittel, R. Lewicki, R. Lascola *et al*., *Trace Analysis of Specialty and Electronic Gases: John Wiley & Sons, Inc., Hoboken, NJ, USA*. doi: 10.1002/9781118642771.ch4.

3. M.W. Sigrist, R. Bartlome, D. Marinov *et al*., *Appl. Phys. B*., 2008, **90**, 289.

4. J. Faist, F. Capasso, D.L. Sivco *et al*., *Science*, 1994, **264**, 553.

5. J.B. McManus, M.S. Zahniser and Jr D.D. Nelson, *Opt. Eng*., 2010, **49**, 111124.

6. R. Lewicki, A.A. Kosterev, D.M. Thomazy *et al*., *Proc. SPIE*., 2011, 7945 doi: 10.1117/12.874887.

7. B. Lee, E.C. Wood and M.S. Zahniser *et al*., *Appl. Phys. B*., 2011, **102**, 417.

8. G. Wysocki, R. Lewicki, R.F. Curl *et al*., *Appl. Phys. B*., 2008, **92**, 305.

9. A. De, G.D. Banik, A. Maity *et al*., *Opt. Lett*., 2016, **41**, 1949.

10. Y.A. Bakhirkin and A.A. Kosterev, C. Roller *et al*., *Appl. Opt*., 2004, **43**, 2257.

11. A.A. Kosterev, A.L. Malinovsky, F.K. Tittel *et al*., *Appl. Opt*.,2001, 40, 5522.

12. G.N. Rao, and A. Karpf, *Appl. Opt*., 2011, 50, 1915.

13. F.M. Schmidt, O. Vaittinen, M. Metsälä *et al*., *Appl. Phys. B*, 2010, **101**, 671.

14. T.G. Spence, C.C. Harb, B.A. Paldus *et al*., *Rev. Sci. Instrum*., 2000, **71,** 347.

15. W. Cao and Y. Duan., *Clin. Chem*., 2006, **52**, 800.

16. J. Wojtas, *Sensors*, 2015, **15**, 14356.

17. G. Wysocki, M. McCurdy, S. So *et al*., *Appl. Opt*., 2004, **43**, 6040.

18. M. Pradhan, M.S.I. Aziz, R. Grilli *et al*., *Environ. Sci. Technol*., 2008, **42**, 7354.

19. G. D. Banik, S Som, A. Maity *et al*., *Anal. Methods*., 2017, **9**, 2315.

20. D.J. Hamilton and A.J. Orr-Ewing, *Appl. Phys. B*, 2011 **102**, 879.

21. S. Kang, S. Kim, S. Kang *et al*., *Sensors*, 2014, **14**, 14399.

22. M. Pradhan, R.E. Lindley, R. Grilli *et al*., *Appl. Phys*. B, 2008, **90**, 1-9.

23. M. Jahjah, W. Ren, P. Stefanski *et al*., *The Analyst*, 2014, **139**, 2065.

24. L.S. Rothmana, I.E. Gordona, A. Barbe *et al*., *J. Quant. Spectrosc. Radiat. Transf*., 2009, **110**, 533.

25. T.L. Mathew, P. Pownraj, S. Abdulla *et al*., *Diagnostics*, 2015, **5**, 27.

26. C. Wang and P. Sahay, *Sensors*, 2009, **9**, 8230.

27. C. Lourenco and C. Turner, *Metabolites*, 2014, **4**, 465.

28. A.J. Thomson, G. Giannopoulos, J. Pretty *et al*., *Phil. Trans. R. Soc. B*, 2012, 367, 1157.

29. F.M. Couto, M.S. Sthel, M.P.P. Castro *et al*., *Appl. Phys*. B, 2014, **117**, 897.

30. A. Hensen, U. Skiba and D. Famulari, *Environ. Res. Lett*., 2013, 8, 025022.

31. J. Nassar and J. Goldbach, *Intern. J. Environ. Anal. Chem*., 1979, 6, 145.

32. A. Roy, A. Upadhyay and A.L. Chakraborty, *Proc. SPIE,* 2016, 9876.

5 Investigation of *l*-type doubling of hot bands in Δ vibrational states of OCS near 5.2 μm using cavity ring-down spectroscopy

Contents

5.1 Introduction

It is well known that each bending or perpendicular mode of vibration in a non-rotating linear polyatomic molecule is doubly degenerate. But molecular rotation introduces a new phenomenon known as *l*-type doubling, *l* being the quantum number of angular momentum so that the vibration-rotation interaction induces the splitting of the degenerate energy levels. Several decades ago, Herzberg[1] first introduced the concept of *l*-type doubling and suggested that this splitting is caused by a Coriolis-type interaction between one component of a doubly degenerate bending mode and stretching vibrations of the molecule. Subsequently, the existence of *l*-type doubling transitions was theoretically demonstrated by Neilsen and Shaffer[2] and pointed out the importance of this effect for better understanding of polyatomic molecular properties from spectroscopic data. In addition, accurate measurements of *l*-type doubling

transitions can provide a variety of information about the bending mode of linear molecules with rotational constants, centrifugal distortion constants and Coriolis interaction. However, the effect of *l*-type doubling is usually significant only in the first excited state i.e. where $v_1 = v_3 = 0$, $v_2 = 1$, $l_2 = \pm1$ (v_i = vibrational quantum number). For *l*=2 (i.e. Δ states) or greater, the *l*-type splittings are extremely small to be measured and usually observed for relatively high rotational states[3,4].
However, there have been considerable interests over the last several decades to measure the *l*-type doubling transitions in carbonyl sulfide (OCS) because it is an important molecule of astrophysical interest[5] and also the second most abundant sulphur-containing species in the atmosphere of Venus[6]. The high-resolution spectroscopic detections of individual ro-vibrational transitions of OCS which could be attributed to the weaker hot bands with *l*-type doubling are important for the studies of terrestrial and planetary atmospheres[7]. Moreover, a good understanding of spectral line parameters such as *l*-type doubling constant and transition dipole moments, determined from experimental analysis would help us to analyze the astrophysical observations with absorption bands of minor constituents.

OCS is known to be a linear triatomic molecule which has three fundamental vibrations ν_1, ν_2, and ν_3 located at 858, 520 and 2062 cm^{-1}, respectively in which ν_1 and ν_3 are the stretching vibrations and ν_2 is the bending vibration which exhibits the *l*-type doubling. However, early studies were primarily focused on the microwave and infrared measurements of *l*-type doubling transitions in OCS for *l*=0 and *l*=1 vibrational states[8]. For instance, using a Spin-Flip Raman Laser, Buckly *et al.*[9] reported the *l*-type doubling in the hot bands of OCS for *l* =1 state near 1890 cm^{-1}. In another study, the existence of *l*-type doubling in OCS was also recorded using the molecular beam electric resonance spectroscopy in low J states of the (02^20) vibrational state of $^{16}O^{12}C^{32}S$[3,10]. In view of the earlier studies[11,12] however, the high-resolution spectroscopic measurements of *l*-type doubling transitions in the weak hot bands for higher values of *l* i.e. *l*=2 or Δ vibrational state are very limited and to our knowledge, it has never been explored before to record the *l*-type splittings involving the parity doublet *e* and *f* sub-states arising from weak hot band transitions. But, the recent technological innovations[13,14] of the mid-IR continuous-wave (*cw*) external-cavity quantum cascade lasers (EC-QCLs) with extremely narrow linewidth (~0.0001 cm^{-1}) and mode-hop-free (MHF) tuning capability in a wide range of frequency when combined with highly-sensitive cavity-enhanced absorption techniques such as cavity ring-down spectroscopy (CRDS)[15] opens the possibility of exploiting this high-resolution spectroscopy to measure the *l*-type doubling transitions in weak hot bands for OCS. We note that the observation of such *l*-doublet splittings between e and f sub-levels of OCS in high J states has not previously been reported.

In this chapter, we investigate the observation of *l*-type doubling in R branch of $^{16}O^{12}C^{32}S$ in $(14^20) \leftarrow (02^20)$ hot band ro-vibronic transitions using an EC-QCL based high-resolution cw-CRDS technique in the region of 1900-1904 cm^{-1}. The line strengths of the e and f sub-states for J=22 to J=29 rotational lines were measured by probing the respective absorption lines. Moreover, the *l*-doublet splittings were utilized to determine the vibrational transition dipole moments, rotational constants, centrifugal distortion constants and *l*-type doubling constant for both e and f components in Δ vibrational state (*l*=2) of OCS. Finally, we extended the current high-resolution *cw*-CRDS method to measure other two primary isotopologues of OCS, i.e. $O^{16}C^{12}S^{34}$ and $O^{16}C^{12}S^{33}$ in pure OCS gas sample. We conducted this measurement as a feasibility study in the $(14^20) \leftarrow (02^20)$ weak hot band transition for the respective isotopic species in the OCS gas samples under investigation by probing the R(35) and R(50) absorption lines, respectively.

5.2 Experimental Technique

As mentioned above, high-resolution measurements of l-doublet splittings of OCS were made using the *cw*-CRDS method coupled with an EC-QCL operating at λ~5.2 μm (1923 cm^{-1}). The experimental arrangement of the *cw*-CRDS system has been described in chapters 3 and 4 in details. Therefore only salient features of the spectrometer are given here. In a classical *cw*-CRDS system, the decay rate of a laser light trapped in a high-finesse optical cavity is measured and the direct absorption of molecular spectral lines is recorded. The number density of a molecular species is calculated in an absolute scale from the knowledge of the molecular absorption cross-section without the need for secondary calibration standards. Additionally, as CRDS measurements are carried out in the time-domain and thus it is insensitive to laser intensity fluctuations. The minimum detectable change in the absorption coefficient, α_{min} is typically < 10^{-9} cm^{-1} and the effective optical path length that is easily achieved is of the order of few kilometres in a small cavity volume. For the described high-resolution CRDS measurements, the probe was an EC-QCL with a fine MHF tuning range of 1847-1965 cm^{-1}, an output power of >80 mW over this range and a linewidth of ~ 0.0001 cm^{-1}. The resulting short-time noise equivalent absorption (NEA) coefficient, which is given by $\sqrt{2}\, \alpha_{min}\, f^{-1/2}_{acq}$ where f_{acq} is the data acquisition rate, was ~ 7.16×10^{-10} cm^{-1} $Hz^{-1/2}$ for f_{acq} = 90 Hz and αmin was determined to be 5×10^{-9} cm^{-1} based on the typical empty cavity ring-down time (RDT) of τ_0 = 5.64 µs and standard deviation (1σ) of 0.08% with averaging of 6 RDT determinations. Cavity mirrors with reflectivity of 99.98% at 5.2 µm were used in the *cw*-CRDS system, corresponding to finesse (F) of ~ 15700. Additionally, the linewidth of the EC-QCL ($\Delta\nu_{QCL}$) was determined to be ~ 18 MHz (0.0006 cm^{-1}), matching the manufacturer specified value of 0.0003 MHz with the EC-QCL. The linewidth of the TEM_{00} cavity modes was also measured to be $\Delta\nu_{Cavity}$= (FSR/F) ≈ 19 kHz, where the cavity's free spectral range (FSR) was 300 MHz. However, the high-resolution Doppler-limited cw-CRDS spectra involving rotationally resolved *l*-type splittings were acquired over the R branch of $(14^20) \leftarrow (02^20)$ hot band transition of OCS by fine tuning over ~ 0.1 cm^{-1} of the piezoelectric transducer (PZT) attached to the tunable diffraction grating of the EC-QCL system.

5.3 Results and Discussion

The performance of the *cw*-CRDS system was initially assessed by injecting a certified calibration gas mixture of 31±0.2 ppm of OCS in N_2 inside the optical cavity with a pressure of 5 Torr. Figure 5.1 shows an example of high-resolution spectrum of OCS, probing the R(24) rotational line of the $(14^20) \leftarrow (02^20)$ hot band transition at 1900.255 cm^{-1} with a line-strength of σ_{line}= 9.59×10^{-23} cm^2 $molecule^{-1}$ cm^{-1} at 296 K, as given by the HITRAN database[16].

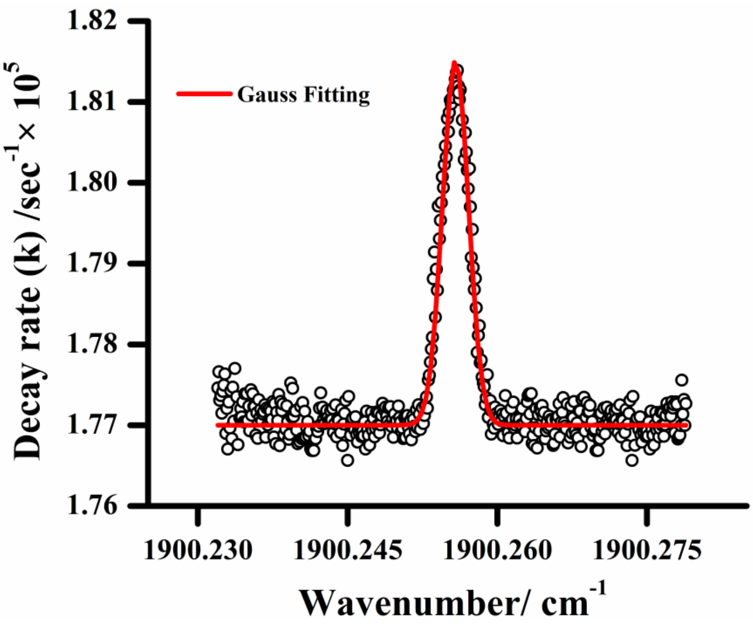

Figure 5.1 *CRDS spectrum of R(24) rotational line of OCS with peak centre at 1900.255 cm^{-1}*

The spectrum was fitted with a Gaussian line-shape profile with FWHM of 0.00306 cm^{-1} which corresponds to the expected Doppler broadening at the measured wavelength. The integrated area under the curve was utilized to measure the concentration of the sample inside the cavity and it was measured to be $[X]_{OCS}$= (5.1 ± 0.02) $\times 10^{12}$ molecules cm^{-3}. As mentioned later, the same sample inside the cavity was used to determine the vibrational transition dipole moments for *e* and *f* sub-states of the $(14^20) \leftarrow (02^20)$ ro-vibrational transition for *l*=2 state. However, we first focused on the measurement of the *l*-type doubling constant of (14^20) vibrational state. To accomplish this, we then probed 8 rotationally resolved *l*-type doublet transitions for OCS from J=22 to J=29. The examples of the rotationally resolved *l*-doublet splittings between *e* and *f* components of the corresponding rotational lines for Δ vibrational state are depicted in figure 5.2.

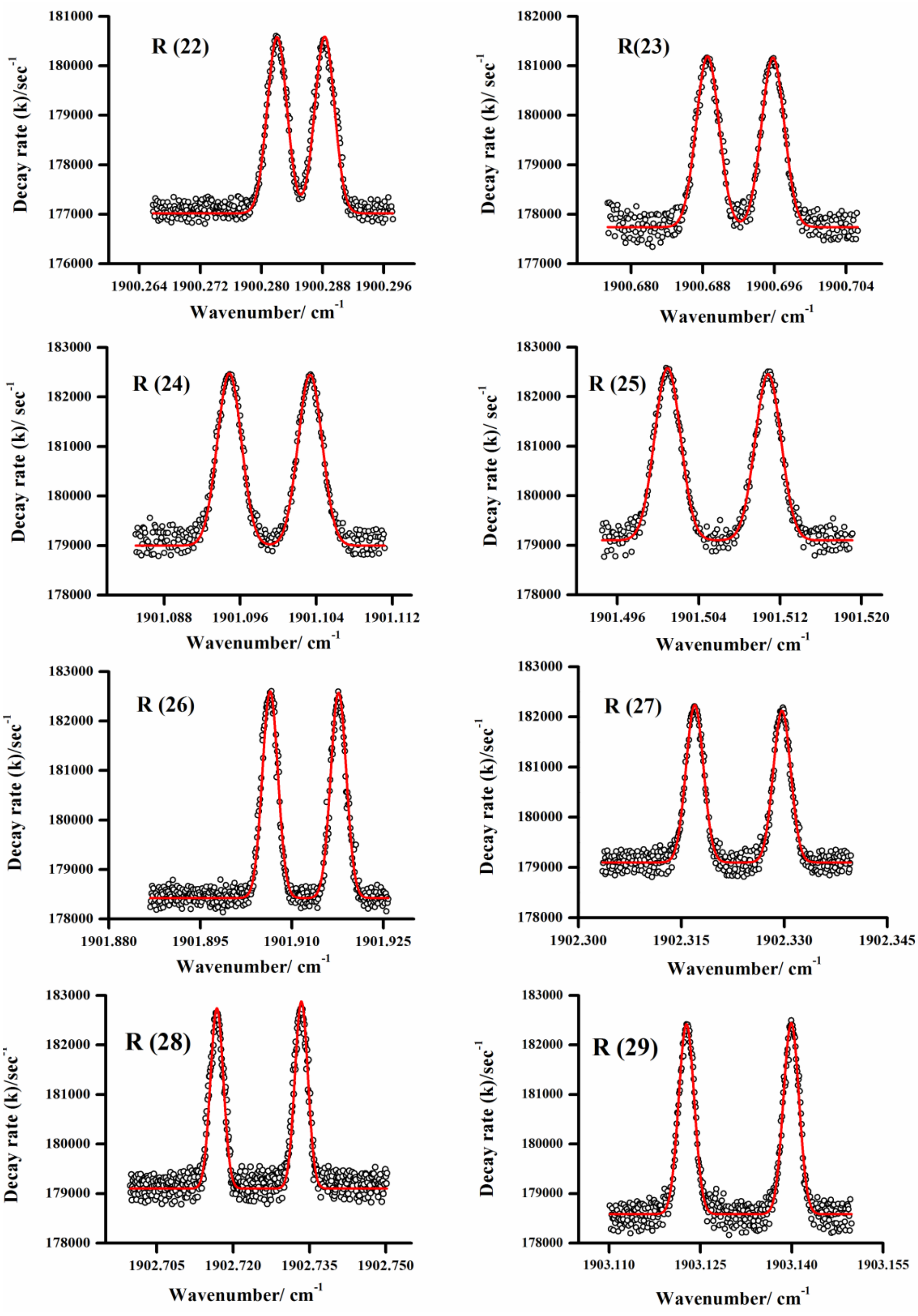

Figure 5.2 *CRDS spectra of l-type doubling in R branch probing J=22 to J=29 rotational lines of the* $(14^20) \leftarrow (02^20)$ *hot band transitions.*

It was observed that the splitting between the *e* and *f* sub-states increases with increasing J value and subsequently the *l*-type doubling constant was calculated. According to Nielsen's theory[17] the splittings in the rotational levels due to interaction between rotation and vibration are given by

$$\Delta E = hqJ(J+1) \tag{5.1}$$

where is the separation between the rotational energy levels, q is splitting constant, h is Planck's constant and J is the rotational quantum number.

For J → J+1 transition, the doublet splitting is given by:

$$\Delta \nu = 2q(J+1) \tag{5.2}$$

The variation of ($\Delta\nu$) with (J+1) is shown in figure 6.3 and the slope of the straight line provides the *l*-type doubling constant[18,19]. In our present study, the *l*-type doubling constant for (14^20) vibrational state was found to be 1.2×10^{-5} cm^{-1} which is ~20 times smaller than the value of the *l*-type doubling constant for *l* =1 state of OCS.

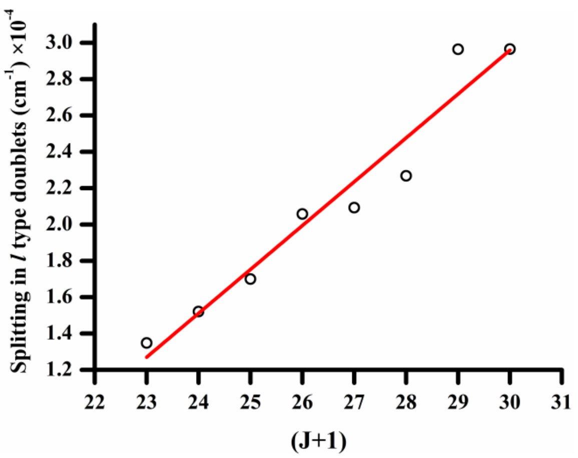

Figure 5.3 *Measurement of l-type doubling constant in l = 2 state probing J=22 to J=29 rotational lines of R branch in (14^20) ← (02^20) hot band transitions***.**

We next investigated the vibrational transition dipole moment and in order to do that, we first estimated the line strengths or line intensities of the individual ro-vibrational transition of the probed absorption lines. The integrated areas under the curves as depicted in figure 5.2 were then utilized to estimate the line strength of the individual ro-vibrational transition. The individual absolute line intensity, S_{if} can be expressed as[20-22]

$$S_{if} = \left(\frac{8\pi^3}{3hc}\right)\frac{T_0}{TZ_v Z_R}\nu N_i S_v S_R \mu_v{}^2 F \exp\left(-\frac{E''}{KT}\right)\left[1-\exp\left(-\frac{hc\nu}{KT}\right)\right] \tag{5.3}$$

where, T is the temperature in Kelvins, T_0=273.15 K, ν is the wavenumber of the line centre at cm^{-1}, E'' is the energy of the lower state and K is Boltzmann constant. For Δl=0, the Hönl-London factor, SR is given by $S_R = \frac{m^2 - l^2}{|m|}$, where m = J''+1 for R branch and m = -J'' for P branch. μ_v is the vibrational transition dipole moment and F is the Herman-Wallis factor that accounts for the vibration-rotation interaction in non-rigid rotator. S_v is the vibrational intensity factor for the triatomic molecule; Z_v and Z_R are the vibrational and rotational partition functions, respectively.

For a linear molecule, F may be expressed as a function of m by[20]

$$F(m)= 1+\alpha m+\beta m^2+\ldots, \tag{5.4}$$

which may be approximated as F(m)= 1+ αm; where α is a dimensionless constant

The vibrational partition function, Z_v has been calculated from:

$$Z_v = \prod_{s=1}^{3}\left[1-\exp\left(-\frac{hc\omega_s}{KT}\right)\right]^{-g_s} \tag{5.5}$$

The rotational partition function, Z_R for a level ν is given by:

$$Z_R = \sum_J (2J+1)e^{-\left[B_v J(J+1) - D_v J^2 (J+1)^2\right]/KT} \tag{5.6}$$

where, B_v and D_v are the rotational constant and centrifugal distortion constant, respectively. Since the contribution to S_v is different for non-degenerate and degenerate vibrational mode, hence S_v can be written as the product of two terms, i.e. L_{13} for non-degenerate modes of vibration (ν_1 and ν_3) and L_2 for the degenerate vibrational mode (ν_2).

$$\text{Thus, } S_v = L_{13}\, L_2 \tag{5.7}$$

where, $L_{13} = \frac{(v_1+\Delta v_1)!(v_3+\Delta v_3)!}{(v_1! v_3! \Delta v_1! \Delta v_3!)}$ with both ν_1 and ν_3 are the vibrational quantum numbers of the lower state. $\Delta\nu_1$ and $\Delta\nu_3$ are the differences of the corresponding vibrational quantum numbers of higher and lower state.

and $$L_2 = \frac{\left[\frac{1}{2}(v_2 + l + \Delta v_2)\right]!\left[\frac{1}{2}(v_2 - l + \Delta v_2)\right]!}{\left\{\left[\frac{1}{2}(v_2 + l)\right]!\left[\frac{1}{2}(v_2 - l)\right]!\left[\frac{1}{2}(\Delta v_2)\right]!^2\right\}}$$

The product of the Herman-Wallis factor (F) and the vibrational transition dipole moment (μ_v) were determined via experimental S_{if} values of the recorded spectra of OCS. Equation (5.3) can now be re-written as follows:

$$\mu_v^2 F = \frac{S_{if}}{\left(\frac{8\pi^3}{3hc}\right)\frac{T_0}{TZ_v Z_R}\nu N_i S_v S_R \exp\left(-\frac{E''}{KT}\right)\left[1 - \exp\left(-\frac{hc\nu}{KT}\right)\right]} \tag{5.8}$$

A plot of right-hand side of equation (5.8) as a function of m yields a curve whose intercept at the origin is the transition diploe moment squared and the slope is proportional to the Herman-Wallis constant, α. The values of B_v and D_v for the lower state i.e. (02^20) of the recoded transitions are shown in Table-5.1 and the values were taken from the microwave data[5,10]. However, neglecting the D_v values, Z_R can be represented as follows:

$$Z_R = \frac{KT}{B_v} \tag{5.9}$$

Table-5.1 *represents the main molecular constant for the lower levels of the measured transitions*

	B_v/ cm^{-1}	D_v/ cm^{-1}	Z_R at 296 K
02^20 *e*	0.20536	5.13×10^{-8}	1000.4991
02^20 *f*	0.20299	4.503×10^{-8}	1012.1804

In our present calculation, the vibrational partition function, Z_v was found to be 1.1987 at 296 K. Using equation (5.7), we obtained S_v=3 for both *e* and *f* sub-states of the (14^20) ← (02^20) hot band transition[21] and consequently, we determined the Sif values for e and f components probing the J=22 to J=29 rotational lines of R branch. The observed line strengths of the probed rotational lines of the measured transitions are shown in Table-5.2. The S_{if} values shown here are in the order of 10^{-23} cm^2 mol^{-1} cm^{-1}.

Table-5.2 depicts the comparison between S_{if} values ($\times10^{-23}$) for R branch of (14^20) ← (02^20) hot band transition of OCS.

J	S_{if} (observed)	S_{if} (calculated)	Obs-Calc
22e	7.528	7.381	0.147
22f	7.528	7.381	0.147
23e	7.167	7.381	-0.214
23f	7.167	7.381	-0.214
24e	7.226	7.341	-0.115
24f	7.226	7.341	-0.115
25e	7.023	7.260	-0.237
25f	7.023	7.260	-0.237
26e	8.741	7.179	1.562
26f	8.741	7.179	1.562
27e	6.570	7.058	-0.488
27f	6.570	7.058	-0.488
28e	7.626	6.937	0.689
28f	7.626	6.937	0.689
29e	8.059	6.776	1.280
29f	8.059	6.776	1.280

Subsequently, $\mu_v{}^2F$ values have been evaluated for both e and f sub-states of (14^20) vibrational state using equation (5.8). The plots of $\mu_v{}^2F$ vs. m for *e* and *f* sub-states are shown in figure 5.4(a) and (b).

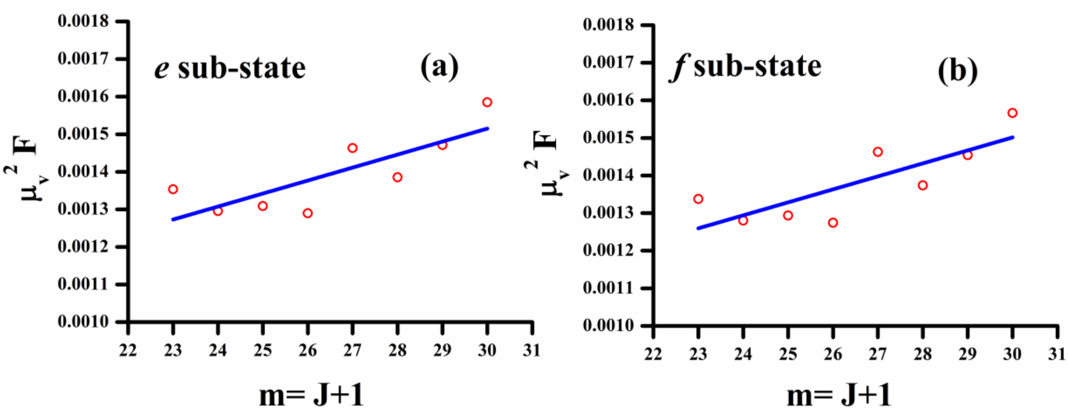

Figure 5.4 $\mu_v{}^2F$ *is plotted as a function of m (=J+1) to measure the vibrational dipole moments for e and f sub-states of the (14^20) vibrational state.*

The values of vibrational dipole moments (μ_v) and Herman-Wallis constants (α) have been mentioned in Table 5.3 for *e* and *f* sub-states of the (14^20) ← (02^20) hot band transition. As expected, the difference between the μ_v values for *e* and *f* sub-states of

Table 5.3 shows the vibrational dipole moments and Herman-Wallis constant for e and f sub-states for $(14^20) \leftarrow (02^20)$ hot band transition.

	μ_v/ Debye	α
$(14^20)^e \leftarrow (02^20)^e$	2.18×10^{-2}	0.072
$(14^20)^f \leftarrow (02^20)^f$	2.15×10^{-2}	0.074

the measured transition is very small but the observed μ_v values for both the *e* and *f* components were found to be ~2-3 times smaller than the values of the hot band transitions for l=1 state of OCS[22]. However it is noteworthy to mention here that the observed μ_v values are extremely higher (~30 times) than the values of the isotopic hydrogen cyanide ($H^{12}C^{14}N$) for the same vibrational transition in l = 2 state[21].

Additionally, we have made an attempt to measure the rotational constant, centrifugal distortion constant and band centres of *e* and *f* sub-components of the (14^20) vibrational level in l=2 state by the least square analysis method. For that purpose, we have monitored the l-type doublet transition frequencies of e and f components of the probed rotational lines belonging to the $(14^20) \leftarrow (02^20)$ hot band transition. Consequently, the transition frequencies were fitted with the following equation (5.10)[9]

$$\nu = \nu_0 + B_{v'}\,[J'(J'+1)-l^2] - D_{v'}\,[J'(J'+1)-l^2] - B_{v''}\,[J''(J''+1)-l^2] + D_{v''}\,[J''(J''+1)-l^2] \quad (5.10)$$

where, $B_{v'}$, $B_{v''}$ are the rotational constants at higher and lower energy states; $D_{v'}$, $D_{v''}$ are the centrifugal distortion constants at higher and lower energy states, and ν0 is the transition center of the selected hot band. The values of for e and f sub-states are 6102.558 MHz and 6102.560 MHz, respectively whereas, the values for *e* and *f* sub-states were found to be 1.54 KHz and 1.35 KHz, respectively[23,24]. All the $B_{v''}$ and $D_{v''}$ values of the lower energy state were taken from microwave data of OCS and the least square analysis was performed with ν_0, $B_{v'}$, $D_{v'}$ as variables. Table-5.4 lists the observed and calculated values of transition frequencies of J=22 to J=31 rotational lines of the $(14^20) \leftarrow (02^20)$ hot band transition in R branches of OCS in l=2 state.

Table-5.3 shows the least square fit of e and f sub-states of $(14^20) \leftarrow (02^20)$ transition of OCS

		$(14^20)^e \leftarrow (02^20)^e$			$(14^20)^f \leftarrow (02^20)^f$		
J'	J"	Obs.	Cal	Obs.-Cal.	Obs.	Cal	Obs.-Cal.
23	22	1900.2820	1900.2803	0.0017	1900.2882	1900.2870	0.0012
24	23	1900.6885	1900.6872	0.0013	1900.6958	1900.6946	0.0012
25	24	1901.0949	1901.0939	0.001	1901.1034	1901.1022	0.0012
26	25	1901.5001	1901.5002	-0.0001	1901.5108	1901.5097	0.0011
27	26	1901.9064	1901.9060	0.0004	1901.9177	1901.9172	0.0005
28	27	1902.3169	1902.3115	0.0054	1902.3297	1902.3246	0.0051
29	28	1902.7168	1902.7165	0.0003	1902.7334	1902.7319	0.0015
30	29	1903.1227	1903.1211	0.0016	1903.1399	1903.1392	0.0007
31	30	1903.5278	1903.5244	0.0034	1903.5475	1903.5520	-0.0045
32	31	1903.9307	1903.9280	0.0026	1903.9565	1903.9596	-0.0031

The $B_{v'}^{\,e}$ and $B_{v'}^{\,f}$ values for the (14^20) vibrational state were found to be 6159.9 ± 19 MHz and 6091.5 ± 17 MHz, respectively which are consistent with and of comparable accuracy to the microwave values of 6150 ± 12 MHz and 6099 ± 18 MHz[25]. Our centrifugal distortion constants, $D_{v'}^{\,e}$ = 2.6 ± 0.9 and $D_{v'}^{\,f}$ = 1.8 ± 0.84 kHz, are new values, and can be compared with estimates from the force field of 2.57 and 1.89 kHz[23]. Subsequently, we have also calculated the centrifugal distortion energy (E_v^{cent}) for the $(14^20)^e$ and $(14^20)^f$ vibrational states and plotted with J values. The E_v^{cent} for a particular vibrational state can be expressed as[11]

$$E_v^{cent} = -D_v\,[J^2(J+1)^2 - l^2] \tag{5.11}$$

where $D_v = D_e + \sum_i \beta_i \left(v_i + \frac{d_i}{2} \right)$ (5.12)

Here, β_i's are the constants and their values were found to be $\beta_1 = 0.028\times10^{-8}$ cm^{-1}, $\beta_2 = 0.057\times10^{-8}$ cm^{-1} and $\beta_3 = -0.038\times10^{-8}$ cm^{-1} [11], d_i indicates the degeneracies in the mode of vibrations and here $d_1 = d_3 = 1$ and $d_2 = 2$ have been considered to measure the D_e values for *e* and *f* components of the selected transition. However, it was observed that centrifugal energy decreases with increase in J values as shown in figure. 5.5. The decrease in centrifugal energy for the e sub-state was more rapid than the f sub-state in the (14^20) vibrational state.

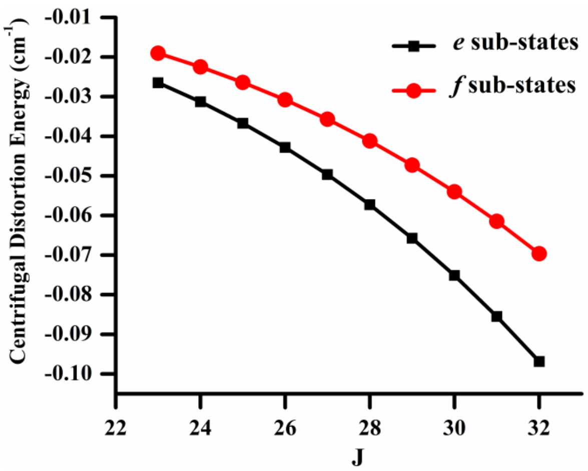

Figure 5.5 *Variation of centrifugal distortion energies for e and f sub-states for the (14^20) vibrational state with rotational quantum number (J).*

Using equation (5.12), the calculated values of D_e for *e* and *f* components were found to be 8.379×10^{-8} cm^{-1} and 5.937×10^{-8} cm^{-1}, respectively for the (14^20) vibrational state. Furthermore, we also calculated the equilibrium value of B_e for the *e* and *f* components for the same vibrational state using the following equation

$$B_v = B_e + \sum_i \alpha_i \left(v_i + \frac{d_i}{2} \right) \tag{5.13}$$

Here, α_i's are the constants and their values were found to be $\alpha_1 = 6.833\times10^{-4}$ cm^{-1}, $\alpha_2 = -3.53\times10^{-4}$ cm^{-1} and $\alpha_3 = 1.21\times10^{-3}$ cm^{-1} [4] and the calculated B_e values were found to be 0.2052 cm^{-1} and 0.2029 cm^{-1}, respectively for the *e* and *f* components of the (14^20) vibrational state.

Finally, we extended our work to check the feasibility of measuring the natural abundances of two other isotopic species of OCS i.e. $O^{16}C^{12}S^{34}$ and $O^{16}C^{12}S^{33}$ in the gas sample being used in the present study by the high-resolution EC-QCL based *cw*-CRDS method. To do this, we probed R(50) and R(35) rotational lines centred at 1900.123 cm^{-1} and 1900.322 cm^{-1}, respectively in the (12^00)←(00^00) transition and subsequently measured the isotope ratios. The minimum detection limits for

$O^{16}C^{12}S^{34}$ and $O^{16}C^{12}S^{33}$ were estimated to be 2.63×10^{11} molecules/cm^3 and 5.66×10^{11} molecules/cm^3, respectively using the line-strengths of 5.8×10^{-23} cm^2 mol^{-1} cm^{-1} and 2.5×10^{-23} cm^2 mol^{-1} cm^{-1} at 296 K mentioned in the HITRAN database[16]. Figure 5.6 indicates a plot of $O^{16}C^{12}S^{32}$ vs $O^{16}C^{12}S^{34}$ concentration with a typical spectrum of $O^{16}C^{12}S^{34}$ in the inset. The gradient of the straight line denotes the isotopologue ratio of $O^{16}C^{12}S^{34}$/ $O^{16}C^{12}S^{32}$ = 4.14 ± 0.02% which is very close to the reported HITRAN value of the natural abundance of 4.15%[16]

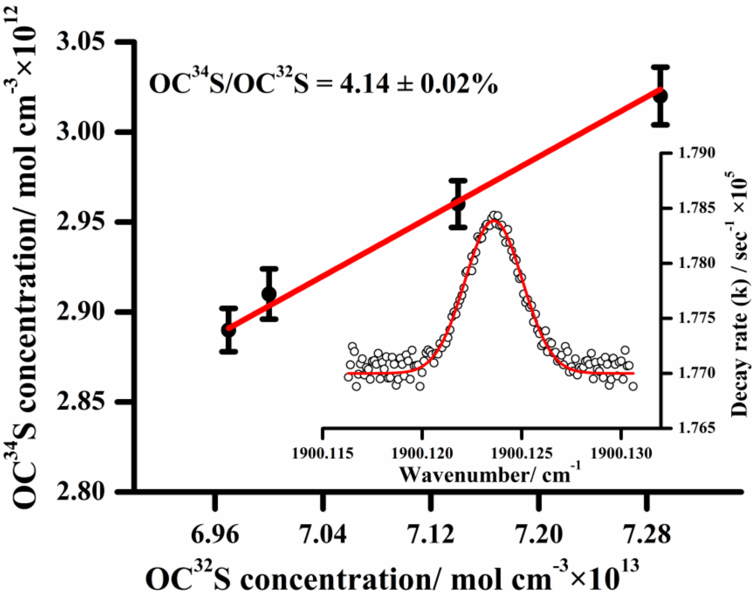

Figure 5.6. *Measurement of natural abundance of $^{16}O^{12}C^{34}S$ isotopic species in OCS gas sample under investigation. The inset figure shows the typical absorption spectrum of $^{16}O^{12}C^{34}S$ isotope in the sample gas probing the R(50) rotational line at 1900.123 cm^{-1}.*

Figure 5.7 represents a similar type of plot for the $O^{16}C^{12}S^{32}$ vs $O^{16}C^{12}S^{33}$ concentration with a representative spectrum of $O^{16}C^{12}S^{33}$ in the inset. From the gradient, we obtained the isotopologue ratio of $^{16}O^{12}C^{33}S/^{16}O^{12}C^{32}S$ = 0.739 ± 0.03% which is also a good agreement with the natural abundance of 0.74% as mentioned in the HITRAN database[16]. In view of these results, the present *cw*-CRDS method also enabled us to measure the natural isotopic abundances of the different isotopologues of OCS gas sample used in the current investigation.

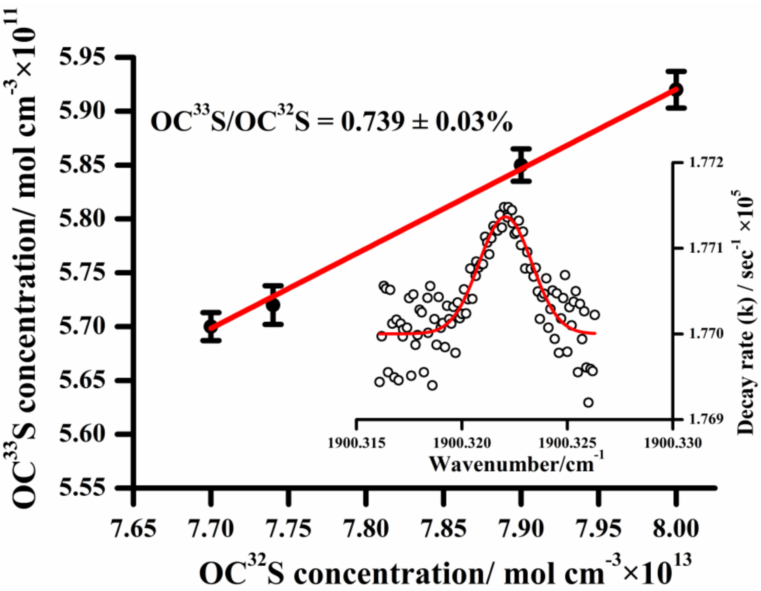

Figure 5.7. *Measurement of natural abundance of $^{16}O^{12}C^{33}S$ isotopic species in OCS gas sample used in the present study. The inset shows the typical absorption spectrum of $^{16}O^{12}C^{33}S$ isotope probing the R(35) rotational line at 1900.322 cm^{-1}.*

5.4 Conclusions

In summary, we have employed the EC-QCL based high-resolution *cw*-CRDS technique for the measurement of *l*-type doubling in the $(14^20)\leftarrow(02^20)$ weak hot band transition of OCS for l =2 state. We have measured the *l*-type doubling constant in R branch of the selected hot band transition for the higher values of J and subsequently determined several spectroscopic parameters such as vibrational transition dipole moments, rotational constants, centrifugal distortion constants for e and f sub-levels and *l*-type doubling constant in Δ vibrational state (l=2) of OCS. As the *l*-doublet splittings in the weak hot band transition $(14^20)\leftarrow(02^20)$ of OCS for l=2 state were not recorded before, therefore our new experimental data involving several spectroscopic parameters will be useful for better fundamental understanding of linear triatomic molecular properties and hyperfine structures of their isotopologues.

5.5 References

1. G. Herzberg, *Rev. Mod. Phys*., 1942, **14**, 219.

2. H. H. Nielsen and W. H. Shaffer, *J. Chem. Phys*., 1943, **11**, 140.

3. B. Fabricant and J. S. Muenter , *J. Mol. Spectrosc*., 1974, **53**, 57.

4. C. H. Townes and A. L. Schalow, 1975, *Microwave Spectroscopy : Dover Publications, Inc., Newyork.*

5. A. G. Maki, *J. Phys. Chem. Ref. Data*,, 1974, **3**, 221.

6. K. Sung, R. A. Toth, L. R. Brown *et al*., *Quant. Spectrosc. Radiat. Transf*., 2009, **110**, 2082.

7. J. V. Auwera and A. Fayt, *J. Mol. Struct*., 2006, **780**, 134.

8. A. G. Maki and D. R. Johnson, *J. Mol. Spectrosc*., 1973, **47**, 226.

9. P. G. Buckley, J. H. Carpenter, A. McNeish *et al*., *J. Chem. Soc., Faraday Trans. 2*, 1978, **74**, 129.

10. Y. Morino and C. Matsumura, *Bull. Chem. Soc. Jpn*., 1967, **40**, 1095.

11. T. Nakagawa and Y. Morino, *J. Mol. Spectrosc*.,1969, **31**, 208.

12. A. G. Maki, Jr. and D. R. Lide, Jr., *J. Chem. Phys*., 1967, **47**, 3206.

13. G. Wysocki , R. F. Curl, F. K. Tittel *et al*., *Appl. Phys. B*, 2005, **81**, 769.

14. G. N. Rao and A. Karpf, *Appl. Opt*., 2011, **50**, 100.

15. D. A. Long, D. H. Havey, M. Okumura *et al*., *Phy. Rev. A*, 2010, **81**, 064502.

16. L. S. Rothmana, I. E. Gordona, A. Barbeb *et al*., *J. Quant. Spectrosc. Radiat. Transf*. **110**, 2009, 533.

17. H. H. Nielsen, *Revs. Modern Phys*., 1951, **23**, 90.

18. M. W. P. Strandberg, T. Wentink , Jr., and R. L. Kyhl, 1949, *Phys. Rev*. **75**, 270.

19. C. A. Burrst and W. Gordy, *Phys. Rev*., 1956, **101**, 599.

20. V. M. Devi, P. P. Das, A. Bano, and K. N. Rao, *J. Mol. Spectrosc.*, 1981, **87**, 578.

21. A. Maki, W. Quapp, and S. Klee, *J. Mol. Spectrosc.*, 1995, **171**, 420.

22. J. Warland, M. Lengele, and G. Blanquet, *Spectrochim. Acta, Part A*, 2004, **60**, 3299.

23. N. Larsen and B. Winnewisser, *Zeitschrift für Naturforschung A*, 1974, **29**, 1213.

24. D. H. Whiffen, *Mol. Phys.*, 1976, **31**, 989.

25. A. Belafhal, A. Fayt, and G. Guelachvili, *J. Mol. Spectrosc*, 1995, **174**, 1.

6 Measurement of high-precision stable $^{13}CO_2/^{12}CO_2$ isotope ratios in exhaled breath for diagnosis of small intestinal bacterial overgrowth with irritable bowel syndrome

Contents

6.1 Introduction:

Small intestinal bacterial overgrowth (SIBO), a very common gastroenterological disorder, is usually characterized by an increased number and/or abnormal type of bacteria in the small intestine, exceeding 10^5-10^6 colony forming units (CFU) per mL in jejunal aspirate[1,2]. SIBO contributes to the development of chronic diarrhoea, bloating, macrocytic anemia, weight loss, and even severe malabsorption and malnutrition caused by metabolic bacterial effects[3]. Several evidences suggest that SIBO is closely associated with irritable bowel syndrome (IBS), which is also one of the most common functional gastrointestinal disorders worldwide of unknown etiology and pathogenesis[4,5]. IBS is usually diagnosed by symptom-based criteria, known as Rome criteria[6,7]. It is still the subject of debate whether the individuals with IBS should be diagnosed as SIBO or individuals presenting with SIBO should be considered as the onset of IBS because the symptoms of IBS and SIBO overlap to a large degree[8]. The overall prevalence of SIBO among patients with an initial diagnosis of IBS is not yet exactly known because SIBO is often misdiagnosed and substantially underdiagnosed[9]. Some earlier reports, however, suggest that the SIBO is regularly found (30%-85%) in individuals fulfilling diagnostic criteria of IBS[3] but these studies are extremely debatable. Thus there is a pressing need to develop a better diagnostic methodology with high sensitivity and specificity for early detection of SIBO. Recently, some authors have also suggested that particular attention should immediately be given to diagnose SIBO in patients particularly with diarrhea-predominant IBS (IBS-D) because the patients with IBS-D often show higher frequency of SIBO than other sub-types of IBS for example, IBS with constipation (IBS-C), mixed IBS (IBS-M) and unsubtyped IBS (IBS-U)[4]. Moreover, it is also important to understand the clinical prognosticators for considering diagnosis of SIBO in individuals presenting as IBS.

The current diagnosis of SIBO is still controversial and consequently considerable disagreements exist in the literatures which diagnostic methodology would be the most appropriate for routine clinical purposes[5,10]. The standard method for the diagnosis of SIBO is considered to be quantitative microbial culture of jejunal aspirates. However, this method is invasive, carries numerous inherent technical difficulties in endoscopic harvesting jejunal fluid and the high-risk of contamination, indicating a cumbrous and impractical method for routine clinical purposes as well as not sensitive enough for early detection and follow up of patients. Therefore, indirect non-invasive breath tests such as hydrogen breath test[11,12] and ^{14}C-xylose breath test[13] have recently been proposed as diagnostic tools for SIBO. Currently, the hydrogen breath test (HBT) by ingestion of glucose or lactulose is considered to be an important diagnostic method for the detection of SIBO because the hydrogen is exclusively produced when carbohydrates are fermented by intestinal bacteria[12].

However, there are various limitations and drawbacks in HBT for the diagnosis of SIBO as described in several reports and review articles[10,14] and accordingly the conclusions drawn from the studies are highly controversial. The utility of the HBT with glucose is mostly limited by its low diagnostic sensitivity (40%) and specificity (80%). The protocols of the HBTs have not yet been accurately standardised. Presently there are no widely accepted criteria for what establishes a positive HBT, so in most cases an increase in hydrogen concentrations ≥ 10-12 parts per million (ppm) above the basal value is considered to be positive test result for bacterial overgrowth[14]. A positive HBT may not always indicative of the bacterial colonization in the small intestine as suggested by few authors[10,14] and hence the symptoms of a patient may not be caused by SIBO. Sometimes the precise distinctions would be extremely difficult as there may be similarities in the excretion profiles of volatile metabolites in the expired breath in individuals with SIBO and individuals with rapid intestinal transit in case of lactose or lactulose test meal. Moreover, it is also possible that some patients might produce other gases such as methane, hydrogen sulphide[3,14] etc in their breath samples rather than hydrogen and in such condition, HBT may not work if SIBO is present. It suggests that a parallel measurement of other gases in exhaled breath samples make the detection of SIBO more precise and specific.

Some authors[3,12] have proposed the possibility of the measurement of CO_2 along with H_2 and to our knowledge the measurements have not yet been explored in detail. It should be mentioned here that the measurement of $^{12}CO_2$ alone might have an influence on the diagnostic accuracy, since $^{12}CO_2$ is also produced endogenously at the same time in exhaled breath depending on the basal metabolic rates (BMR) in individuals. However, the high-precision real-time measurement of $^{13}CO_2/^{12}CO_2$ stable isotope ratios together with H_2 in breath samples after ingestion of ^{13}C-enriched glucose would make the detection of SIBO more specific and accurate. The principle of the measurement of isotopic $^{13}CO_2$ in exhaled breath is based on the fact that a large part of the CO_2 remains in the intestine following bacterial fermentation of glucose[12] and as a consequence, we hypothesized that individuals harboring SIBO would exhale less $^{13}CO_2$ in their breath compared with that in IBS without SIBO. To our knowledge, while no proven ^{13}C-glucose breath test (^{13}C-GBT) for measuring high-precision $^{13}CO_2/^{12}CO_2$ isotope ratios in real-time for screening individuals with suspected SIBO in patients with IBS has been reported to date, the aim of the present study was, therefore, to standardize and validate this methodology for diagnostic assessment.

In this chapter, we have demonstrated, the clinical effectiveness of ^{13}C-GBT method as an alternative non-invasive approach for the diagnosis of SIBO with individuals particularly presenting as diarrhea-predominant IBS (IBS-D). We applied a laser-based high-resolution cavity-enhanced absorption spectroscopy method for the measurements of $^{13}CO_2/^{12}CO_2$ isotope ratios in real-time. We also compared our results with the results of the HBT. In addition, a statistically significant diagnostic cut-off point of the $^{13}CO_2$ isotopic enrichments in exhaled breath was determined to obtain an insight into the diagnostic efficacy of ^{13}C-GBT methodology to identify SIBO.

6.2 Materials and Methods:

6.2.1 Subjects

The present study was approved by the Ethics Committee Review Board of AMRI Hospital, Salt Lake, India (Study No: AMRI/ETHICS/2013/2). Administrative approval (Ref. No: SNB/PER-2-6001/13-14/1769) from the S. N. Bose Centre, Kolkata, India was also obtained. All patients gave informed written consent prior to the participation in the present study. A total of 118 patients (74 male, 44 female, age: 23-75 yrs) with diarrhea-predominant IBS diagnosed according to the symptom-based Rome III criteria were enrolled in the present study and subsequently all these subjects with suspected SIBO were considered for the ^{13}C-GBT to explore the simultaneous measurements of $^{13}CO_2/^{12}CO_2$ isotope ratios and H_2 concentrations in exhaled breath samples. Each subject filled in a set of Rome III questionnaires before the ^{13}C-GBT, which allowed interpretation of IBS sub-type as this has previously been employed and recommended[6,7]. However, subjects were excluded from the present study if they had been taking antibiotics, proton pump inhibitors during the preceding four weeks of the study, colonoscopy within a week before HBT, treatment with drugs that interfere with gastrointestinal motility, or if they had a previous history of prior gastric surgery, corrosive injury, systematic sclerosis, diabetes, liver cirrhosis, COPD, smoking and taking any medication that hamper the glucose metabolism.

6.2.2 Breath Sample Collection and measurements

The subjects underwent the ^{13}C-GBT protocols after an overnight fast (~10-12 hours) by ingesting a drink containing 50 mg ^{13}C-labelled glucose (CLM-1396-CTM, Cambridge Isotope Laboratories, Inc. USA) with 50 g normal glucose dissolved in 250 ml of water. A baseline breath sample was collected in a 750 ml breath collection bag (QT00892, QuinTron Instrument Co. USA) before the administration of the ^{13}C-enriched substrate. Additional breath samples were then collected at 15 min intervals for 180 min for the measurements of $^{13}CO_2/^{12}CO_2$ isotope ratios by a high-precision laser-based isotopic CO_2 analyzer [CCIA 36-EP, LGR, USA], working on principle of cavity enhanced technique. The CO_2 spectrometer, its feasibility test and standard procedure for high-precision isotopic breath CO_2 measurements in real-time have been described in appendix-A.

The $^{13}CO_2$ enrichment in breath samples is usually expressed by δ^{13}C notation in parts per thousand (or per mil, ‰)

$$\delta^{13}C\ (‰) = (R_{sample} / R_{standard} - 1) \times 1000$$

Where, R_{sample} is the $^{13}C/^{12}C$ isotope ratio of the sample and $R_{standard}$ is the international standard Pee Dee Belemnite (PDB) value, i.e. 0.0112372. The CO_2 isotopic ratios in breath samples are usually reported as the delta-over-baseline (DOB), i.e. $\delta_{DOB}{}^{13}C‰$. All experimental results were expressed in $\delta_{DOB}{}^{13}C‰$ values which refer to the post-baseline and baseline relation of $^{13}CO_2/^{12}CO_2$ isotope ratios in exhaled breath samples, i.e.

$$[\delta_{DOB}{}^{13}C\ (‰)]_{t=tmin} = [\delta^{13}C\ (‰)]_{t=tmin} - [\delta^{13}C\ (‰)]_{t=0min}$$

All breath samples were repeated. However, the measurements of H_2 concentrations in ppm were carried out by Gastrolyzer and patients were instructed to blow directly into the H_2 measurement equipment (Gastro$^+$ Gastrolyzer, Bedfont Scientific Ltd. Model No: CE0086). At first, fasting breath hydrogen was estimated and then the measurements were done at 15 min intervals for 180 min following ingestion of ^{13}C-enriched glucose. The average of three values was taken as basal breath hydrogen test. ^{13}C-GBTs were performed under absolutely blind conditions with no knowledge of HBT results. The detailed protocol followed in this study is shown in figure 6.1. It should be mentioned here that during the test, any kind of food, drink, smoking or physical exercise were not allowed. The subjects also washed off their mouths before ingesting the ^{13}C-substrate to avoid any kind of contact of the test substrate with the oral bacteria. Furthermore, the subjects also received instructions not to ingest cane sugar, corn, corn products, during the last few days before the ^{13}C-GBT to avoid the naturally enriched ^{13}C items and also not to take slowly absorbed carbohydrate (like bread), leafy vegetable, legumes and fiber on the previous night of the test to reduce the basal H_2 level.

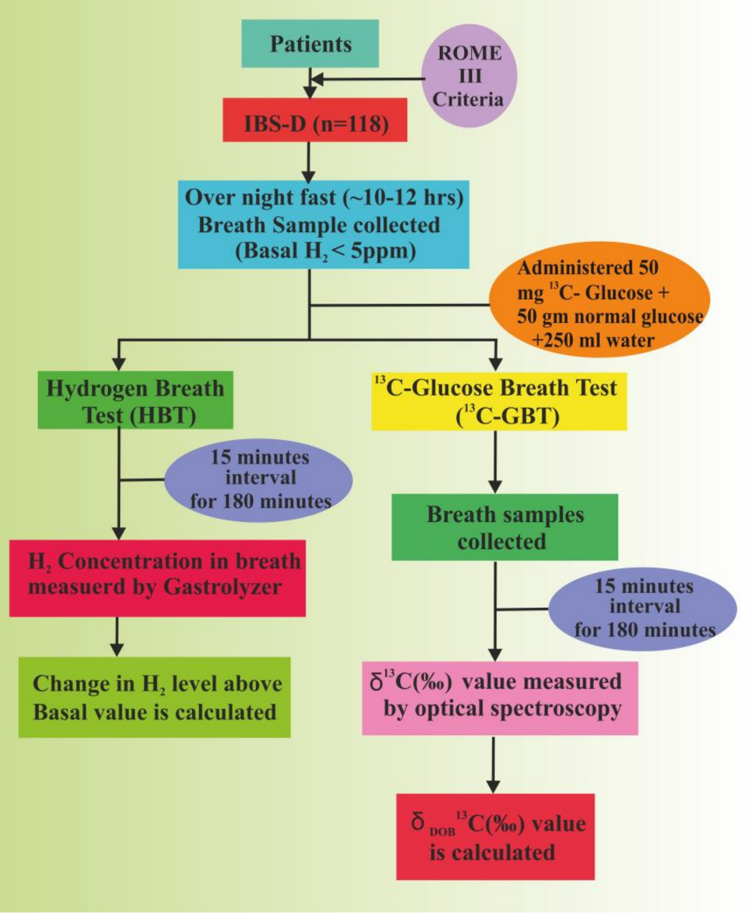

Figure 6.1 *The flow diagram representing the steps of the procedure followed in this study.*

6.2.3 Statistical Analysis

Non parametric statistical analyses (Mann-Whitney Test), one-way ANOVA analyses were performed to assess the breath test results. The data were expressed as mean ± SD. Box and whiskers plots were utilized to demonstrate the statistical distribution of $\delta_{DOB}{}^{13}C‰$ values in exhaled breath samples. Results were also expressed as the cumulative percentage dose of ^{13}C-recorved (c-PDR%) in breath samples after correction for variability of endogenous CO_2 production caused by different BMRs in individuals. Data analysis was performed using Origin Pro 8.0. A two-sided p value < 0.05 was considered to indicate statistical significance.

6.3 Results and Discussion:

6.3.1 Validation of ^{13}C-GBT for diagnosis of SIBO

Figure 6.2 depicts the excretion kinetic patterns of $\delta_{DOB}{}^{13}C‰$ values and H_2 concentrations in exhaled breath samples for n=78 IBS-D patients after ingestion of ^{13}C-enriched glucose. In the first series of experiments, we have investigated the ^{13}C-GBT on 78 patients where the test is considered positive SIBO if the basal value of H_2 is ≤ 5 ppm and there was a clear peak of H_2, exceeding 20 ppm within 60 min, as previous studies suggested that subjects with this consideration is a very likely to be indicative of a positive test result[12]. We observed that in case of IBS-D individuals with positive H_2 breath test (n=25), the $\delta_{DOB}{}^{13}C‰$ values in breath samples depleted more compared to the IBS-D patients with negative H_2 breath test (n=53).

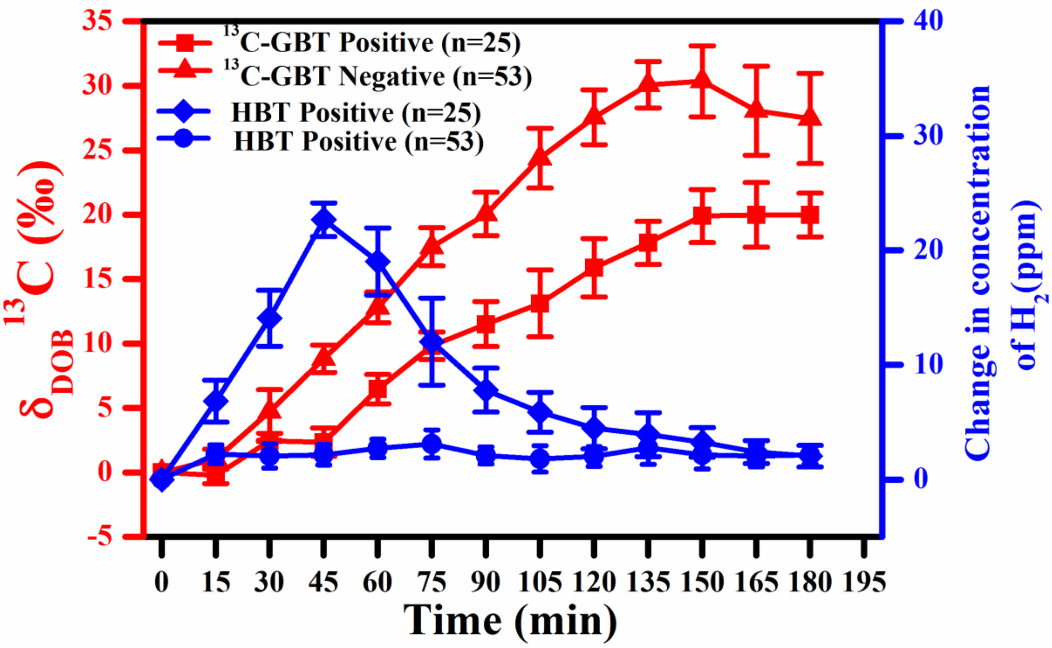

Figure 6.2 *The excretion kinetics profiles of $\delta_{DOB}{}^{13}C$ (‰) and change in concentration of H_2 (ppm) for SIBO positive (n=25) and SIBO negative (n=53) IBS-D subjects. Error bars correspond to 1 SD.*

Consequently, there was a clear distinction of the $\delta_{DOB}{}^{13}C$‰ values in breath samples after 45 min between IBS-D individuals with positive and negative H_2 breath test, demonstrating the measurements of $\delta_{DOB}{}^{13}C$‰ values in breath samples is also an alternative diagnostic tool for the non-invasive detection of SIBO in IBS-D patients. It was previously reported that under physiological circumstances, glucose is readily absorbed in the small intestine[12]. It is initially decomposed by anaerobic bacteria into short-chain fatty acid (SCFA), CO_2, hydrogen and even deconjugate bile acid as a part of the fermentation reaction if there is a bacterial overgrowth in the small intestine. This may contribute to the pathogenesis of diarrhea in patients with SIBO, as suggested recently by Ghoshal *et al.*[4]. However, in our observation, a significant decrease of $\delta_{DOB}{}^{13}C$‰ values in breath samples in case of IBS-D patients with suspected SIBO (positive HBT) compared with IBS-D patients without SIBO (negative HBT), is attributed to the fact that a small part of ^{13}C-enriched glucose is fermented by bacteria to produce $^{13}CO_2$ which mostly remains unabsorbed in the intestine and as a result, comparatively less ^{13}C-enriched glucose would be available to the cell to oxidize it to produce $^{13}CO_2$ in the exhaled breath. Although the exact mechanism of these observations is not yet known, however, our findings suggest that the IBS-D patients with suspected SIBO could clearly be distinguished from IBS-D individuals without SIBO on the basis of isotopic enrichments of CO_2 in exhaled breath samples.

Figure 6.3a and 6.3b depict Box and Whisker plots of $\delta_{DOB}{}^{13}C$ values in per mil (‰) and H_2 concentrations in parts per million (ppm) at 45 min to illustrate the statistical distribution of $^{13}CO_2$ enrichments and the amount of H_2 productions in IBS-D patients with and without SIBO. We observed that the mean (2.35± 1.10 ‰ versus 8.82 ± 1.06 ‰), median (2.63 ‰ versus 8.38‰) and inter-quartile ranges (2.52-2.98‰ versus 7.13-10.40‰) of $\delta_{DOB}{}^{13}C$‰ values decreased significantly ($p < 0.001$) for IBS-D with SIBO patients compared to the IBS-D without SIBO patients, indicating the potential of high-precision measurements of $^{13}CO_2/^{12}CO_2$ isotope ratios as an alternative methodology to accurately diagnose of SIBO in IBS-D patients.

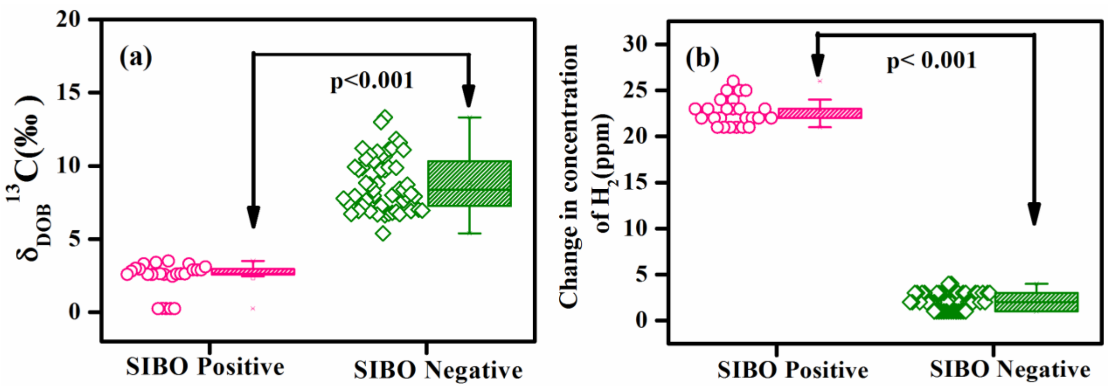

Figure 6.3 *(a) and (b) show statistically significant difference in* $\delta_{DOB}{}^{13}C$ *(‰) values and change in hydrogen concentrations above the basal value for SIBO positive (n=25) and SIBO negative (n=53) IBS-D subjects at 45 min. Scattered points, represented as diamonds and circles correspond to actual experimental data points*

We subsequently determined the cumulative percentage dose of ^{13}C-recovered (c-PDR %) at 45 min in exhaled breath samples for both positive and negative SIBO patients. We applied the Klein *et al.*[15] equation following correction of endogenous CO_2 production to calculate the c-PDR % in breath samples and subsequently the results are illustrated by Box and Whiskers plots as shown in figure 6.4a and 6.4b.

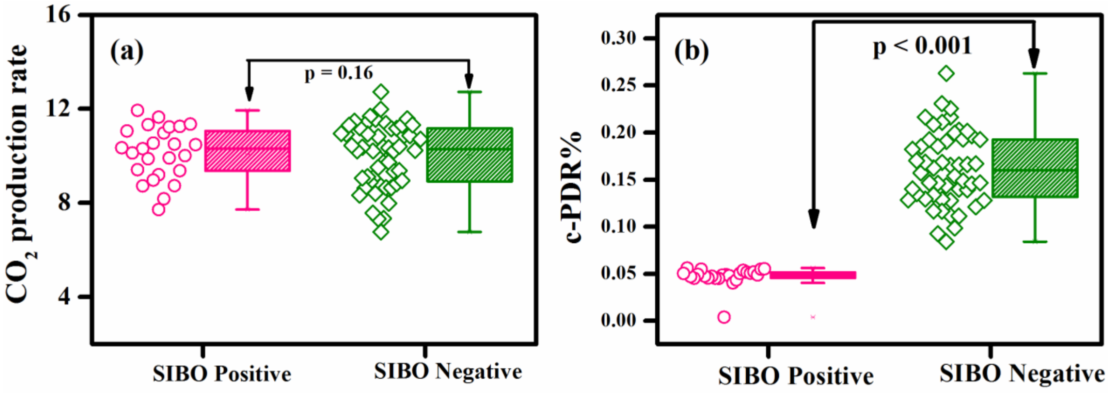

Figure 6.4 (a) *shows statistically insignificant (p=0.16) difference of endogenous CO_2 production rates related to BMR between IBS-D patients with and without SIBO.* (**b)** *A statistically significant difference (p<0.001) is observed in c-PDR(%) in exhaled breath samples between the two groups of IBS-D patients at 45 min after ingestion of ^{13}C glucose. Scattered points, represented as diamonds and circles correspond to actual experimental data points.*

Although there was no statistically significant difference of endogenous CO_2 production rate, but a marked difference of c-PDR (%) values between IBS-D patients with and without SIBO exhibited the evidence of bacterial overgrowth and thus confirmed the clinical feasibility of the ^{13}C-GBT in the diagnosis of SIBO in IBS-D patients.

Our observations also suggest that an optimal cut-off level of $\delta_{DOB}{}^{13}C‰$ value ≤ 5.47‰ at 45 min is indicative of positive SIBO, as depicted in figure 6.5. The cut-off point was found to be greater than 2 standard deviation (SD) from the means of $\delta_{DOB}{}^{13}C‰$ values of SIBO positive and SIBO negative patients, indicating the risk of false-positive or false-negative results of ^{13}C-GBT for the diagnosis of SIBO were lower than 2.3% using the cut-off value of 5.47‰ at 45 min.

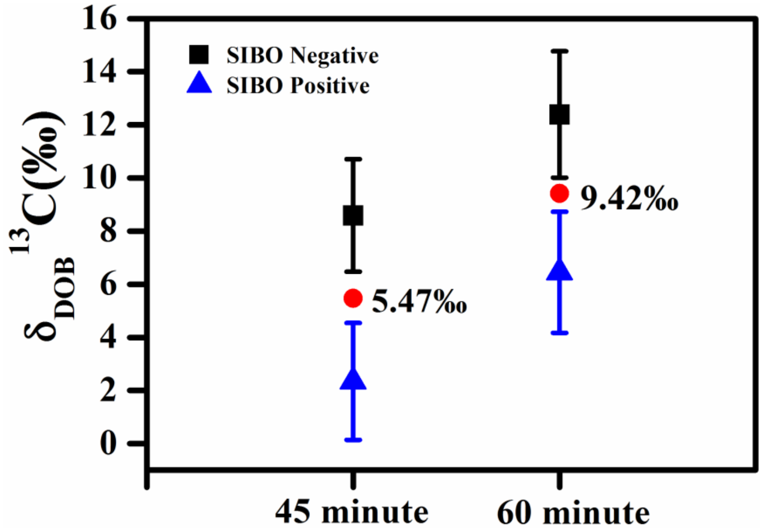

Figure 6.5 *illustrates the optimal cut-off levels of* $\delta_{DOB}{}^{13}C$‰ *value* $\leq$ *5.47‰ at 45 min and 9.42‰ at 60 min. The values are well separated (more than ±2 SD) from the means for the both groups of IBS-D patients at 45 min and 60 min, respectively.*

We can also take a cut-off value of 9.42‰ at 60 min to discriminate positive and negative results, as shown in figure 6.5.

6.3.2 Discriminatory results between ^{13}C-GBT & HBT

In the second series of studies, we explored the excretion profiles of $\delta_{DOB}{}^{13}C$‰ values on IBS-D patients (n= 20) whose H_2 concentrations in exhaled breath samples were in the range of 3-8 ppm at 45 min after ingestion of ^{13}C-enriched glucose. As there was no significant increase of H_2 levels (typically $\geq$10-12 ppm) above the basal value (which was $\leq$ 5 ppm), normally, the test should not be considered as a positive syndrome of SIBO, according to the previously reported observations[12,14]. However, we observed a very interesting behaviour of $\delta_{DOB}{}^{13}C$‰ values in our results; all these patients followed the similar excretion profiles of $\delta_{DOB}{}^{13}C$‰ values with the profiles of IBS-D patients presenting as positive SIBO, as depicted in figure 6.6. At standard post-therapy, all patients exhibited marked improvement in symptoms, thus suggesting the false-negative results of the hydrogen breath test for this group of patients.

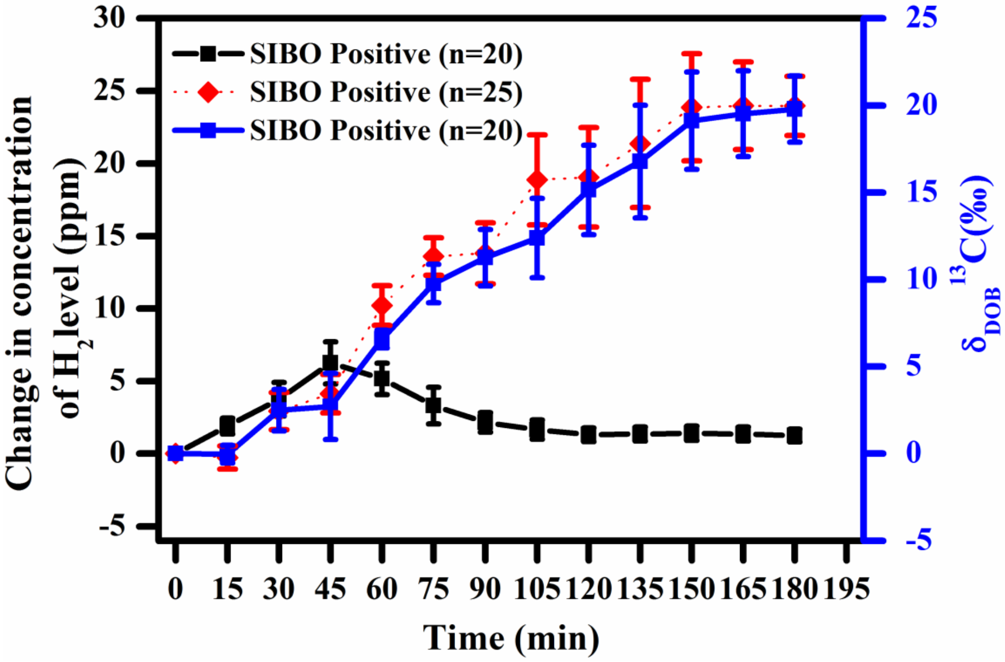

Figure 6.6 *illustrates a group of IBS-D (n=20) patients (H_2 level: 3-8 ppm) follows the similar excretion pattern of $\delta_{DOB}{}^{13}C$ (‰) values in exhaled breath of previously detected SIBO positive patients (n=25), indicating the false negative results of HBT. Error bars correspond to 1 SD.*

It was previously reported that many individuals have non-hydrogen-producing colonic bacteria and hydrogen consuming bacteria[5,12]; in such situation patients do not excrete hydrogen but can produce other gases for instance, CO_2 as a part of the fermentation process. Therefore, HBT may not always be useful for the diagnosis of SIBO. Moreover, our findings suggest that HBT can also underestimate the presence of SIBO. In this context, some authors have also suggested that lactulose HBT might be useful for the cases of "non-hydrogen-production" individuals. But recently, U. C. Ghoshal *et al.*[8] demonstrated that lactulose HBT may not be appropriate for the diagnosis of SIBO, in Asian populations, more specifically in Indian patients because of shorter mouth-to-cecum transit time. However, our high-precision measurements of $\delta_{DOB}{}^{13}C$‰ values in exhaled breath samples after ingestion of ^{13}C-enriched glucose correctly diagnosed SIBO in IBS-D patients (n=20), suggesting it a valid and potentially robust approach for the non-invasive detection of SIBO, when HBT fails to diagnose of SIBO.

6.3.3 Inconclusive results of HBT

We subsequently investigated the efficacy of ^{13}C-GBT on a portion of IBS-D individuals (n=20) whose H_2 levels were in the range of 10-20 ppm above the basal value following ingestion of 13C-labelled glucose, as shown in figure 6 7.

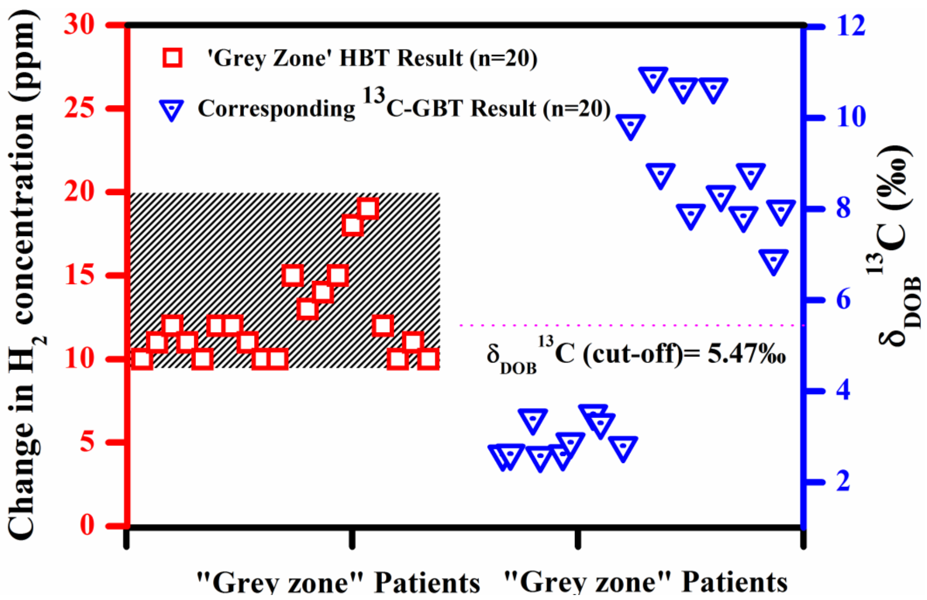

Figure 6.7 *shows the "grey-zone" of hydrogen concentration (10-20 ppm) above basal value for n=20 IBS-D patients and their corresponding $\delta_{DOB}{}^{13}C$‰ values for ^{13}C-GBT. 11 IBS-D patients are above and 9 IBS-D patients are below the cut-off at 45 min assessed by ^{13}C-GBT. Scattered points, represented by squares and inverted triangles correspond to actual experimental data points.*

When the H_2 levels in exhaled breath fall in this region (10-20 ppm), the test result is considered a "borderline positive" or may be termed as "grey-zone" result. Sometimes it is very critical to correctly diagnose SIBO if the H_2 levels are very close to the selected borderline (i.e. 10-12 ppm in most cases for HBT) or within the "grey-zone" and consequently the results of HBT remain debatable and affects the diagnostic accuracy of SIBO. Therefore, the measurements of H_2 levels in breath samples within this area should carefully be interpreted. This "grey-zone" may contain unreliable results which accounts for instinctive variations of H_2 levels in breath samples after the glucose load, patient's metabolisms and considerable heterogeneity of symptoms as well as the limits of the analytical precision of H_2 measurements. Furthermore, many IBS-D patients may fall in the "grey-zone" when the SIBO is just "switched-on" or individuals are at the onset of new symptoms associated with SIBO. However, it is still controversial when or how to recognize IBS patients at-risk for SIBO or during the preclinical phase of SIBO, therefore an accurate, fast, high-precision along with ultra-sensitive measurements of H_2 or isotopic CO_2 in real-time prior to the acute onset of SIBO remains a challenge.

Figure 6.8 (a) and (b) show that when the H_2 levels are at the "borderline" or within the "grey-zone", the significant level of the statistical analysis of H_2 concentrations between positive and cut-off value for HBT is degraded ($p = 0.24$) compared to the statistical level of $\delta_{DOB}{}^{13}C$‰ measurements ($p=0.03$ for negative ^{13}C-GBT and $p<0.001$ for positive ^{13}C-GBT) in breath samples

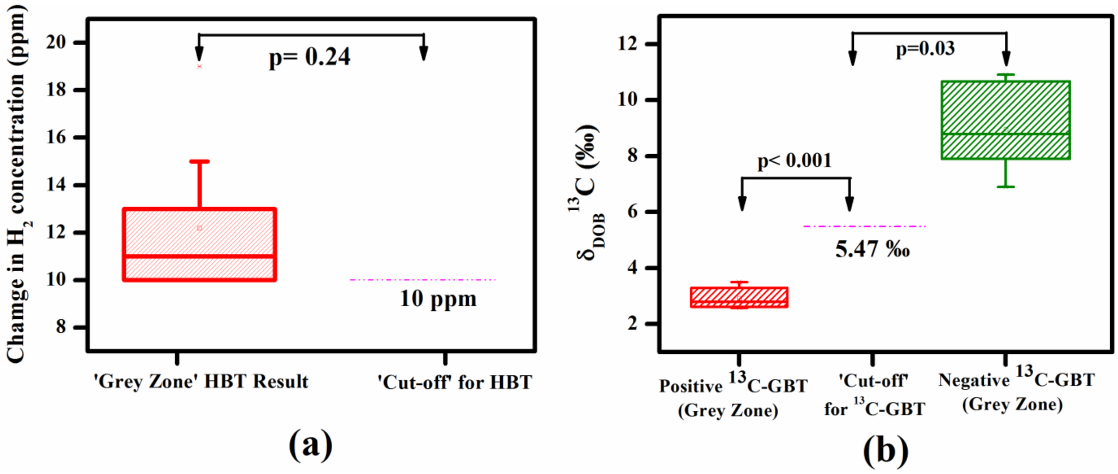

Figure 6.8 (a) and (b) *show H_2 concentrations between positive and negative SIBO patients is degraded (p=0.24) compared to the statistical level of $\delta_{DOB}{}^{13}C$‰ measurements (p=0.03 for negative ^{13}C-GBT and p<0.001 for positive ^{13}C-GBT) in breath samples from grey-zone patients.*

In the present study, the $\delta_{DOB}{}^{13}C$‰ values in breath samples were measured with a precision or accuracy of ±0.25‰, whereas the typical accuracy level of the current H_2 measurement system is within ±10%. This indicates that when an individual is just at the onset of SIBO or the H_2 level is at the "borderline" or in the "grey-zone", HBT may not be an appropriate diagnostic tool for accurate diagnosis of SIBO. However, our findings suggest that the measurements of $\delta_{DOB}{}^{13}C$‰ values with a precision of ±0.25‰ in breath samples after ingestion of ^{13}C-labelled glucose can precisely diagnose the evidence of SIBO in IBS-D patients, thus validating the widespread clinical efficacy of the ^{13}C-GBT in the diagnosis of SIBO and proposing also the methodology to be suitable for early diagnosis and follow-up of SIBO patients in routine clinical practices or daily decision making method.

6.3.4 Prevalence of SIBO

Finally, we explored the prevalence i.e. percentage of SIBO in IBS-D patients. In this study, the prevalence of SIBO was estimated to be 45.7%. Table 1 illustrates the investigations on SIBO in patients with IBS-D from India. Some earlier studies in Indian populations demonstrated that the frequency of SIBO in IBS patients was in the range of 7-11% [16-18]exclusively assessed by HBT.

Table 6.1 Summary of prevalence of SIBO in IBS patients in Indian population

Diagnostic Methods	No. of IBS$^{\Delta}$ Patients	Percentage of SIBO$^{\phi}$ in IBS Patients	References
*HBT	225	11.0%	Rana *et al.*[16]
*HBT	69	13.0%	Gupta *et al*.[17]
*HBT	148	7.0%	Ghosal *et* al[18].
♦^{13}C-GBT	118(IBS-D$^{\Phi}$)	45.76% [Male-47.29%; Female- 43.18%]	Present Study

*HBT- Hydrogen breath test; ♦^{13}**C**-GBT- ^{13}**C**-Glucose breath test; $^{\Delta}$ IBS- Irritable bowel syndrome; $^{\phi}$ SIBO- Small intestinal bacterial over growth; $^{\Phi}$ IBS-D- Diarrhea-predominant irritable bowel syndrome.

However, the present study is the first experimental demonstration showing that patients with IBS-D from India have a higher prevalence of SIBO assessed by ^{13}C-GBT, compared to some earlier studies in Indian populations. It should be pointed out here that these previous studies in Indian populations were carried out for the diagnosis of SIBO using the HBT methodology. Because of numerous intrinsic drawbacks, and limitations of the HBT as mentioned beforehand as well as demonstrated in the present study, the previous investigations in Indian populations could possibly have underestimated the frequency of SIBO in IBS patients. However, utilizing the ^{13}C-GBT, SIBO turned out to be more prevalent in IBS-D patients in Indian subjects, thus suggesting a potential link between IBS-D patients and SIBO symptoms.

6.4 Conclusions

In this chapter we have demonstrated the clinical feasibility of a novel ^{13}C-gluocse breath test (^{13}C-GBT) by measuring high-precision $^{13}CO_2/^{12}CO_2$ stable isotope ratios in exhaled breath samples in the diagnosis of small intestinal bacterial overgrowth (SIBO) in diarrhea-predominant irritable bowel syndrome (IBS-D) subjects. We have shown the ^{13}C-GBT methodology can accurately diagnose the presence of SIBO even when SIBO is just “switched-on” or at the onset of the syndrome as well as when the patients do not produce hydrogen, thus making it a valid and potentially robust alternative non-invasive diagnostic approach for the detection of SIBO and is superior to the widely used hydrogen breath test (HBT). We also observed a higher prevalence of SIBO in IBS-D patients, thus indicating a strong association between IBS-D patients and SIBO symptoms. Our findings also suggest that the present ^{13}C-GBT methodology could routinely be used in many clinical settings or laboratories for diagnostic assessment of SIBO in any sub-types of IBS patients when HBT fails to diagnose of SIBO.

6.5 References

1. A.C. Dukowicz, B.E. Lacy and G.M. Levine, *Gastroenterol Hepatol.*, 2007, **20**, 112.

2. H.C Lin, *JAMA.*, 2004, **292**, 852.

3. J. Bures, J. Cyrany, D. Kohoutova *et al.*, *World J Gastroenterol.*,2010, **16**, 2978.

4. U. C. Ghoshal and D. Srivastava, *World J Gastroenterol.*, 2014, **20**, 2482.

5. U.C. Ghoshal, R. Shukla, U. Ghoshal *et al.*, *Int J Inflam.*, 2012, **2012**, doi:10.1155/2012/151085.

6. X. Yao, Y.S. Yang, L. H. Cui *et al.*, *J Gastroenterol Hepatol.*, 2012, **27**, 760.

7. M. Camilleri, *Clin Gastroenterol Hepatol.*, 2010, **8**, DOI: 10.1016/ j.cgh. 2009.10.009.

8. U.C. Ghoshal, H. Park and K-A. Gwee, *J Gastroenterol Hepatol.*, 2010, **25**, 244.

9. I. Esposito, A de Leone, G. D. Gregoria *et.al.*, *World J Gastroenterology* 2007, **13**, 6016.

10. M. Simren and P. O. Stotzer, *Gut*, 2006, **55**, 297.

11. A. Lupascu, M. Gabrielli, E. C. Luritano *et al.*, *Aliment Pharmacol Ther.*, 2005, **22**, 1157.

12. A. Eisenmann, A. Amann, M. Said *et al.*, *J. Breath Res.*, 2008, **2,** DOI:10.1088/1752-7155/2/4/046002.

13. B. Walters and S.J. Vanner, *Am J Gastroenterol.*, 2005, **100**,1566.

14. U. C. Ghoshal, *J Neurogastroenterol Motil.*, 2011, **17**, 312.

15. P. D. Klein, H. M. Malaty, S. J. Czinn *et al.*, *J Pediatr Gastroenterol Nutr.*, 1999, **29**, 297.

16. S. V. Rana, S. K. Sinha, A. Sikander *et al.*, *Trop Gastroenterol.*, 2008, **29,** 23.

17. D. Gupta, U. C. Ghoshal, A. Misra *et al.*, *J Gastoenterol Hepatol.*, 2007, **22**, 2261.

18. U. C. Ghoshal, S. Kumar, M. Mehorta *et al.*, *Neurogastroenterol Motil.*, 2010; **16**: 40.

7 Summary and Outlooks

In this thesis we have demonstrated the development of a mid IR continuous wave (cw) external-cavity (EC) quantum cascade laser (QCL) based cavity ring-down spectrometer (CRDS) and its application in trace gas sensing including the studies on high resolution ro-vibrational molecular spectroscopy. The extremely narrow linewidth, wide tunibility with mode-hop-free operation features of the EC-QCL in the mid IR spectral region allowed us to access strong fundamental bands of the analyte molecules with significant importance in biomedical and atmospheric science. Furthermore, the direct *in situ* measurements of high resolution spectra provide us the quantitative absorption of trace species with numerous spectroscopic parameters which have also substantial importance in fundamental molecular spectroscopy. Additionally, the isotope selective measurement of exhaled breath CO_2 exploiting the cavity-enhanced technique opens up a new area of research in non-invasive diagnosis of different gastrointestinal and metabolic disorders such as small intestinal bacterial overgrowth (SIBO). Moreover, the optical cavity based technique removes the discrepancies of hydrogen breath test which is commonly used for non-invasive diagnosis of SIBO in routine clinical practice.

In the first chapter of the thesis, we have discussed about fundamentals of infrared molecular spectroscopy, different spectral features such as spectral line width and various type of broadening mechanism with their origin. Then we have discussed about both the common spectroscopic and non-spectroscopic detection techniques for monitoring the trace molecular species in exhaled human breath and atmosphere. Simultaneously, the importance of monitoring of those molecules in biomedical and environmental studies have also mentioned in this chapter.

The basic principle of cavity ring-down spectroscopy with its advantageous features over other conventional spectroscopic techniques is illustrated in chapter-2. The stability parameters with construction of high-finesse stable optical cavity to perform such high sensitive experiment are included in this chapter. Propagation of a Gaussian beam inside the cylindrical cavity, cavity mode structure and the overlapping of cavity modes with laser frequency in both the pulsed CRDS and *cw*-CRDS experiment are also incorporated in this section. Moreover, a description of Allan-Variance analysis which demonstrates the stability of the optical cavity in *cw*-CRDS experiment is also included in this chapter.

Nitrous oxide (N_2O) is a key example of trace molecular species in environment and considered as a most important greenhouse gas responsible for global warming as well as climate change by destructing the ozone layers in stratosphere. In chapter 3, we have demonstrated the development of an MHF-EC-QCL based high-resolution *cw*-CRDS instrument operating at $\lambda \sim 5.2\mu m$ for direct quantitative measurement of atmospheric nitrous oxide in different periods of the day in a variety of environments involving different source of local pollution. Our experimental results show there is a significant change in N_2O concentrations in different sub-areas depending on the source of local pollutant

There is a motivation to measure the trace molecular species such as nitric oxide (NO) and carbonyl sulphide which are considered as biologically important molecules associated with different types of gastrointestinal and metabolic disorders in human subjects as described in chapter-1. Moreover, N_2O and C_2H_2 are another two trace molecular species play the essential role in atmospheric pollution. In chapter -4, we have demonstrated the simultaneous monitoring of multiple trace molecular species such as NO, OCS, N_2O and C_2H_2 in a relatively small tuning range of ~0.05 cm^{-1} using the same EC-QCL based CRDS system. Using the developed spectrometer, the trace detection of those molecules was performed in exhaled human breath as well as in atmospheric samples. A good agreement among their measured concentrations with their typical concentration in exhaled human breath and atmosphere suggested the potential applicability of the CRDS sensor both in biomedical and environmental science for measurement of trace gas analysis.

Moreover, carbonyl sulphide (OCS) is a molecule with astrophysical interest and the weak hot band transition in *l*=2 vibrational state has not yet been explored. Using our developed CRDS system, the doublet structures of OCS have been studied for J=22 to J=29 rotational lines for $(14^20) \leftarrow (02^20)$ ro-vibrational transition and subsequently, the splitting constant, vibrational transitional dipole moments, rotational constants and centrifugal distortion constants for the *e* and *f* sub-states of the particular (14^20) vibrational state have been calculated in chapter 5. These measurements suggest the application of EC-QCL based CRDS system for high-resolution spectroscopy study. The work has been extended for the measurement of natural abundance of two other isotopolouges of OCS i.e. $^{16}O^{12}C^{34}S$ and $^{16}O^{12}C^{33}S$ in standard calibration gas. Our new experimental data will be helpful for fundamental understanding of linear polyatomic molecular properties and hyperfine structures of their isotopologues.

In chapter 6, we have demonstrated the development of an alternative non-invasive ^{13}C-Glucose breath test methodology by measuring the $^{13}CO_2/^{12}CO_2$ isotope ratios in exhaled breath exploiting a cavity-enhanced technique for diagnosis of SIBO in diarrhea predominant irritable bowel syndrome patients. The present methodology overcomes the drawbacks of hydrogen breath test which is widely used for non-invasive diagnosis of SIBO in IBS subjects. Beside that ^{13}C GBT methodology is enough capable to diagnose the IBS subjects with SIBO when the infection is just switched-on or at the onset of the syndrome. Thus present methodology is a valid and potentially robust for diagnosis of SIBO and can be employed for large screening of SIBO in IBS patients.

Thus the present thesis work elucidates the versatile applications of the mid IR cavity enhanced absorption techniques such as CRDS in biomedical diagnostics as well as environmental applications. The accurate and non-invasive diagnosis of different physiological disorders by monitoring the trace components in exhaled breath exploiting CRDS techniques may pave the way for opening new strategies in next generation medical diagnosis. Moreover, the mid IR *cw*-EC-QCL based CRDS technique enriched the atmospheric research by monitoring the trace constituents with their isotopes which are responsible for pollution in atmosphere. Alongside the high resolution spectroscopic features of the molecular absorption enabled us to explore the new spectroscopic parameters which are helpful for understanding of fundamental molecular spectroscopy and molecular properties as well.

A $^{13}CO_2$ and $^{12}CO_2$ isotope Analyzer:

A high resolution CO_2 carbon isotope analyzer exploiting the cavity enhance absorption spectroscopy technique was utilized for high precision isotopic measurement of breath CO_2. In brief, the laser-based CO_2 spectrometer (CCIA 36-EP, Los Gatos research, USA) comprised of a high-finesse optical cavity (~59 cm) with two high reflectivity mirrors (R ~ 99.98%) at the both ends of the cavity. This arrangement provides an effective optical path-length of around 3 km through the measuring gas sample, thus offering a high-precision measurement. A continuous wave distributed feedback diode laser operating at ~2.05 μm is repeatedly tuned over 20 GHz to scan the absorption features of $^{12}C^{16}O^{16}O$, $^{12}C^{18}O^{16}O$ and $^{13}C^{16}O^{16}O$ at the wavenumber of 4878.292 cm^{-1}, 4878.006 $cm^{-1}$and 4877.572 cm^{-1}, respectively. The cavity of the spectrometer is regulated at 46 $^{\circ}C$ by a resistive heater and feedback control system. A typical pressure of 30 Torr is maintained inside the cavity through a diaphragm pump. A solenoid valve along with mass flow controllers are used to control the flow of samples inside the cavity. The absorption features of $^{12}C^{16}O^{16}O$, $^{12}C^{18}O^{16}O$ and $^{13}C^{16}O^{16}O$, corresponding to the R (34e), P (32) and P (12e) rotational lines respectively, in the $2\nu_1+\nu_3$ $[(00^00)\rightarrow(20^01)]$ vibrational combinational band of CO_2, have been utilized to measure the $^{13}C/^{12}C$ and $^{18}O/^{16}O$ isotope ratios simultaneously. The HITRAN simulation of the above mentioned absorption line of CO_2 isotoplogues is shown in figure A1

The transmitted laser intensities were recorded by exploiting a photodetector after passing through a breath sample of interest. Absorption was determined from the measurement of voltage from photodetector

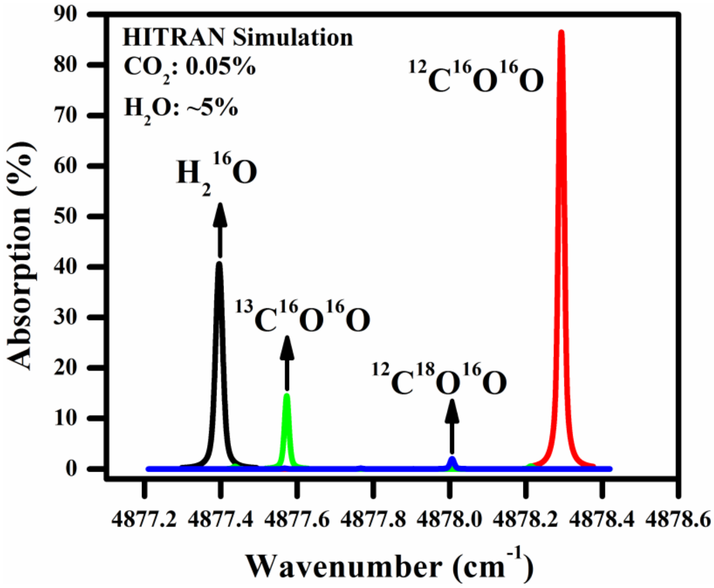

Figure A1. *HITRAN simulation of CO_2 isotoplogues i.e.* $^{12}C^{16}O^{16}O$, $^{12}C^{18}O^{16}O$ and $^{13}C^{16}O^{16}O$ *corresponding to R(34), P(32) and P(12) rotational lines of* $2\nu_1+\nu_3$ *combination band with peak centre at 4878.292* cm^{-1}*, 4877.572* cm^{-1} *and 4878.006* cm^{-1} *respectively.*

Beer-Lambert law was utilized to calculate the concentration after integrating the absorption spectrum. The $^{13}CO_2$ and $C^{18}O^{16}O$ enrichments in samples are usually expressed by $\delta^{13}C$ and $\delta^{18}O$ notation in parts per thousand (or per mil, ‰)

$$\delta^{13}C‰ = (R_{sample} / R_{standard} - 1) \times 1000$$

$$\delta^{18}O‰ = (R_{sample} / R_{standard} - 1) \times 1000$$

Where, R_{sample} is the $^{13}C/^{12}C$ and $^{18}O/^{16}O$ isotope ratios of the sample and $R_{standard}$ are the international standard Pee Dee Belemnite (PDB) values, i.e. 0.0112372 and 0.0020672 respectively for $\delta^{13}C$ and $\delta^{18}O$ measurements. The manufacturer specified precessions' for measurement of $\delta^{13}C$ and $\delta^{18}O$ are 0.1‰ and 1‰, respectively. However, The accuracy and precision of the instrument were verified by repeated measurements of three calibration standards with $\delta^{13}C$‰ values of -22.8‰, -13.22‰ & -7.33‰ (Cambridge Isotope Laboratory, USA) and a precision of 0.2‰ was achieved.